Master's thesis

NTNU
Norwegian University of Science and Technology
Faculty of Natural Sciences
Department of Physics

Vilde Ragnvaldsen

Feasibility of Water Equivalent Path Length Analysis in Adaptive Proton Therapy of Locally Advanced Non-Small Cell Lung Cancer

Master's thesis in Biophysics and Medical Technology
Supervisor: Helge Egil Seime Pettersen, Kristine Fjellanger, Liv Bolstad Hysing
Co-supervisor: Kathrine Røe Redalen

January 2022

NTNU
Norwegian University of Science and Technology

Haukeland University Hospital

Vilde Ragnvaldsen

Feasibility of Water Equivalent Path Length Analysis in Adaptive Proton Therapy of Locally Advanced Non-Small Cell Lung Cancer

Master's thesis in Biophysics and Medical Technology
Supervisor: Helge Egil Seime Pettersen, Kristine Fjellanger, Liv Bolstad Hysing
Co-supervisor: Kathrine Røe Redalen
January 2022

Norwegian University of Science and Technology
Faculty of Natural Sciences
Department of Physics

NTNU
Norwegian University of Science and Technology

PREFACE

This thesis presents my master's degree in Biophysics and Medical Technology at the Norwegian University of Science and Technology (NTNU) in Trondheim. The work was carried out at Haukeland Univeristy Hospital (HUH) in Bergen from August 2021 to January 2022 as part of a research project called *Establishing a framework for interdisciplinary clinical particle therapy research at Haukeland Univeristy Hospital*. The project belongs to the Department of Oncology and Medical physics.

Parts of this master thesis are copied from the report of the specialisation project [1] written by the candidate during the spring semester 2021 at NTNU, also in collaboration with the Particle Therapy Research Group at HUH. Results from the specialisation projects have been used in evaluation of the analysis developed in the master project.

ACKNOWLEDGMENTS

I would like to thank my supervisors at HUH, Helge Egil Seime Pettersen, Kristine Fjellanger and Liv Bolstad Hysing. Thank you, Helge, for guiding me and sharing your expertise, which has really motivated me to learn. Thank you for encouraging me to try myself and helping me whenever I needed it. Kristine, I have really appreciated your attendance during this past year. Thank you for everything you have taught me and for understanding my needs. You have provided valuable feedback on my work and motivated me to the last finish. Thank you, Liv, for encouraging me and providing extensive guidance throughout the work of the study and writing the report. Thank you also for including me in your research group. I feel privileged being a master student with my own office next doors to my supervisors and other skilful researchers.

I would also like to thank Kathrine Røe Redalen, my internal supervisor at NTNU. First of all, thank you for introducing me for Liv and making it easy for me to chose the project that I wanted. Thank you also for always being available and making sure that the formal aspects of my degree were in order.

As this is the end of my education, at least for now, I would like to express my gratitude to my family. Thank you for always believing in me and giving me the freedom to decide for myself.

Last but not least, thank you, Sigve, for your patience and invaluable support on good and bad days throughout these past years. I am really lucky for having you by my side.

Vilde Ragnvaldsen
Bergen, January 19 2022

ABSTRACT

Introduction: Intensity modulated proton therapy (IMPT) may potentially improve the treatment of locally advanced non-small cell lung cancer (LA-NSCLC) as compared to intensity modulated radiation therapy (IMRT), which is the current state-of-the-art. Protons provide more precise dose delivery and better sparing of normal tissues. However, since the proton range is highly sensitive to density variations, treatment in the lung region is extra challenging due to breathing motion and anatomical changes. Adaptive protocols are needed, in which analysing the water equivalent path length (WEPL) of the proton beams in the patient could become a useful decision tool. The aim of this study was to evaluate the feasibility of WEPL in adaptive proton therapy of LA-NSCLC by studying the correlation between WEPL changes and target dose degradation.

Materials and methods: Image materials and IMPT plans of 15 LA-NSCLC patients were included in this retrospective study. The patients were treated with IMRT at Haukeland University Hospital, and robust optimised IMPT plans were created retrospectively. Computed tomography (CT) scans were acquired at planning (pCT) and repeated (rCT) in week 1 and week 3 of the treatment course. One patient missed the rCT of week 3, hence 29 rCTs were available. The IMPT plans were recalculated on the rCTs, and the volume of the clinical target volume (CTV) receiving at least 95% of the prescribed dose (V95) was extracted. In order to calculate the WEPL in the CT scans, a stoichiometric calibration was performed, obtaining a conversion from CT number to proton relative stopping power (RSP), characteristic for the applied CT scanner. For every patient, the WEPL was calculated to all points at the distal edge of the CTV in the pCT and in the rCTs. The change in WEPL (ΔWEPL) from the pCT to each of the rCTs was compared to the change in CTV V95 (ΔV95) from the original IMPT plan to the recalculation on the rCTs. The WEPL changes were quantified as the mean and the 95th percentile of $|\Delta\text{WEPL}|$ and the percentage of points at the distal edge of CTV with > 10 mm and > 3 mm WEPL changes.

Results: With the obtained calibration curve, RSP values were predicted with a mean relative error of 4.6% and were used to calculate the WEPL in the patient CT scans. The median of the mean $|\Delta\text{WEPL}|$ for all patients was 5.4 mm in week 1 and 4.5 mm in week 3, and the median percentage of pixels at the distal edge of CTV with $|\Delta\text{WEPL}| > 10$ mm was 13.1% in week 1 and 10.0% in week 3. There was a statistically significant correlation ($p < 0.05$) between the ΔV95 and the percentage of points with $\Delta\text{WEPL} < -10$ mm, being the only tested parameter with correlation. Seven of the 29 recalculated IMPT plans had $\Delta\text{V95} < -1\%$. The ΔWEPL was not significantly different for these than for the plans with less target dose degradation ($p > 0.05$).

Conclusion: In this study, changes in WEPL to the distal edge of the CTV did not correlate with changes in CTV V95. The WEPL is not a feasible tool in adaptive proton therapy of LA-NSCLC with robust optimised IMPT plans.

SAMANDRAG

Introduksjon: Intensitetsmodulert protonterapi (IMPT) kan potensielt gi betre behandling av lokalavansert ikkje-småcella lungekreft (LA-NSCLC) samanlikna med intensitetsmodulert stråleterapi (IMRT) med foton, som er dagens "state-of-the-art". Proton har meir avgrensa doseavsetning og betre sparing av normalvev, men sidan rekkevidda til protona er svært sensitiv til tettleiksendringar, er behandling i lungeregionen spesielt utfordrande. Dette på grunn av pustebevegelsar og anatomiske endringar. Det er behov for adaptive protokollar, kor analyse av den vatn-ekvivalente rekkevidda (WEPL) til protona i pasienten kan vere eit nyttig hjelpemiddel. Målet med denne studien var å evaluere nytta av WEPL i adaptiv protonterapi av LA-NSCLC ved å studere korrelasjonen mellom WEPL-endringar og degradering av dose til målvolumet.
Material og metode: Bilete og IMPT-planar for 15 pasientar med LA-NSCLC blei inkludert i denne retrospektive studien. Pasientane blei behandla med IMRT på Haukeland Universitetssjukehus, og robust optimerte IMPT-planar blei laga i etterkant. CT-bilete blei tekne for planlegging (pCT) og repeterte (rCT) i veke 1 og veke 3 av behandlingsløpet. Ein pasient tok ikkje rCT i veke 3, så 29 rCT-bilete var tilgjengelege. IMPT-planane blei rekalkulert på rCT-bileta, og volumandelen av det kliniske målvolumet (CTV) som mottek minst 95% av den planlagde dosen (V95) blei henta ut. For å rekne ut WEPL i CT-bileta måtte det ei kalibrering til, der CT-tala blei oversett til den relative stoppekrafta (RSP) av proton, karakteristisk for den brukte CT-maskina. For kvar pasient blei WEPL kalkulert til alle punkt i bakkanten av CTV-strukturen i pCT-biletet og i rCT-bileta. Endringa i WEPL (ΔWEPL) frå pCT til rCT blei samanlikna med endringa i CTV V95 (ΔV95) frå den originale IMPT-planen til rekalkuleringa på rCT. Endringar i WEPL blei kvantifisert som gjennomsnittet og 95-percentilen av $|\Delta\text{WEPL}|$ samt prosentandelen punkt i bakkanten av CTV med > 10 mm og > 3 mm WEPL-endringar.
Resultat: Med kalibreringa kunne RSP-verdiar predikerast med ein relativ feil på 4.6% og brukast til å rekne ut WEPL i CT-bileta av pasientane. Medianen av gjennomsnittleg $|\Delta\text{WEPL}|$ for alle pasientar var 5.4 mm i veke 1 og 4.5 mm i veke 3, og medianen for prosentandelen punkt med $|\Delta\text{WEPL}| > 10$ mm var 13.1% i veke 1 og 10.0% i veke 3. Statistisk signifikant korrelasjon ($p < 0.05$) blei funnen mellom ΔV95 og prosentandelen punkt med $\Delta\text{WEPL} < -10$ mm, som den einaste testen med korrelasjon. Sju av dei 29 rekalkulerte IMPT-planane hadde $\Delta\text{V95} < -1\%$. Det var ikkje statistisk signifikant forskjell i ΔWEPL mellom desse planane og planar med mindre dosedegradering.
Konklusjon: I denne studien var det ikkje korrelasjon mellom endringar i WEPL til bakkanten av CTV og endringar i CTV V95. WEPL er ikkje eit eigna hjelpemiddel i adaptiv protonterapi av LA-NSCLC med robust optimerte IMPT planar.

CONTENTS

LIST OF FIGURES

LIST OF TABLES

ACRONYMS

AIP	average intensity projection
CBCT	cone beam computed tomography (CT)
CT	computed tomography
CTV	clinical target volume
DECT	dual-energy CT
DIBH	deep inspiration breath hold
GTV	gross target volume
HLUT	Hounsfield look-up table
HU	Hounsfield unit
HUH	Haukeland University Hospital
IMPT	intensity modulated proton therapy
IMRT	intensity modulated radiation therapy
LA	locally-advanced
LET	linear energy transfer
LINAC	linear accelerator
MRE	mean relative error
NSCLC	non-small cell lung cancer
OAR	organ at risk
PBS-PT	pencil beam scanning proton therapy
pCT	planning CT
PTV	planning target volume
rCT	repeat CT
ROI	region of interest
RBE	relative biologic effectiveness
RSP	relative stopping power
RTT	radiation therapy technician
SOBP	spread out Bragg peak
TPS	treatment planning system
WEPL	water equivalent path length
4DCT	four-dimensional CT

1 INTRODUCTION

Cancer is a widespread disease and the most common cause of death in Norway. One out of three Norwegians gets at least one type of cancer before the age of 75. Lung cancer is the third most common cancer, after prostate cancer and breast cancer, and non-small cell lung cancer (NSCLC) is the most common lung cancer type. In 2020, there were 3331 new cases of lung cancer in Norway, of which men and women contributed almost equally. The five-year relative survival (2016-2020) was 24.7% for men and 31.0% for women [2].

The prognosis for lung cancer patients is poor. The main reason is that the cancer is often discovered too late for curative treatment to be possible. However, from the 1980s until today, the survival rates have more than doubled. At that time, the five-year relative survival (1981-1985) was 7.0% for men and 6.6% for women [2]. The improvement is owed to research and development of better methods for diagnostics and treatment. Methods within radiotherapy have been substantially improved during the past few decades making radiotherapy a cornerstone in cancer treatment today. Radiotherapy can be given with curative or palliative intention, either alone or in combination with other treatments such as surgery, chemotherapy and immunotherapy.

For inoperable locally-advanced (LA)-NSCLC, the standard treatment is curative intended radiotherapy in combination with chemotherapy. Radiotherapy is a local treatment where radiation, most often in the form of high-energy x-ray photons, is sent towards the tumor area aiming to kill the cancer cells. In order to cure the cancer, all cancer cells must be killed [3]. Hence, it is important that the entire tumor volume is covered with sufficiently high radiation dose. A common measure for evaluating the target coverage is the volume of the clinical target volume (CTV) receiving at least 95% of the prescribed dose (CTV V95). At least as important is minimising the dose to healthy tissues. In radiotherapy of lung cancer, there are several organs at risk. High doses to the heart may contribute to fatal toxicity, while doses to the lung tissue may lead to radiation pneumonitis.

Other factors making radiotherapy of lung cancer challenging are anatomical changes and breathing motion. The treatment is typically divided into 30-33 daily fractions, which are planned in advance using medical imaging, normally CT, acquired before treatment start. If anatomical changes occur during the treatment course, it may jeopardize the quality of the planned treatment, having reduced dose to the tumor or increased dose to healthy tissues [4]. If the tumor or surrounding organs move due to breathing while the treatment is given, it may have the same effect. Robust planning and mitigation strategies have been developed to maintain the treatment quality despite smaller anatomical changes and breathing motion. To overcome larger anatomical changes, ad-

aptive radiotherapy could be needed. That involves changing the entire treatment plan, which is a demanding process involving additional imaging and replanning.

In patients with LA-NSCLC, toxicity and local recurrence of the cancer are common problems after radiotherapy [4]. Increasing the radiation dose could theoretically improve the outcome by reducing the risk of local recurrence, but the possibilities are limited due to the potentially fatal side effects occurring if sensitive organs are exposed to high doses [5]. A clinical study from 2019 found reduced overall survival with higher doses, and concluded that today's standard should remain the standard of care for photon radiotherapy of LA-NSCLC [6].

In 2024, a new type of radiotherapy treatment is going to be introduced in Norway, namely proton therapy. The use of protons in radiotherapy has the great potential of providing a more precise radiation dose to the tumor and better sparing of healthy tissues, as compared to photons. Especially with intensity modulated proton therapy (IMPT), it may be possible reduce side effects and facilitate dose escalation in LA-NSCLC patients [7, 8]. Results from clinical trials show low toxicity rates [9]. However, there are some inherent uncertainties in proton therapy making treatment in the lung region challenging.

The proton range inside the body is highly sensitive to variations. A small amount of additional tissue in the beam path can misplace the precise delivery of the dose, resulting in reduced target coverage and high dose to healthy tissues. With robust optimisation, anticipated changes can be incorporated into treatment planning, but to account for unforeseen major anatomical changes, it is believed that frequent adaptions are needed when treating LA-NSCLC with IMPT [4, 10].

Adaptions will probably not be necessary for all LA-NSCLC patients in proton therapy, but adaptive protocols to identify those who need it is important, and yet to be developed. In photon therapy, adaptive protocols typically involve visual inspection of cone beam CT (CBCT) scans acquired before every treatment fraction. If anatomical changes with possible dosimetric impact are observed, replanning may be triggered. In proton therapy, the dose can be deteriorated by small variations that are not visible on CBCT. Studies have suggested that the treatment plan should be simulated on weekly repeat CT (rCT) scans in order to monitor the dose distribution during the treatment course [10]. However, rCT scans require more resources when it comes to clinical personnel and time, and it leads to additional stress and radiation dose to the patient.

Calculation of the water equivalent path length (WEPL) of protons inside the body may be a useful decision tool in adaptive proton therapy. Quantitatively assessing changes in WEPL could give an indicator on anatomical changes or other changes that are affecting the proton dose delivery. The WEPL can be calculated from a CT scan of the patients anatomy. The Hounsfield unit (HU) values of the CT scan, which are measures of the x-ray attenuation, are converted to the proton stopping power relative to water (relative stopping power (RSP)). Then, integrating the RSP values of the traversed tissues along the beam path results in a water equivalent measure of the proton range. The WEPL calculation is faster than full dose calculation and could be used online on rCTs to monitor the dose delivery during the treatment course. In a study from 2017, it was concluded

that change in WEPL is an indicator of IMPT plan robustness and should be considered for use in adaptive therapy [11]. Also previous studies have found positive correlations between changes in WEPL and dose degradation [12, 13].

A more advantageous use of WEPL would be to connect it to the daily CBCT scans, so that additional rCTs are not needed. The WEPL calculations could then be used as a pre-treatment range check at every fraction, and to decide if adaptions should be considered [14]. However, the image quality of CBCTs is inferior to the standard CT scans due to more photon scattering [15]. The uncertainty in the HU vales translate into uncertainty in the WEPL calculation [16]. Even with the standard single-energy CT scans, proton range margins of 3.5% are typically used to account for uncertainties related to the RSP estimation [17, 18]. This uncertainty will be larger for cone beam CT (CBCT)s, unless advanced scatter corrections are applied. Before implementing CBCT based WEPL calculations, the feasibility of using WEPL in adaptive proton therapy should first be validated on standard CT scans.

1.1 AIM

The overall aim of this study was to explore the feasibility of using WEPL as a decision tool in adaptive proton therapy of LA-NSCLC.

In the first part, the aim was to develop an algorithm for calculating the WEPL between two points in a CT scan. A part of this involved implementing an algorithm presented by a former master student on converting CT numbers into RSP values.

The second aim was to perform WEPL calculations in CT scans of 15 LA-NSCLC patients. The WEPLs should be computed along the proton beam paths from the edge of the CT image to the distal edge of the tumor volume.

The third aim was to investigate whether WEPL differences from planning CT (pCT) scans to rCT scans could be used to predict dose deterioration in IMPT plans.

1.2 HYPOTHESES

The following hypotheses were made to aid the investigation of the feasibility of WEPL in adaptive proton therapy of LA-NSCLC:

1. "A conversion from HU values to RSP values for the applied CT scanner can be performed with an accuracy of 3.5%, and be used to calculate the WEPL between two points in a CT scan."

2. "Calculating WEPL to the distal edge of CTV in pCTs and rCTs and recalculating IMPT plans on the rCTs for a group of patients, there is a statistically significant correlation between the change in WEPL and the change in CTV V95."

3. "The WEPL changes are significantly larger for patients with more than 1% reduction in CTV V95 in the recalculated IMPT plans than for those with less target dose degradation."

2

THEORY

2.1 LUNG CANCER

The lungs reside in the thoracic cavity in the chest (Figure 2.1). They are surrounded by the fluid filled pleural space, where the lungs move smoothly when we breathe [19]. Between the lungs resides the mediastinum, which contains systemic blood vessels and lymph nodes. The diaphragm is a muscle which contracts when we inhale, so that the lungs enlarge and are filled with air.

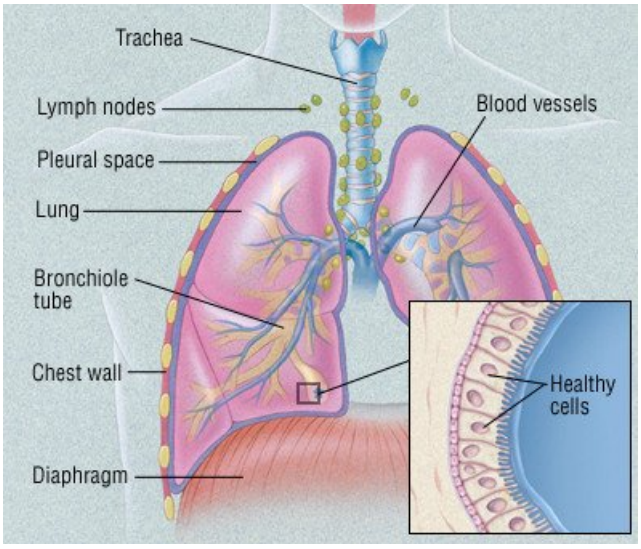

Figure 2.1: Anatomy of the lungs. Figure from [20].

The lungs, as any other organ, consist of many different types of cells. Under normal conditions, these cells grow and die in a specific cycle, keeping the number of cells in check. If mutations occur in the genes, the cell cycle may change and unregulated cell division can lead to an increased number of cells that form tumors. These tumors can be malignant, meaning that they can invade normal tissues and spread. When the malignant cells originate from the lungs, it is lung cancer. The spreading is known as metastasis. Lung cancer commonly metastasises to lymph nodes in the thorax and especially in the mediastinum. Cancer cells can also break away from the primary tumor and travel through the lymph system or vessels to other parts of the body such as the bones, liver or brain, where they form distant metastases [21].

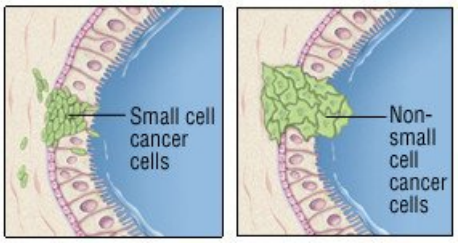

Figure 2.2: In developing lung cancer, healthy cells (Figure 2.1) turn into cancer cells. Small cell cancer cells divide more rapidly making small cell lung cancer very aggressive. Non-small cell cancer cells are larger and divide more slowly. Figure from [20].

2.1.1 Non-small cell lung cancer

There are two main types of lung cancer (Figure 2.2). The most aggressive one is small cell lung cancer, characterized by small cells that tend to divide rapidly. The most common type is non-small cell lung cancer (NSCLC), which accounts for about 85% of all lung cancer cases in Norway [21].

Based on the size of the primary tumor and possible metastases, NSCLC is staged from I to IV. The TNM staging system 8th edition [22] includes three categories - primary tumor (T), regional lymph nodes (N) and distant metastasis (M). Staging of the cancer gives an indicator for which treatment is most suitable and what are the prognosis for survival. At stage I lung cancer, the tumor is confined to the primary organ and the five year survival $(2016 - 2020)$ is 72.8% for women and 63.9% for men. At stage III, the tumor may have progressed or spread to regional lymph nodes, and the five year survival is 35.8% for women and 30.4% for men [2]. Stage III lung cancer is often referred to as locally-advanced (LA) and is the topic of this thesis.

2.1.2 Locally advanced NSCLC

About 40% of all NSCLC are LA at the time of diagnosis [23]. At this stage there is no distant metastases, but the cancer may have spread within the chest. To which degree regional metastases have occurred varies within this stage, and so does the size of the primary tumor. Generally, LA-NSCLC can be defined as:

- a primary tumor that is more than 7 cm in the largest dimension, and/or
- a primary tumor invading intrathoracic structures such as the diaphragm, mediastinum, heart or esophagus, and/or
- separate tumor nodule(s) in a different ipsilateral lobe than the primary tumor, and/or
- metastasis to regional lymph nodes [22, 24].

Stage III NSCLC is further divided into IIIA, IIIB and IIIC. Figure 2.3 shows an example of stage IIIA and stage IIIB. Tables for the TNM classification are presented in Appendix A.

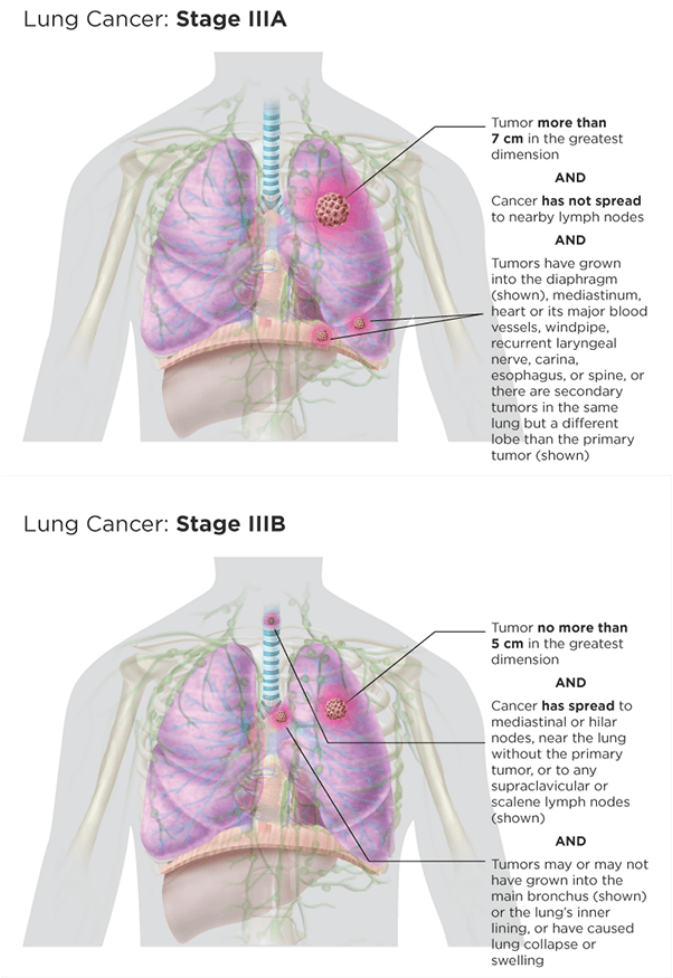

Figure 2.3: Stage III NSCLC is further divided into IIIA, IIIB and IIIC. Stage IIIA can involve a primary tumor larger than 7 cm and invasion to intrathoracic structures. Stage IIIB lung cancer can be a primary tumor smaller than 5 cm that has spread to regional lymph nodes and may have grown into the main bronchus. Figures from [24].

2.1.3 Treatment of LA-NSCLC

Patients with inoperable LA-NSCLC that show good general condition, usually get curative-intended photon radiotherapy in combination with chemotherapy. The radiotherapy gives local treatment of the primary tumor and known metastases, while the chemotherapy is a systemic treatment for potential micro-metastases [23]. Radiotherapy aims at killing cancer cells, but it is unavoidable also to irradiate normal cells surrounding the tumor. Lung tumors are often located close to critical organs or structures, in which toxicities may occur if they are irradiated. Also local recurrence is a major contribution to the bad prognosis for this patient group. Dose escalation can theoretically

improve the outcome, but the possibilities are limited due to the potentially fatal side effects [5].

Proton therapy has the potential to reduce side effects due to more precise treatment allowing better sparing of normal tissue. Phase II clinical trials have shown promising results for using protons in treatment of LA-NSCLC [25–27], but a randomised trial by Liao and colleagues in 2018 [28] showed no advantage of proton therapy over modern radiotherapy with photons. Due to the lack of evidence on improved local control, survival or less side effects, protons are not used in treatment of LA-NSCLC in Norway [23]. However, these clinical trials have mainly been for old delivery techniques, while the state-of-the-art technique is called pencil beam scanning proton therapy (PBS-PT), and has a greater potential of sparing critical organs in radiotherapy for thoracic cancer [7, 29]. With the development of more advanced techniques, it is believed that protons can give LA-NSCLC patients better prognosis [4, 10].

2.2 RADIOTHERAPY

In radiotherapy, ionising radiation is sent towards the tumor aiming to kill cancer cells. The target is the DNA molecule, of which the ionisation might lead to single strand breaks or double strand breaks. Most single strand breaks are repaired by the cells themselves, while the repair process for double strand breaks can become very complex with a high probability of misrepair. Incomplete repair, inhibits the cells' reproductive capability and might induce cell death. In order to cure cancer, all cancer cells must be killed [3].

2.2.1 Radiotherapy treatment modalities

Radiotherapy can be given externally, from outside the body, or internally, from the inside. In internal radiotherapy, a radiation source is placed inside the tumor or in close proximity to it. External radiotherapy is given from outside the body by accelerating particles or photons towards the tumor. Radiotherapy using x-ray photons is the most used modality in Norway today. This is electromagnetic radiation that is generated by accelerating electrons in a linear accelerator (LINAC) and sending them towards a heavy metal target to produce high-energetic photons. The accelerated electrons can also be used directly in radiotherapy treatment of tumors that are located no more than 5 cm under the skin surface, whilst photons can reach further into the body [3].

Protons are heavier particles that are increasingly used for cancer treatment. Because of their heavy mass, more complex and expensive equipment such as a cyclotron is needed to accelerate them to useful energies. Protons can be used in treatment of both deep- and shallow-seated tumors and can potentially increase the sparing of healthy tissue as compared to x-ray photons [3, 8].

Further in the thesis, the focus will be on external radiotherapy with photons and protons, which are the relevant modalities in treatment of LA-NSCLC. In Norway, today's

standard treatment for this patient group is photon radiotherapy, but with proton centers coming in 2024, the question is if proton therapy could improve the treatment.

2.2.2 Absorbed dose, linear energy transfer and relative biological

When ionising radiation interacts with biological cells, energy is deposited with the potential of damaging the cells' DNA. The amount of energy absorbed per unit mass of tissue is defined as absorbed dose, a physical quantity with the unit Gray (Gy). One Gy corresponds to one J/kg.

The energy transferred per unit length of a particle track is referred to as linear energy transfer (LET). For any type of charged particle, the higher the energy, the lower is the LET. For instance, the LET of 10-MeV protons is 4.7 keV/μm, while for 150-MeV protons the LET is 0.5 keV/μm. The LET is higher for protons than for photons. For 250-kV x-rays the LET is 2.0 keV/μm [3].

The LET of the radiation, as well as the dose and the intrinsic radiosensitivity of the tissue, affects the type of damage and the capacity of the cell to repair [30]. Equal doses of different types of radiation do not produce the same biological effect. When comparing different modalities, a scaling parameter is needed. The relative biologic effectiveness (RBE) of a given radiation r is defined by the ratio D_{250}/D_r, where D_{250} and D_r are the absorbed doses of 250-kV x-rays and r, respectively, required to produce the same biological effect [3]. Clinically, a concervative and constant RBE of 1.1 is used for protons, meaning that protons are considered to be 10% more effective than x-rays, which have an RBE of 1.0. Experiments have shown that the RBE of protons actually varies with biological and physical quantities. There are lots of ongoing research on developing models for the varying RBE. Doses in proton therapy are usually prescribed as Gy(RBE) to reflect that the absorbed dose (Gy) was multiplied with an RBE value [30, 31].

2.2.3 Dose deposition of photons and protons

Photon radiation is indirectly ionising, meaning that photons do not produce damage to the DNA directly, but they give up energy to produce fast-moving secondary particles, such as electrons, that in turn can damage the DNA. Hence, when photons enter the body, the absorbed dose is low in the start and builds up as more secondary particles are generated. After a maximum, the dose gradually decreases with depth [3]. A typical depth-dose curve for photons is shown in Figure 2.4 together with one for protons, which is quite different.

Protons are directly ionising, meaning that they produce damage to the DNA themselves. Hence, the high-dose region can be better confined to the target volume. When a beam of high-energy protons enters the body, it is sparsely ionising, meaning that the LET is low and so is the deposited dose. When travelling through tissue, the protons start slowing down as they lose energy to the tissue. As the particle slows down, the LET increases and so does the the dose to the tissue. At a certain depth, the dose in-

creases more rapidly and reaches a sharp maximum, called the Bragg peak (Figure 2.4). After this peak the dose falls rapidly to zero, which is the end of the proton range. A spread out Bragg peak (SOBP) can be generated by applying multiple proton beams of varying intensities and ranges [3, 7].

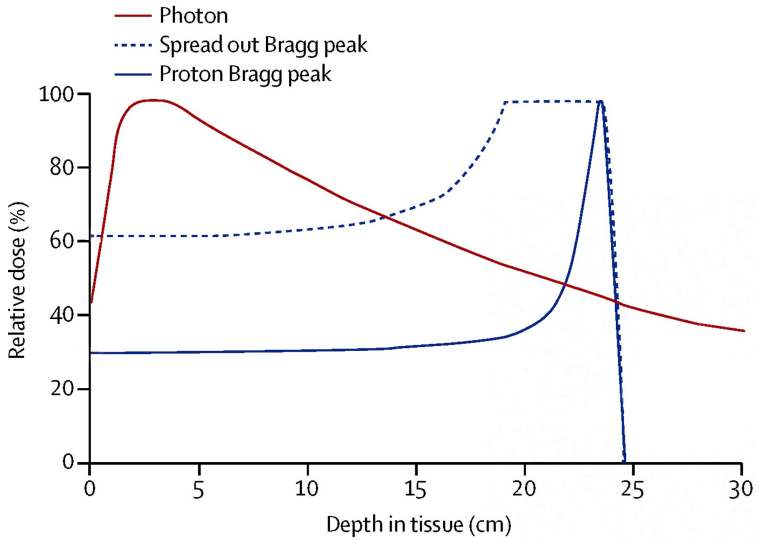

Figure 2.4: Typical depth-dose curves for a photon beam in red and a proton beam in blue. The dotted blue curve shows the spread out Bragg peak (SOBP) generated by summing several proton beams of different intensities and ranges. Figure adapted from [32].

As can be seen from Figure 2.4, the exit dose of protons after the Bragg peak is close to zero, while photons deposit dose also to tissue behind the tumor. For the same dose to the target volume, protons deliver a lower dose to surrounding normal tissues (Figure 2.5). Protons are increasingly used for cancer treatment because of their favorable dose distribution.

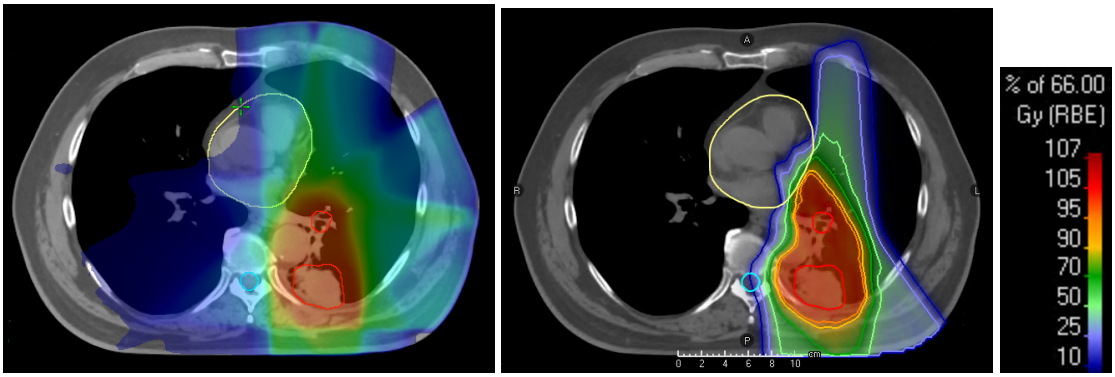

Figure 2.5: Dose distribution of treatment plans for IMRT (left) and IMPT (middle) of LA-NSCLC. The target volume is delineated in red. There is a primary tumor in the lower part of the lung and a metastasis in the mediastinum. The the heart is delineated in yellow and the spinal cord in cyan. The colors show the dose on a scale (right) from 10% to 107% of the prescribed dose, which in this plan is 66 Gy(RBE).

2.2.4 Modern radiotherapy delivery techniques

Radiotherapy with photons or protons is usually delivered from several beams irradiating from different angles. In photon radiotherapy, intensity modulated radiation therapy (IMRT) involves modulating the intensity of each individual field resulting in a homogeneous dose confined to the target volume and minimised dose to surrounding tissue. A specialised collimator is used to conform the radiation fields to the target volume avoiding healthy tissue.

In proton therapy, the localisation of dose in each individual Bragg peak provides the possibility of modulating the intensity within each field, analogously to IMRT. Intensity modulated proton therapy (IMPT) can be delivered with state-of-the-art pencil beam scanning proton therapy (PBS-PT). In PBS-PT, each field consists of individual radiation beams, referred to as pencil beams, that are scanned across the target with the use of magnets. The dose is delivered spot by spot in the individual Bragg peaks. By regulating the intensity and range of each pencil beam and the weighting of the Bragg peaks, the intensity profile of the field can be modified. An alternative technique is passive scattering, in which the proton field is passed through a rotating wheel with sectors of varying thickness, obtaining beams of varying intensities and ranges which can be summed to create a SOBP [3, 7, 33].

2.2.5 Treatment uncertainties in proton therapy

The precise delivery of high doses also makes proton therapy very sensitive to variations. A small change in tissue density may lead to overshooting or undershooting of the Bragg peaks, both being undesirable scenarios. Overshooting means that the proton range is increased so that proximal parts of the target get too low doses and normal tissue positioned behind the target receive unacceptably high doses. Conversely, undershooting leads to a lack of dose in distal parts of the target volume and high doses to normal tissue positioned in front of the tumor [16].

In planning of proton therapy, the proton range in the patient should be predicted as accurately as possible. However, an uncertainty in the proton range of 3.5% plus an additional 1 mm margin is typically assumed in treatment planning. That corresponds to an over- or undershoot of 8 mm in a 20 cm range field in soft tissue, which is substantial [17]. A major contribution to the uncertainty is the prediction of the proton range based on CT images, which will be discussed later in this thesis. Other uncertainties come from setup variations, organ motion and anatomical changes during treatment. There are also uncertainties due to approximations in the dose calculation and biological considerations [15, 17].

Breathing motion must be taken into account in radiotherapy treatment of lung cancer. During the respiration cycle the lung volume changes and the amount of tissue in the beam path varies. The breathing motion might also move the target away from the field, resulting in a underdosage of the target. Several motion management techniques have been implemented to account for this uncertainty. One method is to adjust the

treatment to the free breathing pattern of the patient. The patient breathes normally during treatment, and the target volume encompasses all the potential tumor positions during respiration. In proton therapy, state-of-the-art PBS-PT becomes much more complicated in treatment of lung tumors due to an interplay effect between the pencil beam scanning and organ motion [15, 34]. Another mitigation strategy is deep inspiration breath hold (DIBH). Having the patient to hold their breath during treatment delivery, minimises motion uncertainties as well as it can increase the distance between the target and surrounding critical organs, such as the lung tissue and the heart, and thus reduce the dose to these organs [35]. This strategy relies on patient compliance and reproducibility [36].

Variation in patient setup during treatment also contributes to uncertainties. It is highly important that the patient is positioned similarly at treatment as on the planning CT, so that the amount of tissue in the beam path is the same. Otherwise, the deposition of the high doses may be displaced. In proton therapy the individual beam intensities can be optimised accounting for several uncertainty scenarios coming from breathing motion, setup or range uncertainty. That is called robust optimisation [7].

As mentioned, proton therapy uses an RBE of 1.1 to weigh proton doses compared to photon doses, but the proton RBE actually varies between patients and throughout the beam path. Within the SOBP the LET increases causing an increase in RBE at the distal edge of the SOBP. Treatment planning with variable RBE values is not done clinically because of significant uncertainties [30]. The dose calculation using a constant RBE of 1.1 also contributes to uncertainties in the treatment planning [17, 34].

2.2.6 Imaging for radiotherapy

Medical imaging is an indispensable part of radiotherapy. First of all, imaging is used in diagnosing the cancer. Computed tomography (CT) is often used along with magnetic resonance imaging (MRI) and/or positron emission tomography (PET) to localise the tumor and distinguish it from surrounding healthy tissue [15].

Planning the radiotherapy treatment involves setting up the radiation fields to best achieve the prescribed dose to the target and restricted dose to surrounding tissues. CT is the most used imaging method for treatment planning since it provides information about electron density in the different tissues, which is used for calculating the absorption of radiation.

To image organs in the thorax region, which move while the patient breathes, four-dimensional CT (4DCT) scans are often useful. That involves taking CT scans continuously during free breathing resulting in a data set representing the different phases of the respiration cycle. Separated image series for the different phases can be reconstructed, as well as an average intensity projection (AIP) of the CT scans in the different phases. An alternative to this is avoiding breathing motion by acquiring the CT scan while the patient holds their breath (DIBH).

Imaging is also used in connection with treatment delivery to make sure that the patient is positioned correctly relative to the coordinate system of the treatment machine

and to monitor changes in the anatomy during the treatment course. Orthogonal X-ray radiograph systems are parts of all photon and proton delivery systems, and some have onboard scanners mounted to the gantry which can be used for CBCT acquisition. For image guidance in treatment of lung cancer, CBCT is most often used [15]. How the CT and the CBCT works is explained in more detail in Section 2.4.

2.2.7 The radiotherapy workflow

Delineation

After diagnosis and acquisition of the planning CT (pCT), a treatment plan is made. The first step of planning is delineation of target volumes (Figure 2.6) and organs at risk (OARs) in the CT image. The structure of the visible tumor volume is called the gross tumor volume (GTV), while the internal gross tumor volume (IGTV) includes the position of the tumor in all phases of the 4DCT. The clinical target volume (CTV) includes the IGTV and an additional margin accounting for any microscopic extension of the tumor. The planning target volume (PTV) includes the CTV and a safety margin accounting for changes in the CTV and expected patient motion and variations in position and setup. [4]. For LA-NSCLC, there are typically several separated target volumes as there may be metastases in addition to the primary tumor. Typical OARs are the lungs, heart, esophagus, brachial plexus and spinal cord.

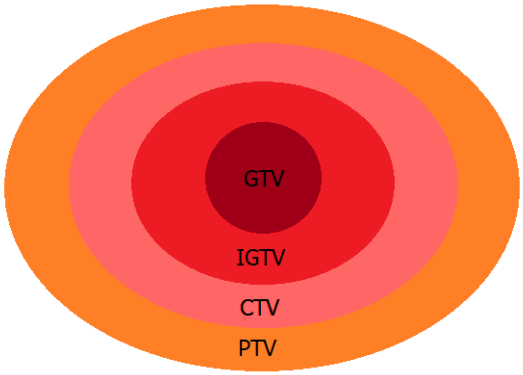

Figure 2.6: Schematic presentation of volumes typically delineated for treatment planning. *Abbreviation:* GTV = gross tumor volume, IGTV = internal gross tumor volume, CTV = clinical target volume, PTV = planning target volume. Figure adapted from [37].

Treatment plan setup

The next step of the treatment planning is defining the angles of the incident radiation fields, which is done based on the location of the tumor relative to healthy tissue. Then desired qualities of the treatment plan are defined. These typically include a desired dose to the target volume and constraints for dose to OARs and other normal tissue. Based on an optimisation algorithm, the treatment planning system (TPS) calculates the properties of the beams in order to achieve these qualities.

Robust optimisation

The PTV includes a margin that should ensure dose coverage of the CTV with an acceptably high probability, despite changes in the target and variations in patient position and setup [37]. In proton therapy, however, such margins could be problematic due to the steep dose gradients and high RBE at the distal edge of the beam, causing more injury to normal tissues. In addition, margins may have little of the intended effect in IMPT, especially in heterogeneous tissues such as the lungs and for highly modulated plans. The position of each individual Bragg peak depends on the density of the traversed tissues, and a change leads to a distorted dose distribution [29]. More complex procedures have been introduces to IMPT planning, such as robust optimisation [7, 38].

In robust optimisation, uncertainties due to changes in patient position, setup and changes in proton range inside the patient are included in the optimisation problem, which typically aims at minimising the penalty of the worst case scenarios. The optimisation algorithm searches for the spot weight configuration that is the least sensitive to these uncertainties [38]. This is often referred to as 3D robustness. By also including variations due to breathing motion into the planning, obtained from a 4DCT scan, a plan can be made 4D robust, which may reduce the interplay effects in treatment of lung cancer with PBS-PT.

Treatment plan evaluation

The TPS calculates the distribution of dose to the different structures delineated in the pCT image. To evaluate the plan quality, quantitative dose parameters can be retrieved. Some parameters that are typically used in evaluating the target coverage are CTV V95, which is the volume of the CTV receiving at least 95% of the prescribed dose, and CTV D98, which is the dose that covers at least 98% of the CTV. For OARs, other dose-volume parameters that are correlated with side effects are use for evaluation. Also mean doses are used for the lungs and the heart.

Treatment delivery

Conventional radiotherapy treatment is usually delivered in separated fractions. For LA-NSCLC the standard is to divide the treatment into 30-33 fractions, and treat with one daily fraction 5 times a week. Since the treatment is thoroughly planned on a pCT scan, it is important that the patient is positioned similarly at every treatment fraction as on the pCT. Fixation tools are used to position the patient correctly, and pre-treatment imaging is used for matching the coordinate systems of the treatment machine and the patient. The images acquired before every treatment fraction are also used for monitoring the anatomy of the patient throughout the treatment course. If large anatomic changes occur during the treatment course, the planned treatment may not fulfill the desired qualities anymore. That brings us to adaptive radiotherapy.

2.2.8 Adaptive radiotherapy

Adaptive radiotherapy involves changing the treatment plan during the course of treatment. Adaptions may be needed to incorporate anatomical changes that have occurred after the pCT was taken, degrading the planned treatment by either having too low target coverage or depositing high doses in healthy tissue.

The impact of anatomical changes

For patients with LA-NSCLC, anatomical changes commonly occur during the course of treatment, either spontaneously or induced by the radiation. These changes may have a large impact on the dose distribution in radiotherapy, and especially in proton therapy. Common changes in this patient group are atelectasis, which is a collapse of lung tissue, and pleural effusion, which is accumulation of fluid in the pleural space due to the cancer or an infection. These changes can increase the tissue density along the beam path, which shortens the proton range and deteriorates the target coverage. Tumor progression can also have this effect. In contrast, tumor regression and patient weight loss can reduce the density along the beam path and increase the proton range, which can result in increased dose to surrounding healthy tissues [14]. Baseline shifts of the tumor position relative to a reference, for instance the bony anatomy, are also common. If these changes are not discovered and the original treatment plan is used throughout the course, it can reduce the quality of the treatment, potentially with severe consequences [4, 21].

Adaptive protocols

Anatomical changes can be observed visually on the CBCT scans taken before every treatment. If the radiation therapy technician (RTT) discovers significant anatomical changes, an oncologist or physicist evaluates the need for adaption. If needed, a new CT scan is acquired and the treatment is replanned. This is a typical protocol in photon radiotherapy of lung cancer. However, not all changes are easy to spot on the CBCT. In a specialisation project performed by the candidate in 2021, it was found that the severity of anatomical changes observed on CBCT scans by RTTs did not correlate with degradation in dose in neither IMRT nor IMPT treatment of LA-NSCLC [1].

In proton therapy, even the smallest change in density may misplace the Bragg peaks. Robust optimisation partly considers the association between geometrical changes and the dosimetric consequences, but the optimisation cannot consider unforeseen anatomical changes [4]. Studies have suggested that about 30% of IMPT plans on lung cancer would require adaptions even with robust optimisation [29, 39]. According to the PTCOG's consensus guidelines for implementing PBS-PT for thoracic malignancies [10], all patients should undergo weekly 4DCT verification simulations to determine whether adaptive replanning is needed to maintain plan robustness. As most plans are valid without adaptions, the additional CT scans may expose the patients for unnecessary

stress and excess dose. Adaptions are highly recommended when treating LA-NSCLC with IMPT [4, 10, 38], but there is a lack of adaptive protocols.

One potential approach is to use the CBCT scans, which are acquired at every treatment fraction, to calculate the water equivalent path length (WEPL) of the proton beams in the patient. The WEPL can be used as a proton range check before delivering the treatment, and give an indication on whether adaptions are necessary. Calculating the WEPL from a CT scan involves converting the CT numbers, which are measures of the attenuation of photons in the body, into proton stopping powers. This calculation, which is explained in more details in Section 2.6, is quite complicated, since photons and protons interact differently with matter.

2.3 INTERACTIONS OF IONISING RADIATION WITH MATTER

Ionising radiation can be classified as directly or indirectly ionising. Protons and electrons are charged particles and directly ionising, causing chemical and biological damage to the DNA directly by ionising the absorbing atoms. Photons, on the other hand, are neutral particles and are indirectly ionising meaning that they do not cause damage to the DNA directly, but release secondary particles that in turn produce damage [3].

2.3.1 Photon-Matter interactions

As the photon beam travels through matter, the beam is attenuated, meaning that photons are removed from the beam and absorbed in the traversed material. The intensity I of the travelling X-ray beam is given by

$$I(x) = I_0 e^{-\mu x}, \tag{2.1}$$

where I_0 is the initial intensity of the beam, x is the thickness of the traversed material and μ is the linear attenuation coefficient of the material. The linear attenuation coefficient μ is given as

$$\mu = n\sigma, \tag{2.2}$$

where n is the number of atoms per unit volume and σ is the total interaction cross section per atom. The interaction cross section is an effective measure of the probability for interaction between a photon and an atom [40]. The type of interaction depends on the energy of the incoming photon and on the chemical composition of the absorbing material [3]. The total cross section can be written as the sum of the the processes contributing to the attenuation. At photon energies relevant for medical imaging (up to 100 keV),

$$\sigma(E) = \sigma_C(E) + \sigma_R(E) + \sigma_p(E), \tag{2.3}$$

where $\sigma_C(E)$, $\sigma_R(E)$ and $\sigma_p(E)$ are the atomic cross sections for Compton scattering, Rayleigh scattering and photoelectric effect, respectively [41].

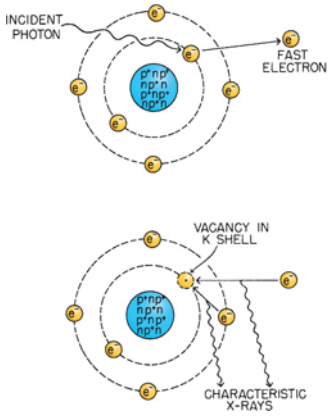

Figure 2.7: Photoelectric absorption. Figure from [3].

Photoelectric effect

At lower photon energies (up to 30 keV in water) photoelectric absorption is the dominating interaction. In photoelectric absorption, the photon is absorbed by an atom, which is left in an excited state (Figure 2.7). The excess energy is released by the ejection of a tightly bound orbital electron with energy $T = E - E_s$, where E_s is the binding energy of the electron and E is the energy of the incoming photon. The ejected electron leaves behind a vacancy in the atom. The vacancy is filled by an electron from a higher shell, a process which releases a characteristic electromagnetic radiation (fluorescent X-ray) or an electron from a higher shell, known as an Auger electron. The new vacancy will then be filled, and this process continues in a cascade of events that may finally leave the atom in an ionised state. The photoelectric absorption's cross section per atom, σ_p, is proportional to Z^4/E^3, where Z is the atomic number of the absorber [40]. Thus, the probability of this interaction increases with increasing atomic number and with decreasing energy.

Compton scattering

Compton scattering dominates at higher photon energies (above 30 keV in water). That is when the incoming photon interacts with an atomic electron whose binding energy is negligibly small compared to the photon energy. Part of the photon's energy is given to the electron as kinetic energy, which is released as a fast electron that can ionise surrounding atoms (Figure 2.8). The photon continues travelling with reduced energy and can eject more electrons. The energy transferred to the recoil electron is largest when the photon is backscattered, and is zero in the forward direction [40]. The probability of Compton scattering increases linearly with Z, as larger atoms have more outer electrons.

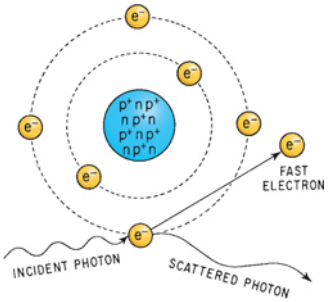

Figure 2.8: The Compton scattering process. Figure from [3].

Rayleigh scattering

Another possible interaction is coherent Rayleigh scattering, in which the incoming photon is scattered at a small angle when interacting with an atomic electron (Figure 2.9). No energy is transferred to the electron. Determining the atomic cross section σ_R for Rayleigh scattering involves integrating over all possible scattering angles. This becomes a complicated expression depending on the scattering angle θ, the atomic number Z and the energy of the incoming photon [40]. In medical imaging, the scattered radiation contributes to image noise if recorded by the detector. It may also increase the radiation dose to the patient or to clinical personnel standing close to the patient.

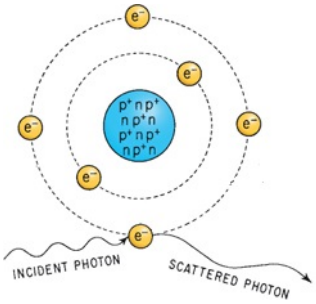

Figure 2.9: Rayleigh scattering. Figure adapted from [3].

The total cross section

Taking into account the cross sections for the different interactions, the total photon cross section can be parametrised as

$$\sigma(E,Z) = k_C(E)Z_i + k_R(E)Z_i^{2.86} + k_p(E)Z_i^{4.62}, \tag{2.4}$$

with a certain degree of accuracy. Here Z is the atomic number of the absorbing material, $k_C = \sigma_C(E)/Z$ is the electronic cross section for Compton scattering [42], and $k_R = 2.80E^{-2.02}$ and $k_p = 20.64E^{-3.28}$ are the Rayleigh and photoelectric coefficients, respectively, parametrised as functions of the photon energy, E [41, 43]. Inside the body, travelling photons are absorbed to a greater degree by materials of high atomic number Z, such as calcium in bones. At high energies, where Compton scattering dominates, this effect is not that prominent, but at lower energies, where photoelectric effect

dominates, there is a stronger dependence of Z in the attenuation of photons. Different degrees of attenuation in different tissue types provides contrast in medical imaging. Hence, lower energies are most often used in medical imaging.

2.3.2 Proton-Matter interactions

Protons are charged particles and directly ionising. In therapy, the entrance proton energy is typically between 150 and 250 MeV [34]. When travelling through matter, three types of interactions occur.

The first is a Coulomb interaction between the proton and atomic electrons resulting in an ionised atom and a free electron that can further ionise other atoms. The proton mass is about 1840 times the one of an electron [44]. Due to the larger mass, the proton is not deflected from its trajectory and loses only a small fraction of its energy. Through multiple such collisions the proton will finally lose all its energy and stop. These inelastic interactions result in a longitudinal dose distribution [34].

Protons can also be subject to elastic interactions with the positive atomic nuclei, in which the protons are deflected. This is an elastic interaction where the proton loses only a small amount of energy. From multiple scatterings, the effect is lateral broadening of the beam. The third possible interaction is a nuclear interaction with the atomic nucleus, which reduces the intensity of the primary beam and contribute to both longitudinal and lateral dose profiles [34].

Proton stopping power

In the inelastic Coulomb interaction with atomic electrons, the amount of energy transferred from the proton in each interaction has a probability distribution, which results in energy- and range straggling. In practise, energy- and range straggling for clinical proton beams can be assumed to have a nearly Gaussian distribution. Hence, not all protons in a monoenergetic beam will have the same range [34, 44]. As an estimate, the proton electronic stopping power of a given material is given by the Bethe-Bloch formula, simply expressed as

$$S_{el} = \rho_e \frac{4\pi e^4}{m_e c^2 \beta^2} L(I, \beta). \tag{2.5}$$

Here ρ_e is the electron density of the stopping material, $m_e c^2$ is the electron rest energy, β is the velocity of the proton in units of speed of light and $L(I, \beta)$ is the stopping number [45]. With I being the ionisation energy (I-value) of the material, the stopping number can be expressed as

$$L(I, \beta) = \ln \frac{2 m_e c^2 \beta^2}{1 - \beta^2} - \beta^2 - \ln I. \tag{2.6}$$

This is referred to as the Fano's term and contains corrections to the Bethe-Bloch formulation [45]. In the above expression, shell and density corrections are neglected.

In a compound material, the I-value can be estimated by the Bragg additivity rule,

$$\ln I = \frac{\sum_i w_i \frac{Z_i}{A_i} \ln I_i}{\sum_i w_i \frac{Z_i}{A_i}}, \tag{2.7}$$

where Z_i, A_i and w_i are the atomic number, the atomic weight and the weight fraction of an element i in the material composition [46]. The I-values of elemental substances I_i in solid states can be found from tables developed by Berger and Seltzer in 1982 [46]. These elemental I-values are used clinically to calculate the I-values of human body tissues. As argued by Bär et al. [47], there are uncertainties related to this as the I-value of an element depends on whether it is unbound or bound, and on the types of chemical bonds. Many attempts on optimising the I-values for body tissues have been carried out, for instance by Bär et al..

The proton electronic stopping power relative to the one of water is referred to as relative stopping power (RSP) and can be written as

$$\text{RSP} = \frac{\rho_e}{\rho_{e,w}} \frac{L(I,\beta)}{L(I_w,\beta)}, \tag{2.8}$$

where ρ_e, $\rho_{e,w}$ are the electron densities and I, I_w are the I-values of the material and of water, respectively [41]. Hence, RSP can also be expressed as the relative electron density $\hat{\rho_e} = \rho_e/\rho_{e,w}$ times the relative stopping number $\hat{L} = L/L_w$,

$$\text{RSP} = \hat{\rho_e}\hat{L}. \tag{2.9}$$

That means that the RSP is directly proportional to the relative electron density, $\hat{\rho_e}$, of the material.

2.4 COMPUTED TOMOGRAPHY

Computed tomography (CT) is an imaging modality using x-ray photons as radiation source. When imaging, the patient lies on a table that moves through a rotating gantry, which contains a radiation source and detectors (Figure 2.10). For many angles, as the gantry rapidly revolves around the patient, a wide x-ray beam is sent through a section of the patient and detected on the opposite side. Based on the readings of the transmitted x-rays, a projection profile is generated. During one rotation, many projections are made for the same section of the patient and reconstructed into axial slices. Putting slices from many rotations together, a 3 dimensional CT image is obtained, showing the internal anatomy of the patient in the field of interest [40].

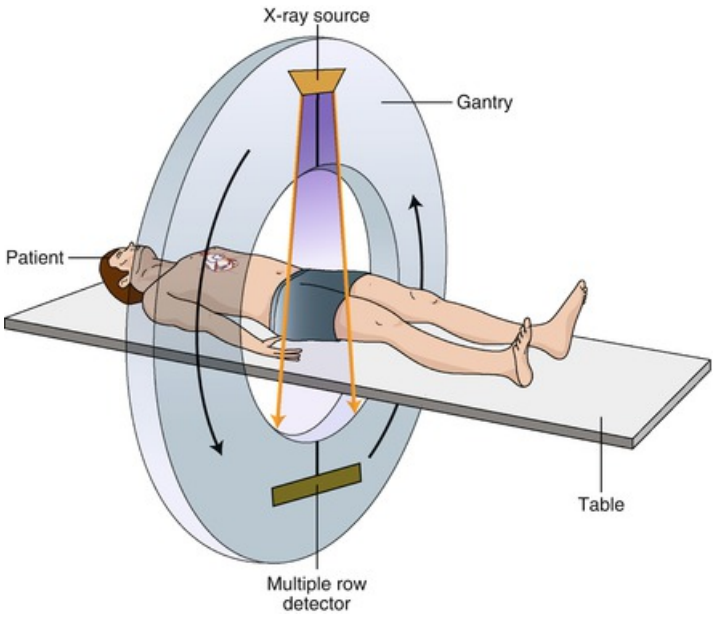

Figure 2.10: An illustration of a typical CT-scanner. Figure from [48].

A CBCT scanner performs the acquisition of the entire field of interest within one single rotation. Hence, a lower dose is deposited in the patient as compared to a standard CT scan. Due to more photon scattering, the image quality of a CBCT scan is substantially lower [15, 16].

The CT image is composed of a matrix of pixels. Each pixel is assigned a CT number that is associated with the attenuation of x-rays in the imaged tissue [40]. The effective linear attenuation for the same material may vary from scanner to scanner since the spectrum of x-rays generated in the machine and the energy-dependency of the detector response vary between scanners [41]. The format of a CT image is DICOM. One DICOM file contains the image itself and all metadata, including for instance the acquisition settings.

While the standard CT scanner uses one energy for imaging, a dual-energy CT (DECT) scanner uses two energies, enabling more accurate information about the materials that are imaged. Some tissues have the same attenuation of x-rays at one energy and different at another. Hence, the DECT can distinguish between tissues that are perceived as one tissue in a single-energy CT. Nevertheless, single-energy CT is still the standard imaging modality in proton therapy treatment planning, and the modality considered in this study [15, 41].

2.4.1 Hounsfield units

The CT number is given in Hounsfield unit (HU), defined as:

$$\mathrm{HU} = \left(\frac{\mu}{\mu_{\mathrm{w}}} - 1\right) \cdot 1000, \tag{2.10}$$

where μ and μ_w are the linear attenuation coefficients of the given material and of water, respectively. We have that for air, HU $= -1000$ since $\mu_{\text{air}} = 0$, and for water, HU $= 0$.

In a compound material, the linear attenuation coefficient (Eq. 2.2) can be expressed as

$$\mu(E) = \sum_i n_i \sigma_i(E) = \rho N_A \sum_i \frac{w_i}{A_i} \sigma_i(E), \tag{2.11}$$

where w_i is a weight fraction of the ith element in the mixture. The number of atoms per unit volume of an element has been expressed as $n = \frac{\rho N_A}{A}$ with ρ being the mass density, N_A the Avogadro constant and A the atomic mass. Using the parametrisation of σ (Eq. 2.4) the linear attenuation can be parametrised as

$$\mu(E) = \rho N_A \sum_i \frac{w_i}{A_i} [k_C(E) Z_i + k_R(E) Z_i^{2.86} + k_p(E) Z_i^{4.62}]. \tag{2.12}$$

The ratio between the effective linear attenuation coefficients of a compound material and the one of water can be expressed as

$$\frac{\mu}{\mu_w} = \frac{\rho}{\rho_w} \frac{\sum_i \frac{w_i}{A_i} (Z_i + k_1 Z_i^{2.86} + k_2 Z_i^{4.62})}{\frac{w_H}{A_H}(1 + k_1 + k_2) + \frac{w_O}{A_O}(8 + k_1 8^{2.86} + k_2 8^{4.62})}, \tag{2.13}$$

where k_1 and k_2 are fitting parameters that characterize the CT scanner's x-ray spectrum and energy-dependent detector response [41]. This ratio will be referred to as the reduced HU.

The electron density of an element can be expressed as

$$\rho_e = nZ = \rho N_A \frac{Z}{A}, \tag{2.14}$$

and in a mixture of different materials,

$$\rho_e = \rho N_A \sum_i w_i \frac{Z_i}{A_i}. \tag{2.15}$$

The relative electron density for a compound material can thus be written as

$$\hat{\rho_e} = \frac{\rho \sum_i w_i \frac{Z_i}{A_i}}{\rho_w (w_H \frac{Z_H}{A_H} + w_O \frac{Z_O}{A_O})}. \tag{2.16}$$

Combining this with equations 2.10 and 2.13 we have that the CT number depends linearly on the relative electron density $\hat{\rho_e}$ of the material, with proportionality constant σ [41].

2.5 HOUNSFIELD LOOK-UP TABLE

CT imaging is used in proton therapy planning to determine the proton range and dose distribution. Since photons and protons interact differently with tissue, a calibration curve is needed that establishes the relationship between the HU value of a given pixel

and the RSP [41]. There is no one-to-one physical relationship between the two. The HU value is based on photon interactions induced by the photoelectric effect or Compton scattering, whereas the proton interactions are described by the Bethe equation (Eq. 2.5) [49]. However, both have a linear dependency on the relative electron density $\hat{\rho}_e$, with proportionality constant σ for the CT number and L for RSP. The relationship between CT number and RSP can be approximated with a piecewise linear function called a Hounsfield look-up table (HLUT).

The easiest approach for generating a HLUT is by doing a CT scan of tissues with known elemental compositions, called tissue substitutes. When the composition is known, the RSP values for each tissue can be calculated theoretically by the Bethe-Bloch formula (Eq. 2.8) and the formula for relative electron densities (Eq. 2.16). The calculated RSP values can then be plotted against the HU values measured in the CT scan, and a HLUT function can be fitted to the plot. Then the HLUT can be used to calibrate from HU to RSP in new CT scans.

2.5.1 Stoichiometric calibration

To make the HLUT accurate for biological tissues, which are intrinsically different from tissue substitutes, the stoichiometric calibration method includes properties (density, elemental composition) of a large number of real human tissues [49, 50]. It is considered to be the most accurate method to establish the relationship between the HU numbers in single-energy CT scans and RSP [41].

An intrinsic part of the stoichiometric calibration is a characterisation of the CT scanner, accounting for the polychromatic x-ray spectrum and energy dependency of the detector. One approach is to determine k_1 and k_2 in equation 2.13 by scanning a phantom with tissue substitutes of known elemental composition, and minimizing the expression

$$\sum_j \left[\left(\frac{\mathrm{HU}}{1000} + 1 \right)_j - \left(\frac{\mu}{\mu_w}(k_1, k_2) \right)_j \right]^2, \tag{2.17}$$

where j runs over the tissue substitutes [41]. That is, minimising the squared sum of the differences between measured HU and synthetic, reduced HU (Eq. 2.13).

Knowing k_1 and k_2 for the scanner, synthetic HU values for any human tissue with known properties can be calculated by equations 2.10 and 2.13. With this one can obtain HU values for human tissues, as if they were scanned on the characterised scanner. The synthetic HU are used together with calculated RSP values for a large number of human tissues to make the HLUT.

2.5.2 Proton range uncertainties

This prediction of proton range from a CT scan is a large contributor to the overall uncertainty in proton therapy planning, and comes in addition to the uncertainties in treatment delivery mentioned earlier (Section 2.2.5). Comprehensive analysis by Yang

et al. [18] showed that the stoichiometric calibration has a combined uncertainty of $3-3.4\%$ in determining the proton RSP, and 3.5% uncertainty is commonly assumed in proton therapy planning [17].

First of all, there are uncertainties related to the CT scanner itself and the scanner calibration, which, according to Paganetti [17], is $\pm 0.5\%$, and even larger for lungs. The conversion from HU into RSP also comes with uncertainties, mainly due to the I-values (Eq. 2.7). In real biological tissues, the I-values will not be the same as in a solid state, but these are still being used in the clinical derivation. The uncertainty contribution from the I-value was estimated by Paganetti to be approximately 1.5% [17]. The multiple other steps in the conversion method may also contribute to error. As the RSP depends linearly $\hat{\rho_e}$ (Eq. 2.9), the proton range is highly sensitive to variations in electron density of the tissues along the beam path. The proton straggling effects is an additional source to error the proton range in tissue. According to Wohlfart and Richter, the overall range uncertainty for a HLUT-based approach is at least not overestimated with $3-3.5\%$ [49].

2.6 WATER EQUIVALENT PATH LENGTH

An useful application of the RSP values obtained from a CT scan is to calculate the WEPL of protons in the tissues. For a proton beam travelling through tissues with different stopping abilities, the WEPL scales the RSP values of all these tissues to the equivalent depth of water needed to produce the same stopping power. The WEPL can be obtained by integrating the RSPs along a straight line in a CT scan. This can be expressed as

$$\text{WEPL} = \sum_i x_i \text{RSP}_i, \tag{2.18}$$

where the subscript i represents the different pixels along the line and x is the chord length in mm, which is equal to the pixel size if the line is normal to the pixel edges and a more complicated function if the line is oblique. The WEPL is given in mm and describes in one single parameter the stopping of a proton beam in a patient, given a CT scan of the relevant body parts.

A clinically relevant application of WEPL is to monitor anatomical changes during the course of treatment by comparing the WEPL from time to time. A change in WEPL along the beam path indicates that the tissue densities have changed, which can affect the range of protons and the delivery of dose. An increase in WEPL along the proton beam path could lead to undershooting of the Bragg peak, whilst a decrease could lead to overshooting. If this situation persists for several treatment fractions, subsequently it could lead to under dosage of the target and/or too high doses to OARs [13]. By connecting the WEPL calculation to the CBCT scans taken before every fraction, it can become a very useful tool in adaptive proton therapy.

However, since the accuracy of the HU values is substantially lower in a CBCT as compared to a standard CT scan, evaluating the WEPL in CBCT scans would be less accurate. Scattering corrections would be needed, which makes the calculations more complicated [16]. This thesis will explore the feasibility of WEPL in adaptive therapy

using standard CT scans, which should be more accurate. The methods may be further developed to CBCT scans, which is where the true potential of WEPL in adaptive protocols could be utilized.

2.7 PREVIOUS RESEARCH CORRELATING WEPL AND DOSE DEGRADATION

In 2017, Gorgisyan et al. presented their study on applying WEPL analysis to explore the robustness of PBS-PT dose distributions for different beam angles. Data sets of 30 lung cancer (LA and non-LA NSCLC) patients previously treated with conventional radiotherapy were included. They evaluated DIBH CT scans acquired at planning and at the end of treatment, and analysed anatomical changes by calculating WEPL to the distal edge of the PTV. Optimised proton dose distributions were calculated and evaluated as V95, D98 and mean dose to CTV. Using linear models, correlation was found between the absolute changes in WEPL ($|\Delta\text{WEPL}|$) and the changes in V95 and D98 ($p < 0.01$). Tumor regression, tumor progression and weight loss were the main causes of larger ΔWEPL [13].

Later that year, the same research group evaluated the feasibility of breath hold in PBS-PT treatment of LA-NSCLC using the same WEPL analysis. They made IMPT plans using DIBH CT scans and the dose was recalculated onto repeated DIBH CTs acquired at the end of the treatment course. A significant correlation was found between the degradation in dose (CTV V95) and the percentage of voxels at the distal edge of the PTV with more than 3 mm WEPL undershoot ($p < 0.01$). They did not find correlation between degradation in dose and the other tested parameters, which were the mean WEPL change, the percentage of voxels with more than 3 mm WEPL overshoot, V95 of the WEPL over- or undershoot distributions, baseline shifts and changes in lung volume [11].

The method of evaluating WEPL differences for different beam angles was also applied in 2014 by Casares-Magaz et al. They presented a 4DCT-based method to assess WEPL variations induced by breathing motion. For each of the 3 patients included, 61 single-beam spot scanning proton plans were made on the maximum intensity profile (MIP) image set and transferred to the 10 phases of the 4DCT. An average dose to the CTV was calculated from the CTVs of the 10 phases. The WEPL values were extracted from the CT images and the mean ΔWEPL was calculated for all angle combinations and represented in 2D maps. The mean ΔWEPL was found to have a strong correlation with the reduction in CTV V95 with Pearson's correlation coefficients of 0.98, 0.92 and 0.96 for the three patients ($p < 0.01$) [12].

Bentefour et al. performed in 2014 a phantom study and found that CBCT could detect daily or cumulative variations of WEPL equal to or greater than 3 mm within the treatment volume. Considering WEPL variation over a specific path within the same CBCT slice, they could detect WEPL variations smaller than 1 mm. They reported that due to the limitations of CBCT to capture tissue density, the WEPL values calculated on CBCT deviated some from those from CT. But, since they could reproduce WEPL measurements on CBCTs from different days, it was effective inn detecting changes [16].

Veiga et al. presented in 2016 an adaptive proton therapy workflow in which they used a deformable image registration between the daily CBCT and the planning CT to create a virtual CT for every fraction. Then they compared the calculated WEPL in the virtual CT and the planning CT to find those patients with considerable anatomical changes. For those, repeated CT scans were triggered and the dosimetric effect was evaluated. The workflow based on CBCT provided similar clinical indicators as those using repeat CT [14].

3

MATERIALS AND METHODS

In this thesis, an algorithm for calculating WEPL in CT images was developed and evaluated as a decision tool in adaptive proton therapy of LA-NSCLC. The first step involved a calibration of the relevant CT scanner and generation of a HLUT, by implementing an algorithm presented by a former master student [51]. The implementation was done by the candidate and is explained in Section 3.1. Using the HLUT, the candidate developed an algorithm for calculating WEPL in CT images, which is explained in Section 3.2.

The WEPL was evaluated in CT scans of LA-NSCLC patients acquired at planning and during the treatment course. Differences in WEPL were associated with degradation of target dose in simulated proton therapy plans made on the same CT scans. The evaluation was performed by the candidate using dose parameters obtained in a previous project [1]. This is explained in Sections 3.3 - 3.5.

Calculation and evaluation of WEPL were performed by the candidate in Python v. 3.8.5. The Python codes are presented in Appendix D. The image processing program ImageJ (Wayne Rasband at the Research Services Branch, National Institute of Mental Health, Bethesda, Maryland, USA) was used to visualise CT scans and to verify the WEPL calculations. Statistical testing was performed in SPSS Statistics v. 26 (IBM Corp, Armonk, New York, USA).

3.1 STOICHIOMETRIC CALIBRATION

The workflow of the stoichiometric calibration was presented by Annette Høisæter in her master thesis in 2020 [51]. The Python code written by her was adapted by the candidate for calibration of the CT scanner applied in this project.

3.1.1 CT acquisition

All imaging for this project was performed on a Big Bore CT scanner (Philips Healthcare, Best, The Netherlands) belonging to the Department of Oncology and Medical Physics at Haukeland University Hospital (HUH). A scanning protocol designed for treatment planning of LA-NSCLC patients (See Section 3.3) was used. The acquisition settings are presented in Table 3.1.

Table 3.1: Settings for the CT acquisition. The exposure time, tube current and exposure are given for imaging of the calibration phantom.

Peak potential	120 kVp
Filter type	B
Scan option	Helix
Slice thickness	3 mm
Exposure time	1230 ms
Tube current	500 mA
Exposure	615 mAs

3.1.2 The Gammex phantom

The Gammex 467 Tissue Characterization Phantom (Figure 3.1) was used for the calibration. This phantom contains 16 cylindrical inserts of tissue substitutes. The elemental composition of the inserts is tabulated in Table B.1.

Figure 3.1: Gammex 467 Tissue Characterization Phantom.

The Gammex phantom was imaged on the CT scanner (Figure 3.2). The images were imported into Python in a DICOM format, where a package for reading DICOM files was used for measuring the HU values. In every slice, circular regions of interest (ROIs) were defined inside every insert avoiding the edges. Due to reduced amount of water in the water insert, this ROI was made smaller than the others. The HU for the tissue inserts were measured for five central slices and averaged (Table 3.2).

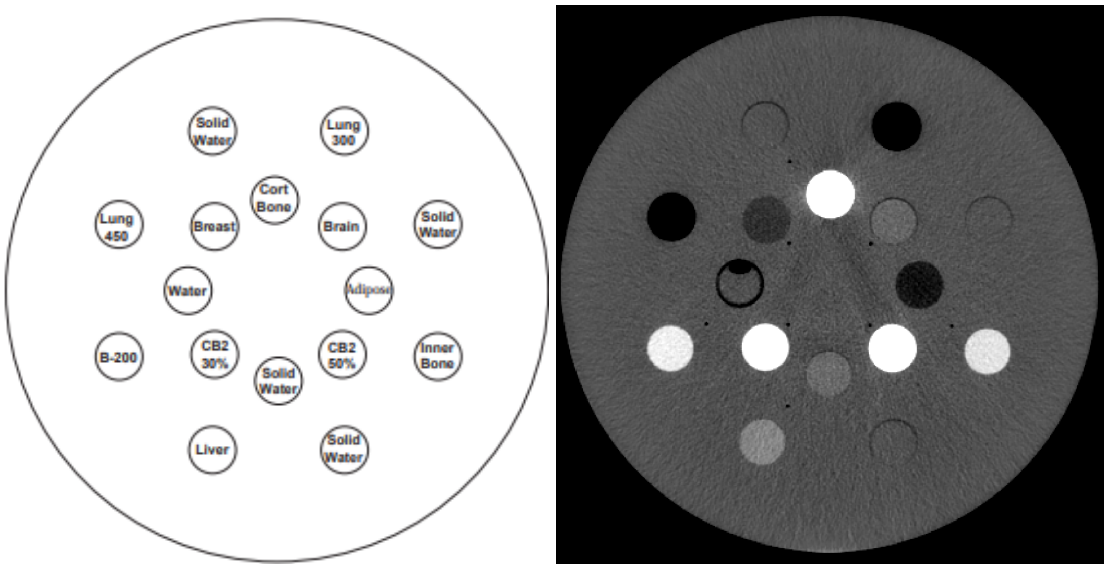

Figure 3.2: Left: Arrangement of tissue substitute inserts of the Gammex phantom. Right: CT image of the Gammex phantom.

Table 3.2: Measured HU for the 16 inserts of the Gammex 467 calibration phantom. The measurement was done for five central slices and averaged.

Insert	**Average HU**	**Insert**	**Average HU**
Lung 300	-709.6	Muscle	29.6
Lung 450	-531.9	Brain	23.8
Adipose	-90.9	Liver	67.4
Breast	-46.3	Inner bone	196.2
Water	-9.0	B-200	214.1
Solid Water 1	-2.4	CB2-30 %	431.7
Solid Water 2	-1.7	CB2-50 %	780.7
Solid Water 3	-5.3	Cortical bone	1186.5

3.1.3 Characterising the CT scanner

With the measured HU values for the Gammex inserts, and knowing their elemental composition, the scanner characteristic parameters k_1 and k_2 were found by minimising expression 2.17. That was done using a gradient descent minimization with boundaries $2 \cdot 10^{-4} < k_1 < 6 \cdot 10^{-3}$ and $3 \cdot 10^{-}6 < k_2 < 6 \cdot 10^{-4}$, inspired by Gomá et al. [41].

3.1.4 Synthetic HU and theoretical RSP for human tissues

Once the k-values characterising the applied CT scanner were determined, synthetic HU values were calculated using Equations 2.10 and 2.13 for 60 adult human tissues with

properties and elemental composition given in the ICRU report 46 [42]. Theoretical RSP values were calculated for each of the human tissues using Equation 2.8. The I-values were calculated using Equation 2.7 with I_i for tissue elements in a solid state listed in Table B.2. A mean excitation energy of water of $I_w = 78$ eV was used, and the RSP was calculated for proton kinetic energy of 100 MeV [41].

3.1.5 Making the HLUT

The synthetic HU values for the 60 human tissues were plotted against the calculated RSPs. The HLUT was generated through piecewise linear regression using the Python package PWLF. Initially, two break points were chosen, at HU $= 20$ and HU $= 40$, inspired by previous studies [41, 51].

For verification, the measured HU values for the inserts of the Gammex phantom were used as input in the piecewise linear function and the predicted RSP values were compared to theoretical RSP values calculated with Equation 2.8. The number of break points in the HLUT and their values were adjusted several times attempting to achieve the most accurate RSP prediction without overfitting.

The HLUT developed for the applied CT scanner could then be used to convert HU values to RSP values in any CT scan acquired at that scanner.

3.2 RSP PREDICTION AND WEPL CALCULATION

An algorithm for calculating WEPL in a CT scan was developed by the candidate. Opening a DICOM-formatted CT image in Python, pixel coordinates for two specific points in the image were defined. For every pixel along a straight line between the two points, HU values were measured and converted to RSP values using the HLUT. Finally, the WEPL of the straight line was calculated by an integration of the RSP values along the line (Eq. 2.18).

3.2.1 Verification of the WEPL calculation

The WEPL calculation was verified on a CT scan of a water phantom (Figure 3.3). Lines, representing proton fields, were defined from the center point to the edges of the image at angles 0° (field 1), 90° (field 2) and 210° (field 3). Along fields 2 and 3 the pixels included water only, while along field 1 some pixels included air. The WEPLs along the lines, calculated using the algorithm in Python, was compared to the physical length of the same lines, analysed in both Python and in ImageJ. The WEPL in water should be equal to the physical length in water. The WEPL along field 3 should verify that the integration was performed correctly also when the line crossed the pixel edges at oblique angles. The WEPL along field 1 was calculated in order to verify that the pixels with air were accounted for.

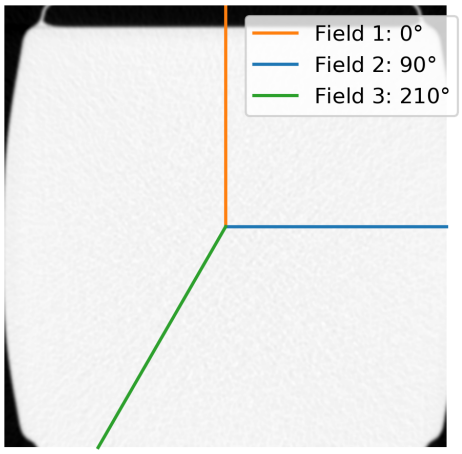

Figure 3.3: CT image of a water phantom. Lines, representing radiation field lines, from the center point to the edge of the CT image at angle 0°, 90° and 210 ° and were defined in Python.

The WEPL calculation was then applied to patient CT scans in order to evaluate the potential of using WEPL as a decision tool in adaptive proton therapy.

3.3 PATIENT MATERIAL

This study was a part of a research project that has been approved by the Regional Committee for Medical and Health Research Ethics of Western Norway (REK 2019/749). Invited to take part were LA-NSCLC patients treated with photon radiotherapy at HUH in 2019-2020. All patients gave informed consent before participation. Image material from 15 patients were included in the study of this thesis.

The patients were treated with IMRT to 60 or 66 Gy, given in daily fractions of 2 Gy. The standard treatment procedure was in free breathing, but three patients were treated in DIBH due to lung dose exceeding the constraints or large tumor motion blurring the 4DCT.

3.3.1 Images

As part of clinical practice, pCT scans were taken before treatment start and CBCT scans were taken before every treatment fraction. For the purpose of the research project, additional repeat CT (rCT) scans were taken in week 1 and week 3 of the treatment course. One out of the 15 patients missed the rCT of week 3. The pCTs and rCTs were taken both as 4DCT and DIBH CT (Figure 3.4). Target volumes and OARs were delineated in the pCTs as part of treatment planning, and in the rCTs due to the project. The same oncologist delineated the target volumes in all of the CT scans.

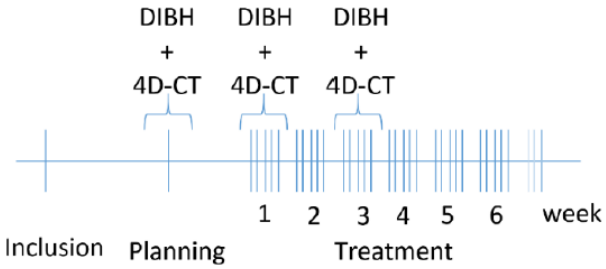

Figure 3.4: Timing for acquisition of CT scans for the research study. Also CBCT scans were taken at every treatment fraction (5 fractions/week).

This retrospective study evaluated the pCT and the two rCT scans of 15 LA-NSCLC patients. For the majority, the AIP of the 4DCTs were included, whilst for the three DIBH patients, the DIBH CTs were included.

Image registrations between the pCT and each of the rCTs (Figure 3.5) were performed by the candidate as a part of the specialisation project in 2021 [1]. Matching of the images' coordinate systems was based on the bony anatomy, and the images were moved in 3 directions (x, y, z) in a rigid image registration. This was done in Eclipse TPS (Varian Medical Systems, Palo Alto, CA, USA). The obtained image registrations were imported into the TPS RayStation v. 8B (RaySearch Laboratories, Stockholm, Sweden), where the proton therapy plans were made.

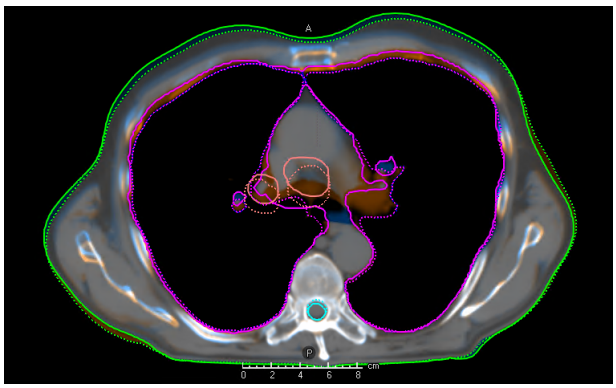

Figure 3.5: Rigid image registration between a pCT (blue shade) and a rCT (orange shade) of week 1. *Delineations:* coral: CTV, pink: lungs, cyan: spinal cord, green: body contour. The filled lines represent the delineations made on the pCT, while the dotted lines represent the rCT.

3.3.2 IMPT plans

A treatment planner from HUH with experience from proton therapy planning made IMPT plans retrospectively for these patients using RayStation. The original pCT scans including delineations of target volumes and OARs from the planning of the actual treatment were used. For patients treated in DIBH, also IMPT plans were made on the DIBH CT scans by the candidate's supervisor, K. Fjellanger. The plans consisted of 2 or 3 radiation fields and were made 3D robust accounting for setup and range uncer-

tainties. The robustness settings were 5 mm in each direction (x, y, z) with a 3.5% range uncertainty.

As a part of the specialisation project [1], the candidate recalculated the IMPT plans on the rCTs of week 1 and week 3, showing the dose distribution at these points in the treatment course (Figure 3.6). The recalculation was done in RayStation after importing the rigid image registrations made in Eclipse. Since the target volumes and OARs had been delineated again in the rCTs, after possible anatomical changes, the dose to each volume could be found. The volume of the CTV receiving at least 95% of the prescribed dose (CTV V95) was extracted as a measure of target coverage, which is highly important for the quality of the treatment.

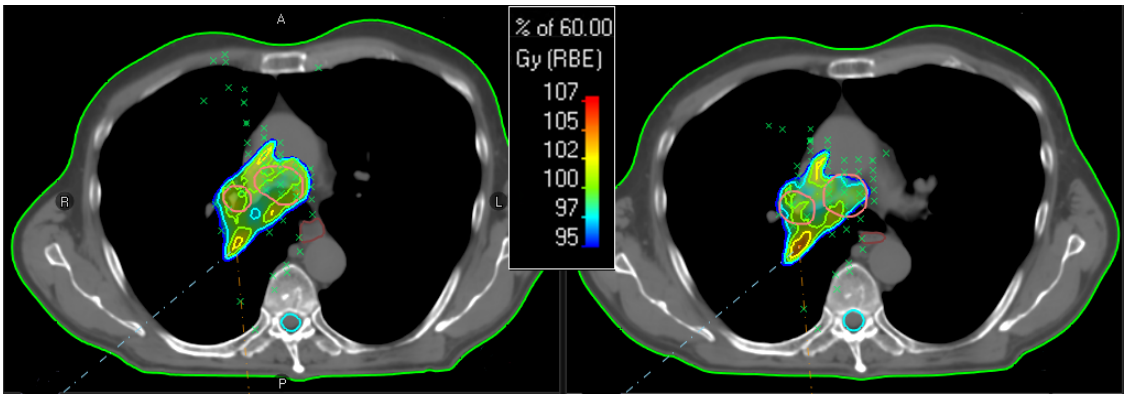

Figure 3.6: Dose distribution of an original IMPT plan (left) and of the recalculation of the plan on the rCT of week 1 (right). The blue and orange dotted lines show the center lines of the fields, and the green crosses show the positions of Bragg peaks. *Delineations*: coral: CTV, cyan: spinal cord, green: body. The color scale shows the dose from 95% to 107% of the prescribed dose, which was 60 Gy(RBE) in this plan.

3.3.3 Anatomical changes

During the radiotherapy treatment, the RTTs registered anatomical changes that they observed on the daily CBCT scans of the patients. They rated the observed changes according to a traffic light protocol, inspired by the one developed by Kwint et al. [52]. The changes addressed in the protocol were atelactasis, pleural effusion, infiltrative changes, baseline shift, tumor regression and tumor progression. Green colors were assigned to patients with no or little anatomical changes as compared to the pCT, meaning that the treatment should continue as planned. Yellow indicated that there were anatomical changes, but small enough to assume target coverage with the planned treatment. Orange color indicated that there were significant anatomical changes and that the dosimetric impact should be evaluated by a medical physicist or oncologist before the next treatment fraction. Red color represented large anatomical changes and the need for replanning before continuing the treatment.

Based on these registrations and on visual inspection of the image registrations between the pCTs and the rCTs, which both had delineated structures, the candidate evaluated the anatomical changes during the treatment course for every patient. Registered ana-

tomical changes with traffic light colors orange and red were included, while registered changes with yellow color were evaluated based on the image registrations with focus on the impact on the WEPL and the IMPT dose distribution. Changes in lung volume, due to different breathing patterns, and in body contour, due to patient setup for instance, where not specifically addressed in the traffic light protocol. These changes were evaluated by the candidate based on the image registrations only. This evaluation was indefinite and not very reliable, but should give an indicator on the feasibility of the WEPL calculations in detecting anatomical changes.

3.4 EVALUATING WEPL IN PATIENT CT SCANS

The patient CT scans were exported in DICOM format from Eclipse, along with the 3 translation values describing the image registration between the pCT and rCTs. DICOM files containing the delineated structures on each CT scan were also exported. The files were imported into Python, where the WEPL calculation was performed.

3.4.1 Locating the target structure

From the structure DICOM file corresponding to the pCT, the pixel coordinates of all points at the surface of the delineated CTV were extracted. These coordinates were used to locate the CTV structure in the CT scans and exclude the slices in which the CTV structure was not present. Slices with two (or more) separated CTV structures, as can be seen in figure 3.6, were included once for each structure. A Python script for doing this automatically was written by the candidate's supervisor, H. Pettersen. The following work was done by the candidate.

For the rCT scans, the translation values from the image registration with the pCT (x, y, z) were added to correctly locate the structure. Note that the structure delineated in the pCT was used to locate the target volume also in the rCTs, instead of using the delineations made on the rCTs. There are two reasons for that. Firstly, this study involved an analysis of the differences in WEPL between the pCT and rCTs. Hence, keeping the same reference points was considered to be the best solution. Secondly, if the WEPL analysis is going to be used as part of an adaptive protocol in the clinic, the RTTs will have access to the delineated structures made at planning throughout all treatment fractions, whilst they will probably not have rCTs and re-delinations.

3.4.2 WEPL to the distal edge of CTV

From the IMPT plans in RayStation, the beam angles of each radiation field (2 or 3 fields) were extracted. In every image slice containing a part of the CTV structure, the distance along the beam path from each point of the CTV structure to the edge of the image was calculated. The half of the points with the largest distance were extracted to represent the distal edge of the CTV relative to each field angle (Figure 3.7). The distal edge of

CTV was of interest for the WEPL calculation in order to detect anatomical changes both within and proximal to the target [11].

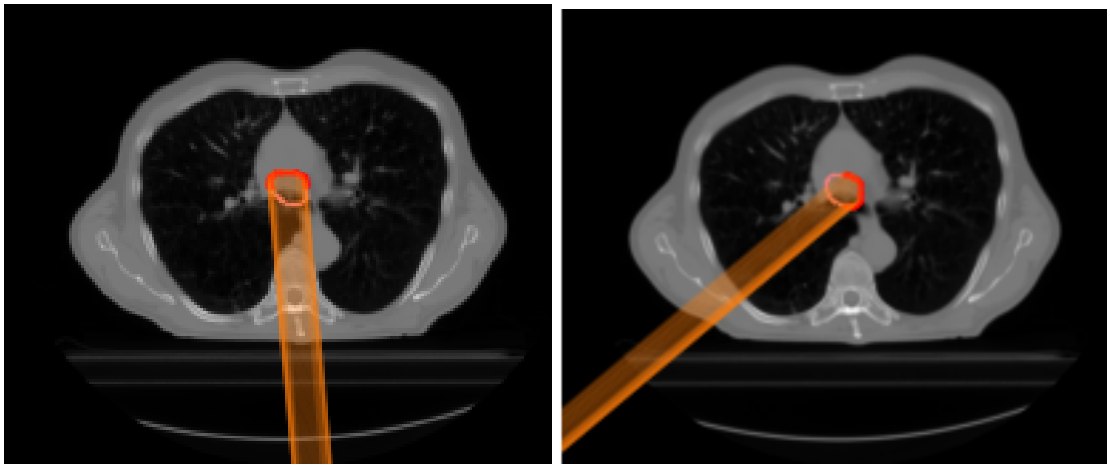

Figure 3.7: A CT image of one of the patients with the CTV delineated in coral and the distal edge of CTV in red. The WEPL was calculated along several individual paths (colored orange) from the outer edge of the image to every point on the distal edge of the CTV relative to the radiation field angle. Here shown for two different field angles.

The WEPL was calculated as described in Section 3.2 between the pixels of all points at the distal CTV edge and the corresponding points at the outer edge of the image at the given beam angles. In Figure 3.7 the orange lines represent the paths in the image along which the WEPL was calculated. There is one line for every point at the distal edge of CTV. Hence, where the CTV structure curves, there might be overlapping paths, seen as more opaque lines in the figure. The calculations resulted in large tables containing WEPL values to every point at the distal edge of CTV for every field angle and for every image slice.

3.4.3 WEPL changes

WEPL calculations were performed on the pCT and on the rCTs of week 1 and week 3. As the CTV structure delineated at planning was used in all three CTs, changes in WEPL could be analysed point by point. The WEPL change was calculated as

$$\Delta\text{WEPL} = \text{WEPL(rCT)} - \text{WEPL(pCT)}. \tag{3.1}$$

A decrease in WEPL from the pCT to the rCT ($\Delta\text{WEPL} < 0$) corresponded to range overshoot and an increase ($\Delta\text{WEPL} > 0$) corresponded to range undershoot.

The analysis of ΔWEPL was inspired by the method in the studies by Gorgisyan et al. [11, 13]. The mean $|\Delta\text{WEPL}|$ was calculated for every patient rCT (from the pCT) by averaging the absolute ΔWEPL values over all points at the distal CTV edge for the field angles involved. Absolute values were used as any change in WEPL was of interest. The 95th percentile of the $|\Delta\text{WEPL}|$ per field angle was also extracted for each patient rCT and averaged over the field angles. This was considered to be an accurate measure of

the degree of WEPL changes without averaging over the numerous points at the distal edge of CTV.

As another measure of the ΔWEPL from the pCT to the rCT, the percentage of points at the distal edge of CTV with more than 3 mm and more than 10 mm change in WEPL were analysed. The choice of 3 mm as a threshold was inspired by Gorgisyan et al. [11], while the 10 mm threshold was chosen to better distinguish between small changes and large changes in our data. In addition to consider the percentage of points with absolute WEPL changes above the given thresholds, the percentage of points with overshoot and undershoot were analysed separately. As a CT scan with a large number of overshooting points typically had a low number of undershooting points, every rCT was classified as an overshooting case or an undershooting case based on the majority of points.

3.5 STATISTICAL EVALUATION

For evaluating the feasibility of WEPL in adaptive proton therapy, the WEPL changes from the pCTs to the rCTs were associated with the dose distribution in the recalculated IMPT plans. The CTV V95 was used as a measure for target coverage, and relative changes (ΔV95) from the original IMPT plans to the recalculation on the rCT scans were evaluated. Assuming $\Delta V95 \leq 0\%$ for all, $\Delta V95 \geq -1\%$ was deemed acceptable. Plans with more than 1% degradation ($\Delta V95 < -1\%$) were classified as failing plans.

For the hypothesis 2, the Spearman's rank-order correlation coefficient test in SPSS was used. The correlation with ΔV95 was assessed for the mean $|\Delta WEPL|$, the 95th percentile of $|\Delta WEPL|$, the percentage of points with $|\Delta WEPL| > 10$ mm and > 3 mm, and the percentage of overshooting- and undershooting points above these thresholds. The Spearman's correlation coefficient is referred to as r_S, and the significance level is $p < 0.05$.

The Mann-Whitney U test in SPSS was used to test hypothesis 3. The comparison between the group of failing plans and the group of accepted plans was done for the mean $|\Delta WEPL|$, the 95th percentile of $|\Delta WEPL|$ and the percentage of points with $|\Delta WEPL| > 10$ mm and 3 mm, with significance level $p < 0.05$. This test was implemented for the rCTs of week 1 and week 3 separately, due to the requirement of independent samples.

4

RESULTS

4.1 STOICHIOMETRIC CALIBRATION

The scanner characteristic k-values were calculated to $k_1 = 2.000 \cdot 10^{-4}$ and $k_2 = 2.303 \cdot 10^{-5}$. With these, synthetic HU and RSP values of the 60 adult human tissues were successfully calculated and are presented in Table B.3. These values were used to generate the piecewise linear HLUT, using two break points at HU $= 20$ and HU $= 40$. The resulting HLUT, which is specially designed for the CT scanner, can be seen in Figure 4.1. The equations describing the HU-to-RSP conversion were given as

$$\text{RSP} = \begin{cases} 0.000976438425349501 \cdot \text{HU} + 1.01685572002769, & \text{if HU} \leq 20 \\ 0.00102118905637142 \cdot \text{HU} + 1.01596070740725, & \text{if } 20 < \text{HU} \leq 40 \\ 0.000694191199870186 \cdot \text{HU} + 1.0290406216673, & \text{if HU} > 40. \end{cases} \tag{4.1}$$

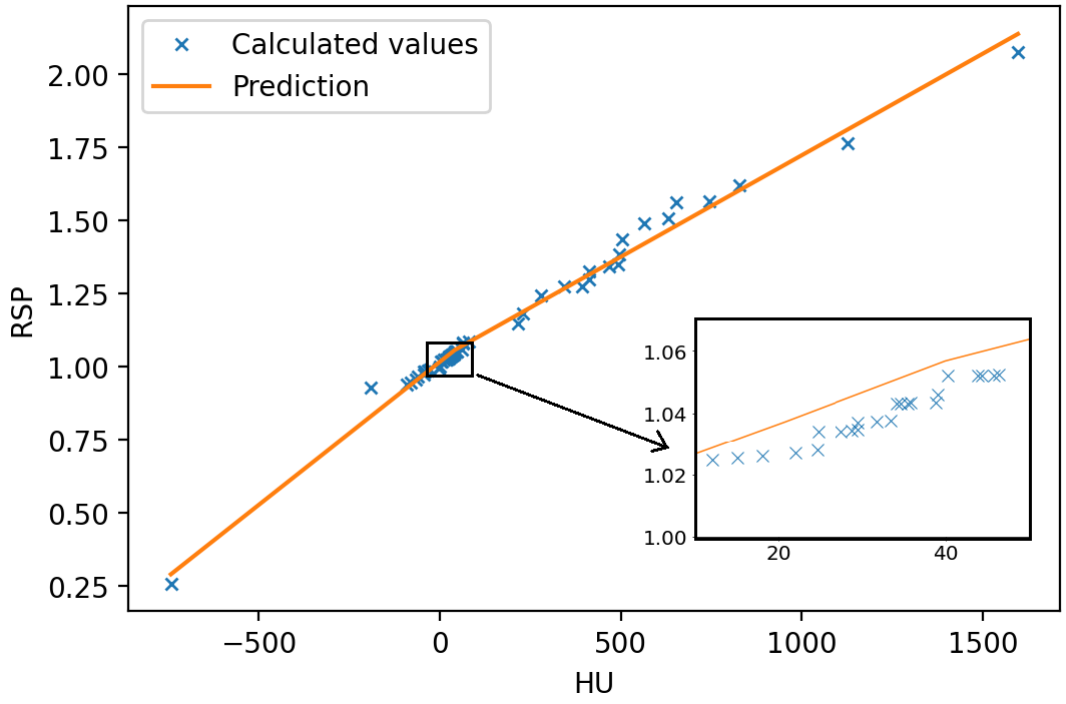

Figure 4.1: Hounsfield look-up table (HLUT) for the CT scanner used in this study. The calibration of the HLUT was based on 60 ICRU adult human tissues [42].

4.1.1 Accuracy of RSP prediction

For the 16 inserts of the Gammex phantom, RSP values were predicted experimentally using the HLUT and calculated theoretically using Equation 2.8. Table 4.1 shows the results. With the calculated RSP values as references, the HLUT was able to predict the RSP of the Gammex inserts with a mean absolute error of 0.045 ± 0.043. The relative errors per insert are presented in Figure 4.2, and the mean relative error (MRE) in absolute values was 4.6%.

Table 4.1: Reference RSP (RSP ref) calculated with equation 2.8 and predicted RSP (RSP exp) using the HLUT for the 16 inserts of the Gammex 467 calibration phantom.

Insert	**RSP ref**	**RSP exp**	**Insert**	**RSP ref**	**RSP exp**
Lung 300	0.283	0.324	Muscle	1.023	1.046
Lung 450	0.458	0.497	Brain	1.052	1.040
Adipose	0.930	0.928	Liver	1.067	1.076
Breast	0.942	0.972	Inner bone	1.085	1.165
Water	1.001	1.008	B-200	1.101	1.178
Solid Water 1	0.990	1.014	CB2-30 %	1.279	1.329
Solid Water 2	0.990	1.015	CB2-50 %	1.465	1.571
Solid Water 3	0.990	1.012	Cortical bone	1.685	1.853

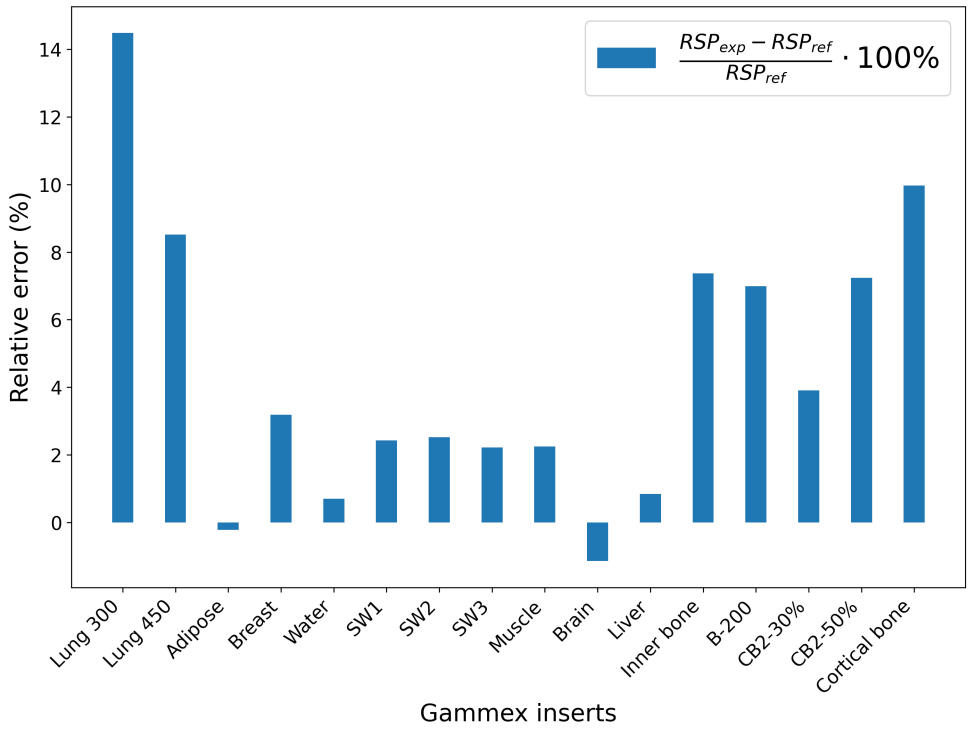

Figure 4.2: Relative error of the HLUT-predicted RSP values of the 16 Gammex inserts.

4.2 VERIFICATION OF THE WEPL CALCULATION

The verification of the WEPL calculation on a CT scan of a water phantom showed that the WEPL of a line in water was almost equal to the physical length, while for a line including air, the WEPL was shorter (Table 4.2). The physical lengths for the lines were equal when measured in ImageJ and calculated in Python. Figure 4.3 shows the RSP values as functions of WEPL for fields 1 and 2. The WEPL was approximately 0 for the pixels with air in field 1.

Table 4.2: Along the three field lines defined in Figure 3.3 (1: 0°, 2: 90°, 3: 210°), the physical length was measured in ImageJ and calculated in Python. The WEPL for each line was calculated in Python.

Field	ImageJ: Length (mm)	Python: Length (mm)	WEPL (mm)
1 (air and water)	100.0	100.0	92.4
2 (water)	99.6	99.6	101.4
3 (water, oblique)	115.2	115.2	117.0

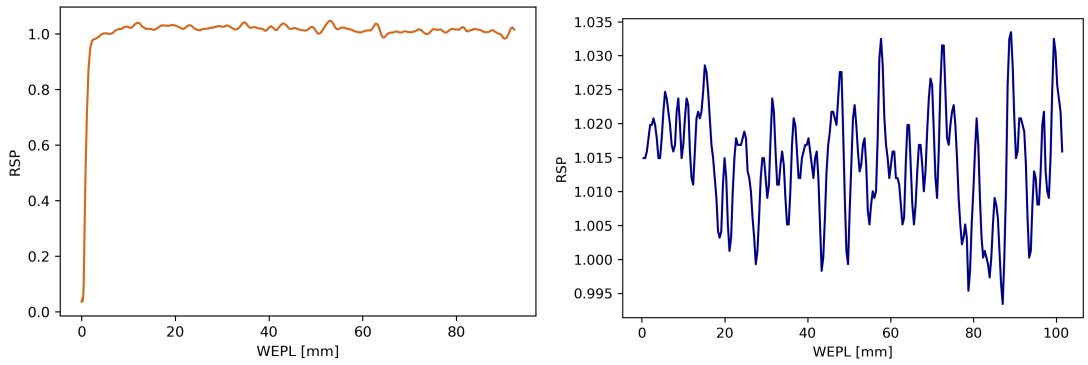

(a) Field 1 (air and water)

(b) Field 2 (water)

Figure 4.3: The RSP as a function of the WEPL along the field 1 and field 2 in the CT scan of the water phantom (Figure 3.3). The graph of field 1 shows that in points with air, the WEPL is close to 0, while in water, the WEPL is close to 1, as also shown for field 2.

4.3 WEPL CHANGES IN PATIENT CT SCANS

The WEPL was successfully calculated along the proton beam angles to all points at the distal edge of the CTV in every patient CT scan. Analysing the WEPL changes (ΔWEPL) from the pCT to the rCTs for every point resulted in a large amount of data for each patient rCT. The highest number of ΔWEPL values obtained for one rCT was 8930 (Patient 4 week 3), while the lowest number was 1935 (Patient 2 week 3). Figure 4.4 shows a boxplot of the ΔWEPL for every patient rCT.

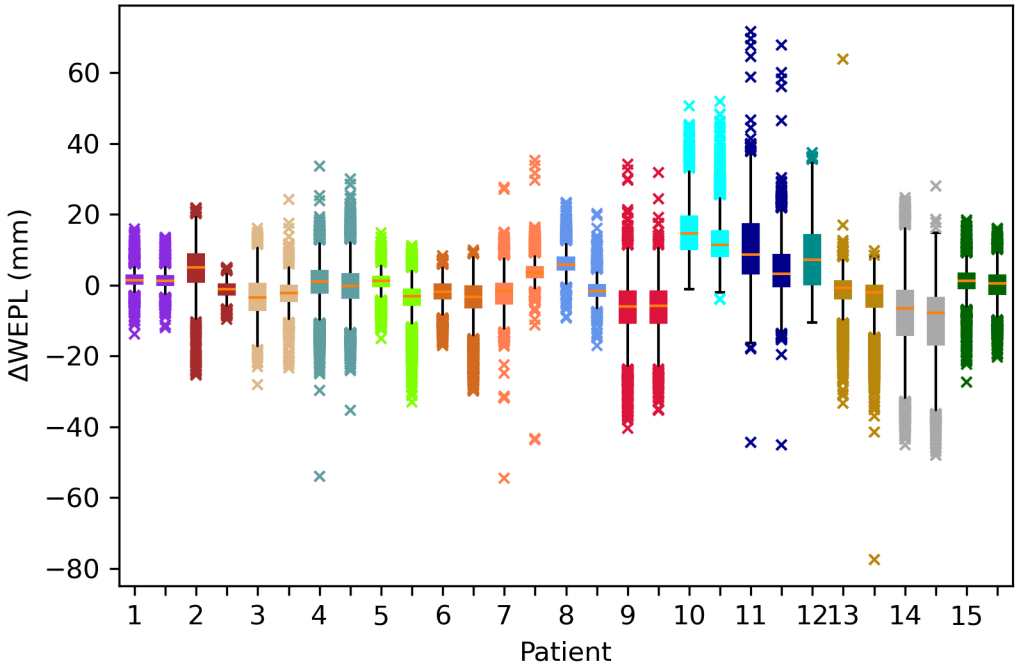

Figure 4.4: The WEPL changes from every pCT to the corresponding rCTs in every pixel of the distal edge of CTV for each field angle. For every patient, the box to the left represents changes to the rCT of week 1 and the box to the right represents changes to the rCT of week 3. For patient 12 the rCT of week 3 was missing. The boxes extend from the first quartile (Q1) to the third quartile (Q3) of the data, with an orange line at the median. The whiskers extend from the box by 1.5 times the inter-quartile range (IQR = Q3-Q1), and outliers are shown as small crosses. Due to a large numbers of outliers, the crosses tend to overlap.

As an example, Figure 4.5 shows the distribution of WEPL values in the pCT and the ΔWEPL for the rCTs of week 1 and week 3 for patient 10. For this patient, the majority of points had larger WEPL in the rCTs as compared to the pCT, meaning that $\Delta\text{WEPL} > 0$. The mean ΔWEPL for this patient was 15.3 mm in week 1 and 12.8 mm in week 3. The median ΔWEPL was 14.6 mm in week 1 and 11.3 mm in week 3. Similar histograms presenting the values of $|\Delta\text{WEPL}|$ for all patients are shown in Appendix C.

Figure 4.6 shows the mean $|\Delta\text{WEPL}|$ for every patient rCT, together with the standard deviation. The median of the mean $|\Delta\text{WEPL}|$ for all patient rCTs was 5.4 mm in week 1 and 4.5 mm in week 3.

Figure 4.7 shows the percentage of points at the distal edge of CTV with > 10 mm change in WEPL for every patient rCT. The median percentage of points with $|\Delta\text{WEPL}| > 10$ mm for all patients was 13.1% in week 1 and 10.0% in week 3.

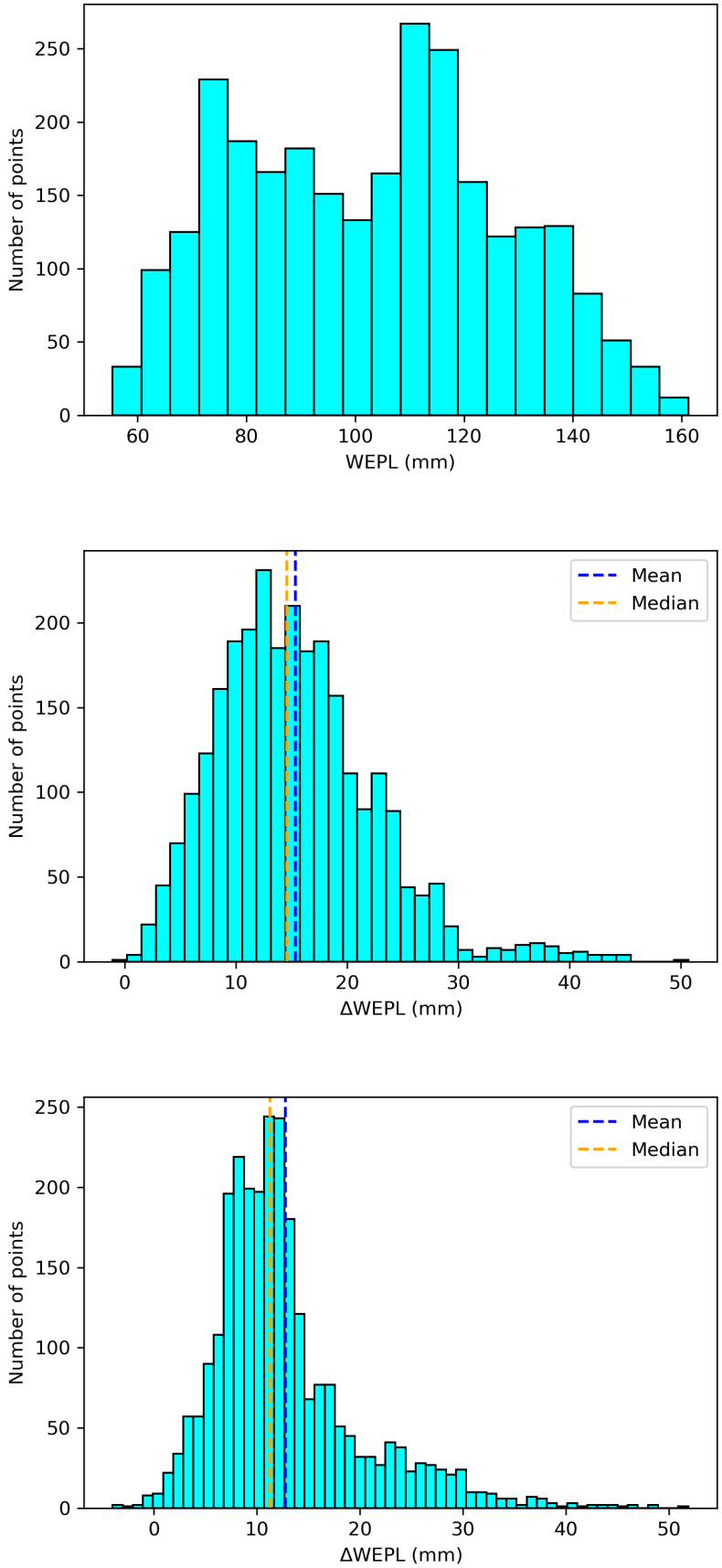

Figure 4.5: The distribution of WEPL values in the pCT (upper figure), and the WEPL changes from the pCT to the rCT of week 1 (middle figure) and to the rCT of week 3 (lower figure) for patient 10. A total of 2703 points were counted for each CT.

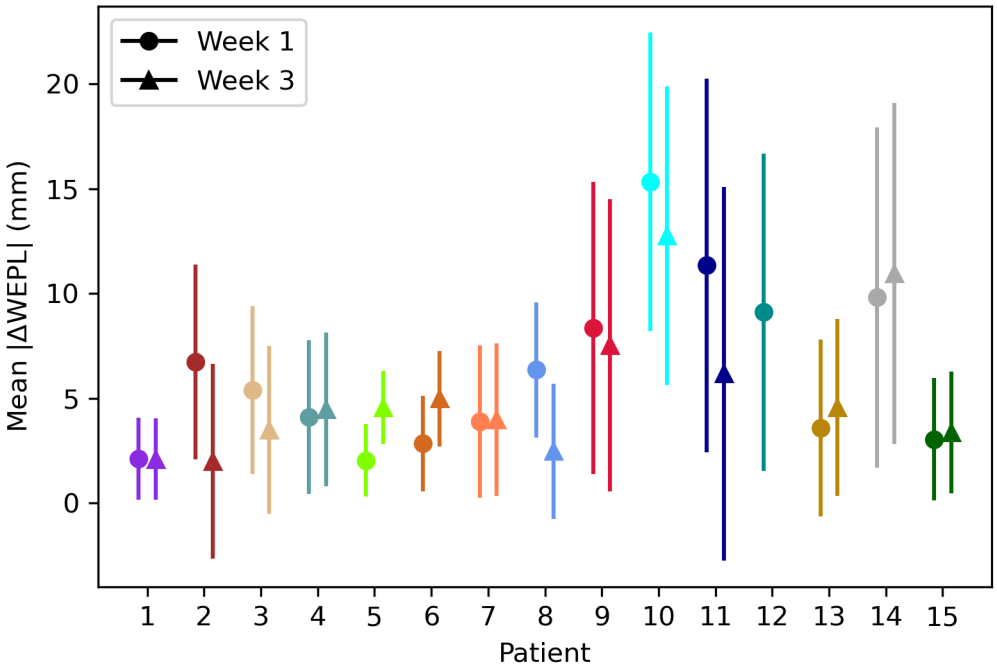

Figure 4.6: Mean and standard deviation of the absolute WEPL changes from the pCT to the rCTs of week 1 and week 3 for each patient.

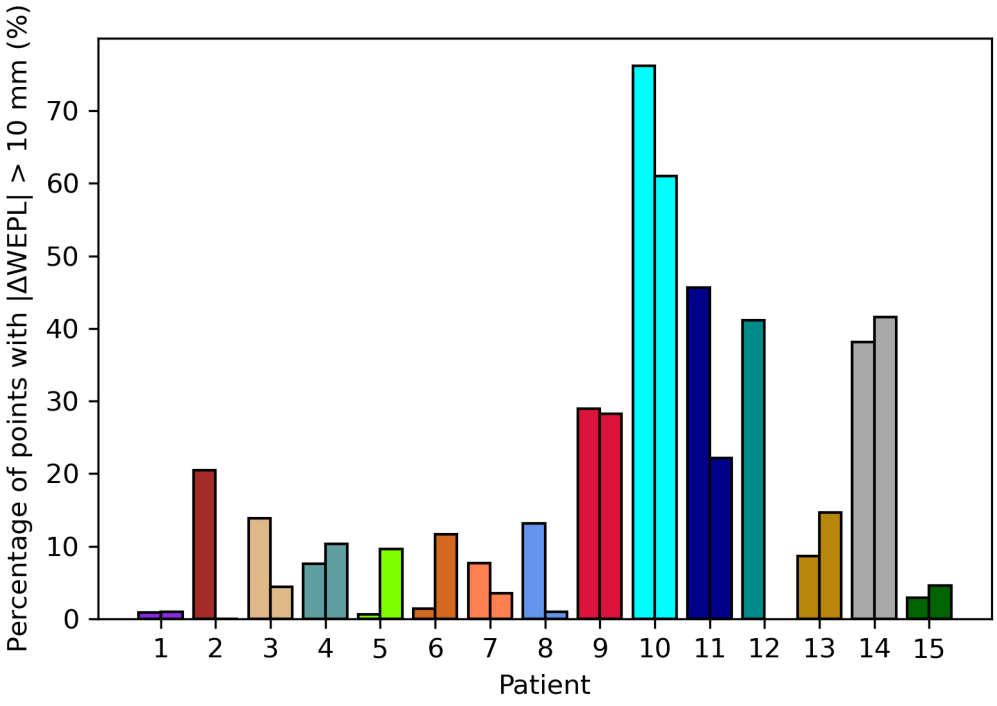

Figure 4.7: The fraction of points at the distal edge of the CTV with more than 10 mm change in WEPL from the pCT to the rCT. For every patient, the bar to the left represents the rCT of week 1 and the bar to the right represents the rCT of week 3.

4.3.1 Correlation with anatomical changes

Tables 4.3 and 4.4 list the observed anatomical changes for every patient in week 1 and week 3, respectively, based on reports from the RTTs in the clinic and the candidate's visual inspection of the rCTs. The patients are sorted from the one with the largest to the one with the smallest percentage of points at the distal edge of CTV with $|\Delta\text{WEPL}| > 10$ mm.

Table 4.3: Observed anatomical changes and the percentage of points at the distal CTV edge with $|\Delta\text{WEPL}| > 10$ mm for all patients in week 1.

Patient	**Percentage of points with $\lvert\Delta$WEPL$\rvert$ > 10 mm**	**Anatomical changes**
10	76.2%	Baseline shift, smaller lung volume, changed body contour (more tissue in 1/2 fields)
11	45.7%	Baseline shift, smaller lung volume
12	41.1%	Changed body contour (more tissue in 2/2 fields)
14	38.1%	Tumor regression, larger lung volume, changed body contour (more tissue in 1/3 fields, less in 2/3)
9	29.0%	Baseline shift, changed body contour (less tissue in 1/2 fields)
2	20.5%	Larger lung volume
3	13.8%	Baseline shift, changed body contour (more tissue in 2/2 fields)
8	13.1%	Baseline shift, changed body contour (more tissue in 1/2 fields)
13	8.6%	Little changes
7	7.7%	Little changes
4	7.6%	Baseline shift, changed body contour (more tissue in 1/3 fields)
15	2.9%	Little changes
6	1.4%	Little changes
1	0.9%	Little changes
5	0.6%	Little changes

Table 4.4: Observed anatomical changes and the percentage of points at the distal CTV edge with $|\Delta\text{WEPL}| > 10$ mm for all patients in week 3.

Patient	**Percentage of points with $\lvert\Delta$WEPL$\rvert$ > 10 mm**	**Anatomical changes**
10	61.0%	Baseline shift, smaller lung volume, changes body contour (more tissue in 1/2 fields)
14	41.6%	Tumor regression, larger lung volume, changed body contour (less tissue in 3/3 fields)
9	28.3%	Tumor regression, changed body contour (less tissue in 1/2 fields)
11	22.2%	Baseline shift, smaller lung volume
13	14.6%	Tumor regression
6	11.6%	Baseline shift, larger lung volume,
4	10.4%	Tumor regression, changed body contour (more tissue in 1/3 fields)
5	9.6%	Little changes
15	4.5%	Little changes
3	4.4%	Baseline shift
7	3.57%	Baseline shift
1	1.0%	Changed body contour (more tissue in 1/3 fields)
8	1.0%	Baseline shift
2	0 %	Little changes

4.4 DOSE DEGRADATION

All original IMPT plans had CTV V95 = 100%, except one that had CTV V95 = 91.2% due to an overlap of the target volume with the spinal cord. The relative change in CTV V95 (ΔV95) from planning to week 1 and week 3 for each plan is shown in Figure 4.8. The median ΔV95 was −0.15% (range −3.97% - 0%) in week 1 and −0.21% (range −5.53% - 0%) in week 3.

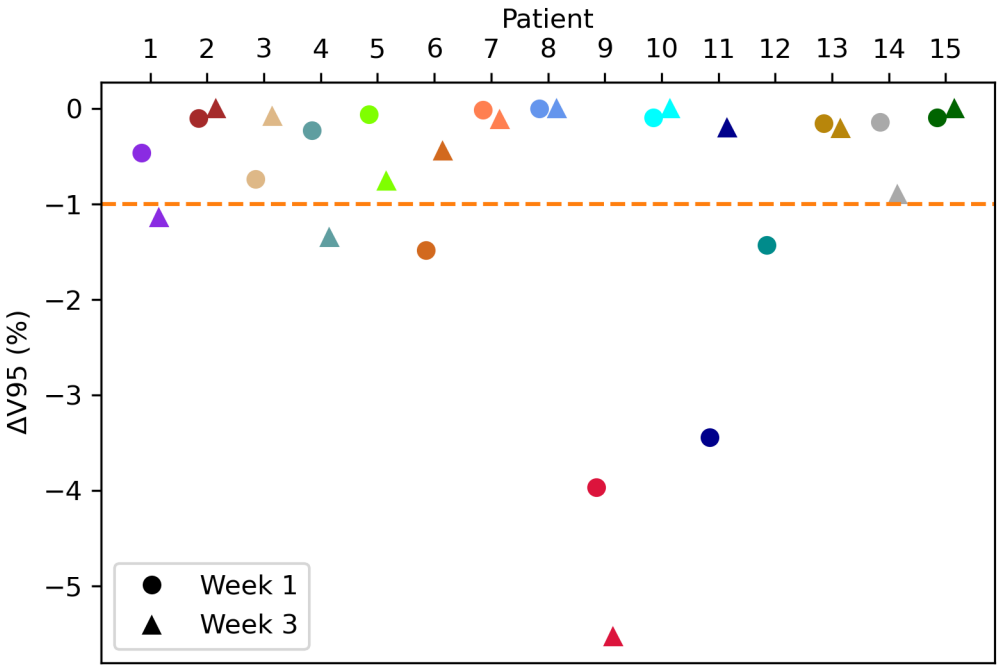

Figure 4.8: Relative change in CTV V95 from the original IMPT plan to the recalculations on the rCTs of week 1 and week 3 for every patient. The orange dotted line indicates a 1% degradation in CTV V95.

With ΔV95 ≥ −1% as acceptance criterion, 4/15 plans failed in week 1 and 3/14 plans failed in week 3. One plan (patient 9) failed in both weeks. Figure 4.9 shows the distribution of ΔV95 values for the group of failing plans and the group of accepted plans.

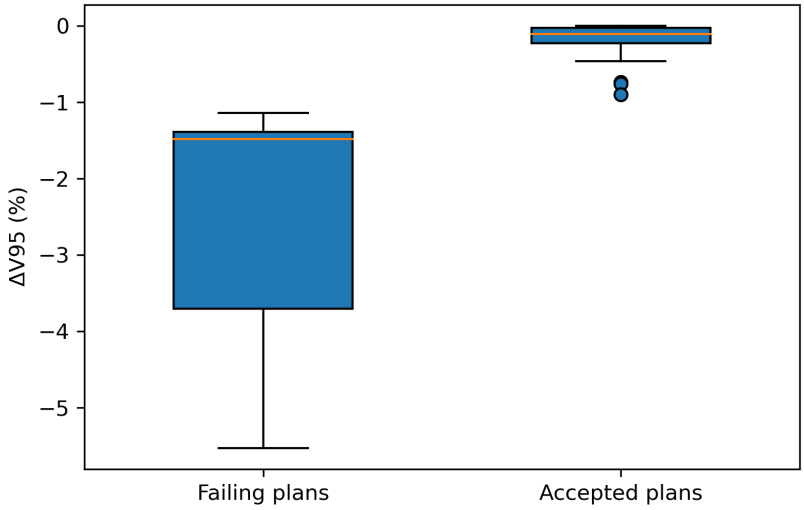

Figure 4.9: Changes in CTV V95 for the group of failing plans ($\Delta V95 < -1\%$) and the group of accepted plans ($\Delta V95 \geq -1\%$) in week 1 and in week 3. The boxes extend from the first quartile (Q1) to the third quartile (Q3) of the data, with an orange line at the median. The whiskers extend from the box by 1.5 times the inter-quartile range (IQR = Q3-Q1), and outliers are shown as blue dots.

4.5 CORRELATING WEPL CHANGES TO DOSE DEGRADATION

The ΔWEPL at the distal edge of CTV was quantified using the mean $|\Delta WEPL|$, the 95th percentile of $|\Delta WEPL|$, the percentage of points with $|\Delta WEPL| > 10$ mm and > 3 mm and the percentage of points with undershooting or overshooting above these thresholds.

4.5.1 Mean WEPL changes

Figure 4.10 shows the association between the mean $|\Delta WEPL|$ for each patient rCT and ΔV95 in the recalculated IMPT plan on the same rCT. There was no statistically significant correlation between mean $|\Delta WEPL|$ and ΔV95, according to the Spearman's correlation coefficient ($r_S = -0.276$, $p = 0.148$).

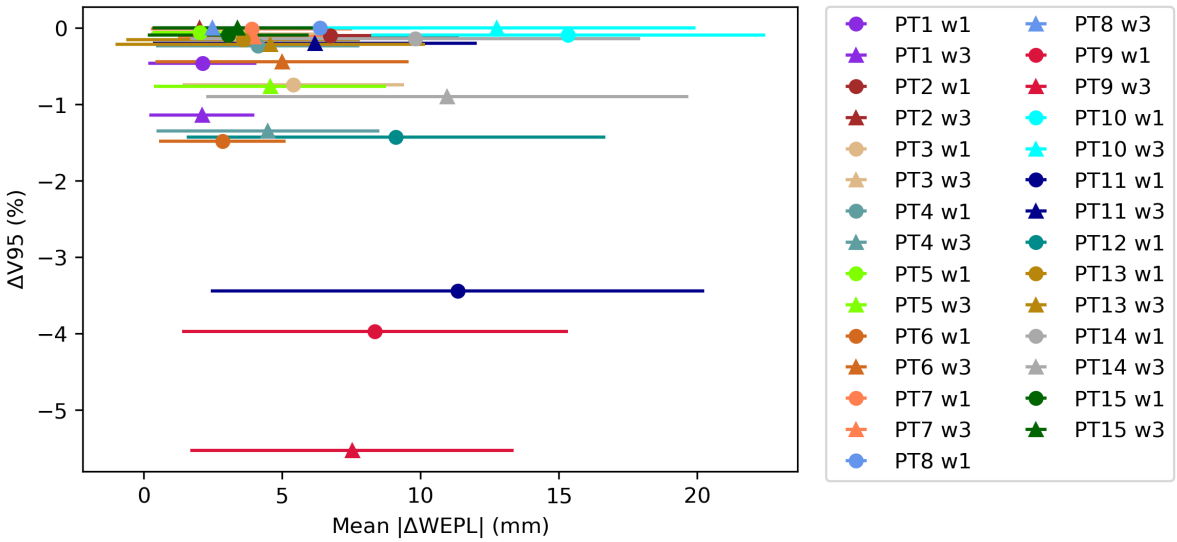

Figure 4.10: The mean and standard deviation of the absolute WEPL changes and the relative change in CTV V95 for every patient rCT. *Abbreviation:* PT = patient, w = week.

Figure 4.11 shows the distribution of the mean $|\Delta\text{WEPL}|$ for all patient rCTs in the group of failing plans and the group of accepted plans. The Mann-Whitney U test concluded that there was not a significant difference in mean $|\Delta\text{WEPL}|$ between the two groups, neither in week 1 ($p = 0.343$) nor in week 3 ($p = 0.885$).

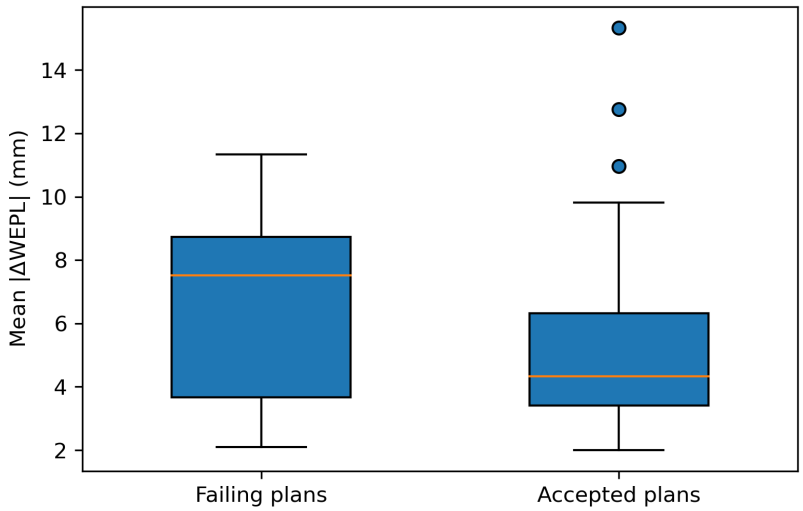

Figure 4.11: Mean absolute WEPL changes for all patient rCTs (week 1 and week 3) in the group of failing plans ($\Delta\text{V95} < -1\%$) and the group of accepted plans ($\Delta\text{V95} \geq -1\%$).

4.5.2 95th percentile of WEPL changes

The 95th percentile of the |ΔWEPL| was calculated for every patient rCT and plotted towards the dose degradation in Figure 4.12. There was not a statistically significant correlation ($r_s = -0.354, p = 0.059$). Comparing this parameter between the groups of failing plans and accepted plans showed no significant difference, neither in week 1 ($p = 0.280$) nor in week 3 ($p = 885$).

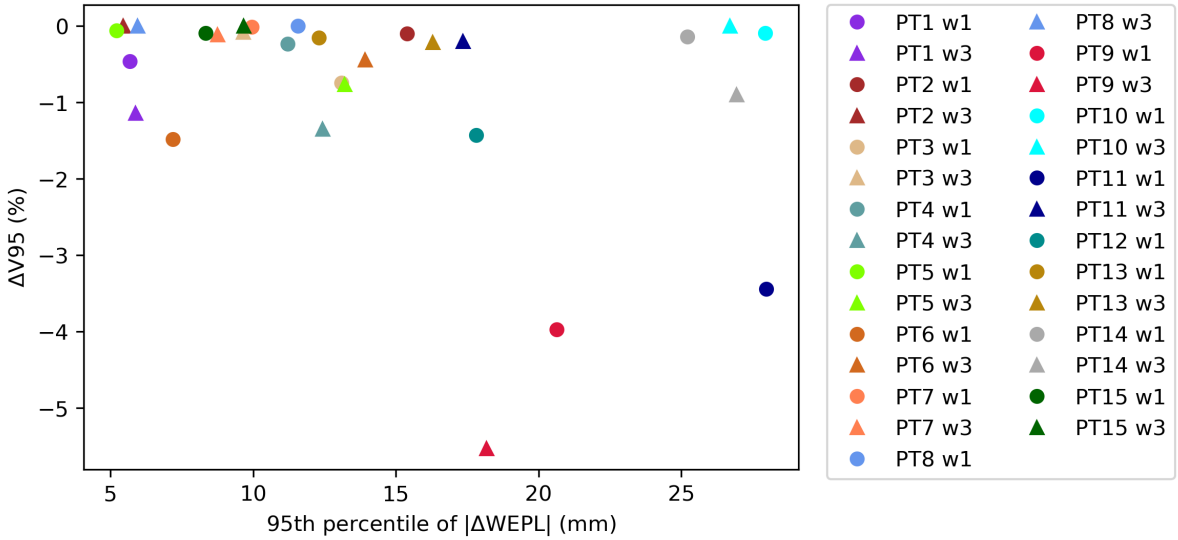

Figure 4.12: The 95th percentile of |ΔWEPL| and the relative change in CTV V95 for every patient rCT. *Abbreviation:* PT = patient, w = week.

4.5.3 Percentage of points with > 10 mm change in WEPL

Comparing the fraction of points with |ΔWEPL| > 10 mm between the group of failing plans and the group of accepted plans showed no significant difference, neither in week 1 ($p = 0.280$) nor in week 3 ($p = 1$). Figure 4.13 shows the association between the percentage of points with |ΔWEPL| > 10 mm and ΔV95. The Spearman's correlation coefficient showed that there was no significant correlation between the two ($r_S = -0.212$, $p = 0.110$).

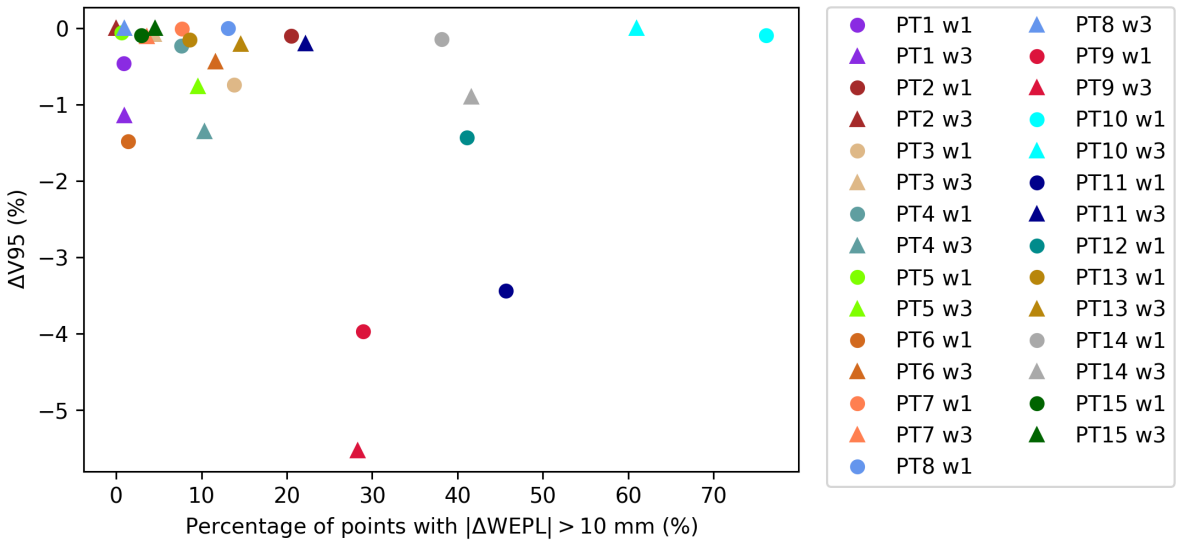

Figure 4.13: The percentage of points at the distal edge of CTV with more than 10 mm change in WEPL and the relative change in CTV V95 for every patient rCT. *Abbreviation:* PT = patient, w = week.

Distinguishing between increasing and decreasing WEPL, the percentage of points with $\Delta\text{WEPL} > 10$ mm (undershoot) and the percentage with $\Delta\text{WEPL} < -10$ mm (overshoot) were found for each patient rCT. There was a significant correlation between the degradation in target dose and the percentage of overshooting points ($r_S = -0.434$, $p = 0.019$) (Figure 4.14). For the percentage of undershooting points, there was no correlation with ΔV95 ($r_S = -0.008$, $p = 0.968$).

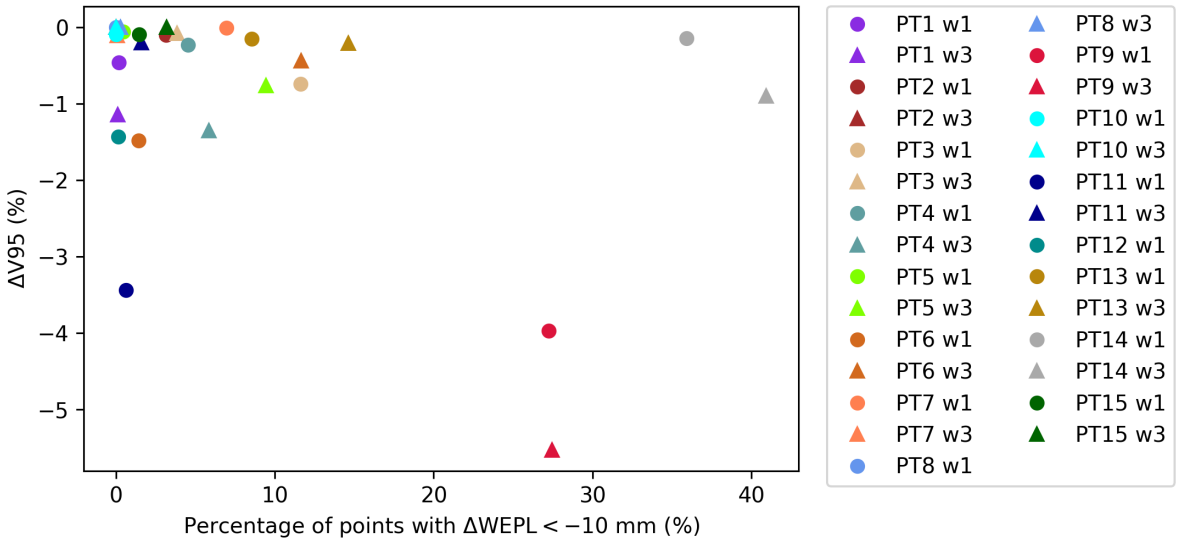

Figure 4.14: The percentage of points at the distal edge of CTV with more than 10 mm reduction in WEPL (overshoot) and the relative change in CTV V95 for every patient rCT. *Abbreviation:* PT = patient, w = week.

In Figure 4.14, patient 11 is an example of degradation in V95 that is most likely caused by a large fraction of undershooting points, while the fraction of overshooting points is low. To assess the degradation in V95 caused by an increasing or a decreasing WEPL, the ΔWEPL calculation on every patient rCT was classified as an overshooting or an undershooting case based on the majority of points. Figure 4.15 shows the result for the 10 mm WEPL change. With the classification, there was a significant correlation between degradation in target dose and the percentage of overshooting points ($r_S = -0.511$, $p = 0.036$), while there was no correlation for the undershooting points ($r_S = -0.063$, $p = 0.845$).

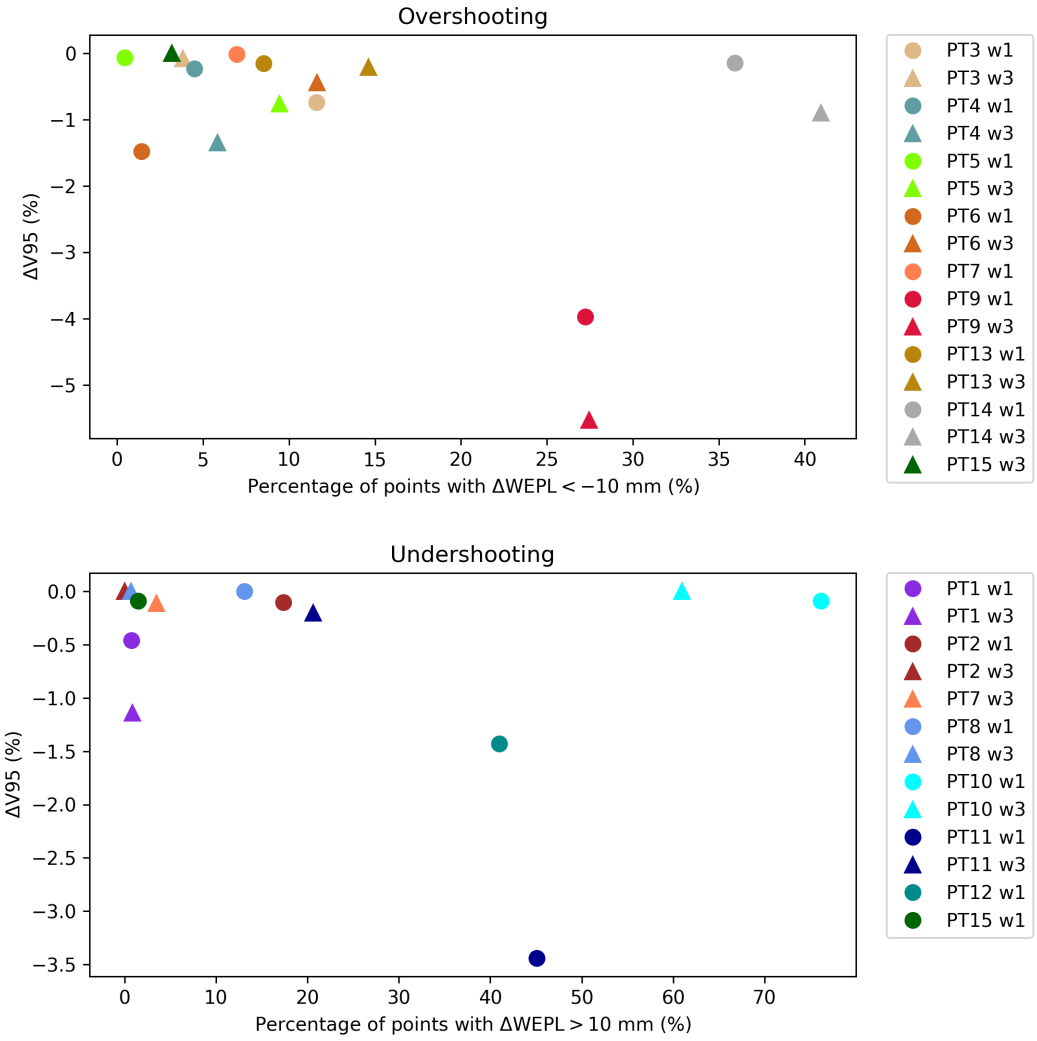

Figure 4.15: The percentage of points with more than 10 mm decrease in WEPL (upper figure) or more than 10 mm increase in WEPL (lower figure) plotted towards the relative change in CTV V95 for patient rCTs classified as overshooting or undershooting cases.
Abbreviation: PT = patient, w = week.

4.5.4 Percentage of points with > 3 mm change in WEPL

The percentage of points at the distal CTV edge with $|\Delta\text{WEPL}| > 3$ mm was not significantly different between the groups of failing plans and accepted plans, neither in week 1 ($p = 0.753$) nor in week 3 ($p = 0.885$). Figure 4.16 shows the association between the percentage of points with $|\Delta\text{WEPL}| > 3$ mm and ΔV95, which were not significantly correlated ($r_S = -0.153$, $p = 0.429$). After separating positive and negative changes, there were still no statistical significant correlations with the dose degradation neither for the overshooting points ($r_S = -0.492$, $p = 0.063$), nor for the undershooting points ($r_S = 0.159$, $p = 0.587$).

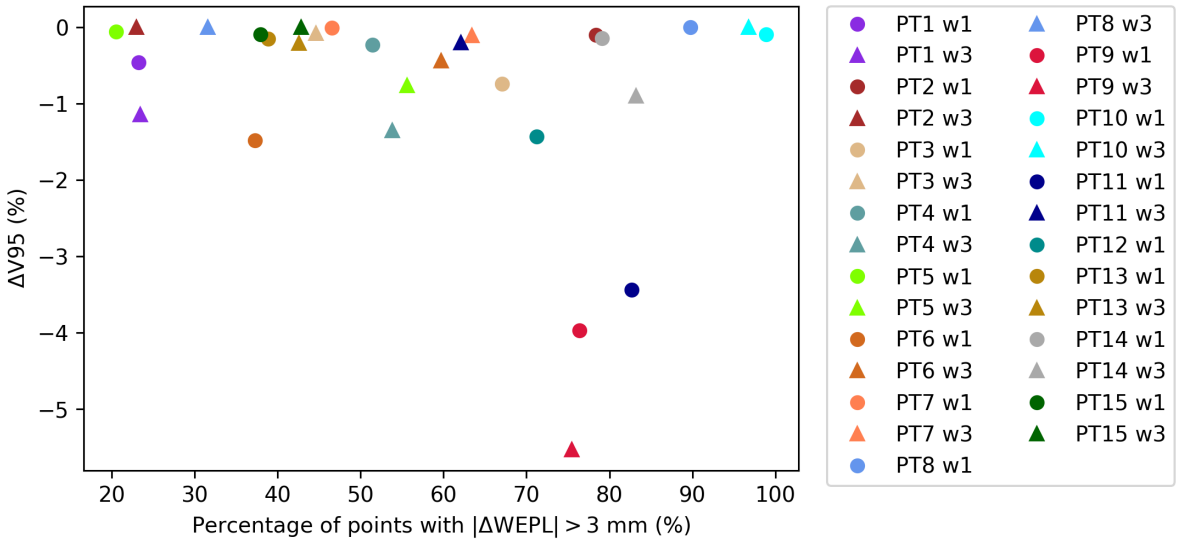

Figure 4.16: The percentage of points with more than 3 mm change in WEPL and the relative change in CTV V95 for every patient rCT. *Abbreviation:* PT = patient, w = week.

4.6 PATIENT EXAMPLES ON WEPL CALCULATION AND DOSE DEGRADATION

Patient 9

For patient 9, the mean $|\Delta\text{WEPL}|$ was 8.6 mm and 7.5 mm from the pCT to the rCT of week 1 and week 3, respectively. The percentage of points at the distal edge of CTV with $|\Delta\text{WEPL}| > 10$ mm was 29.0% in week 1 and 28.3% in week 3, and the majority had decreasing WEPL, indicating an overshoot of the proton beams. Considering only overshooting points, the percentage was 27.2% in week 1 and 27.4% in week 3. Figure 4.17 shows the WEPL calculation on the pCT and the image registration between the pCT and the rCT of week 3 for corresponding slices.

As predicted by the WEPL calculation, the dose distribution in Figure 4.18 shows that there was an overshooting of the proton beams and that the target coverage was deteriorated in the rCT of week 3. The ΔV95 for patient 9 was -3.97% in week 1 and -5.53% in week 3.

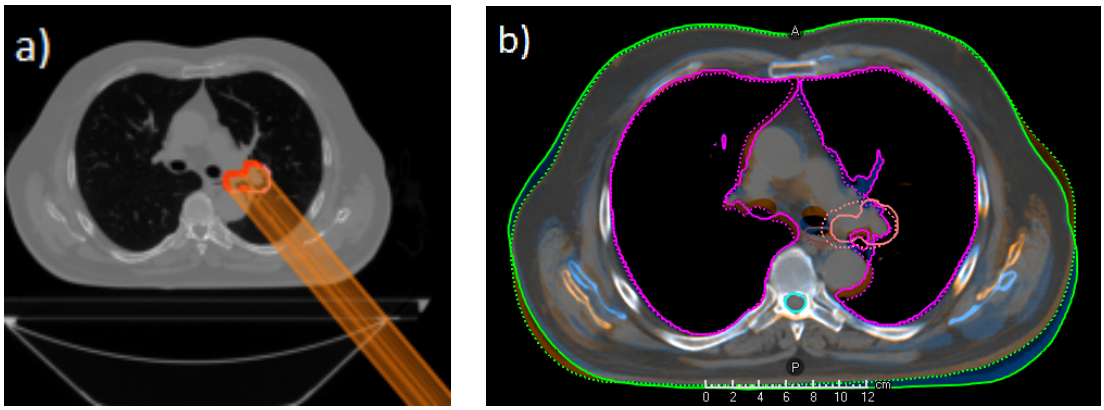

Figure 4.17: a) Illustration of the WEPL calculation for one field angle (blue line in Figure 4.18) in one slice of the pCT of patient 9. The orange lines are the lines along which the WEPL was calculated. *Delinations:* coral: CTV, red: distal edge of CTV. b) Image registration of the rCT of week 3 (orange shade) with the pCT (blue shade) for the same slice. *Delinations:* coral: CTV, pink: lungs, green: body structure. The dotted lines represent the delineations made on the rCT, while the filled lines represent the pCT.

This patient was treated with IMRT in DIBH, and the RTTs in the clinic reported that they had some trouble obtaining the same breathing level as on the pCT, which could affect the dose delivery. They also reported baseline shift and tumor regression. Studying the image registration of the rCT of week 3 with the pCT (Figure 4.17(b)) verified the tumor regression, but there was little changes in the lung volume. The image registration also shows that there was less tissue behind the left shoulder in the rCT than in the pCT, where one of the radiation fields entered the body. This may be due to a different fixation of the patient or a weight loss. One of the patient's doctors informed that the patient's weight was stable throughout the treatment course, but there might have been loss of muscle mass. The decreased amount of tissue in the proton beam path leads to a reduced WEPL and an overshooting of the proton beams.

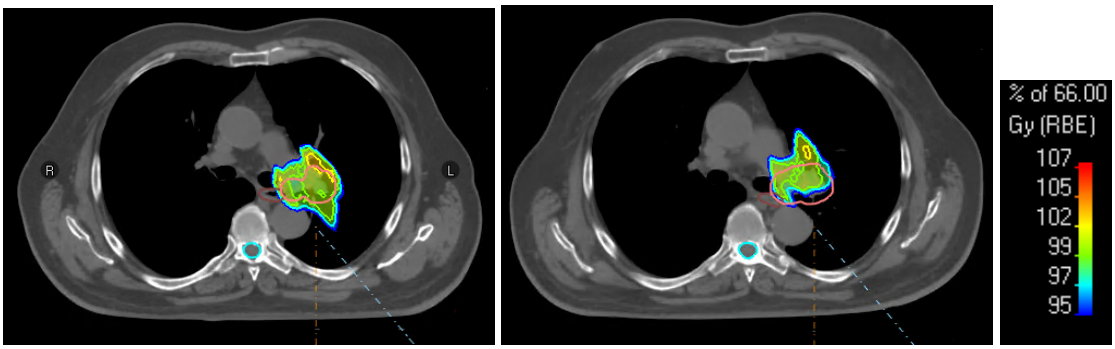

Figure 4.18: Dose distribution of the original IMPT plan of patient 9 on the pCT (left) and of the recalculation on the rCT of week 3 (right), shown in corresponding slices. The orange and blue dotted lines show the field angles for the incoming fields. *Delineations:* coral: CTV, cyan: spinal cord, brown: esophagus. The structures were delineated in the pCT and in the rCT. The color scale shows the dose in percentage of the prescribed dose, which was 66 Gy(RBE).

Patient 10

The largest WEPL changes were found for patient 10 (Figure 4.6). From the pCT to the rCTs the mean $|\Delta\text{WEPL}|$ was 15.3 mm in week 1 and 12.8 mm in week 3, mainly increasing (Figure 4.5). Figure 4.19 shows the WEPL calculation in the pCT and the image registration between the pCT and the rCT of week 1 for corresponding slices,

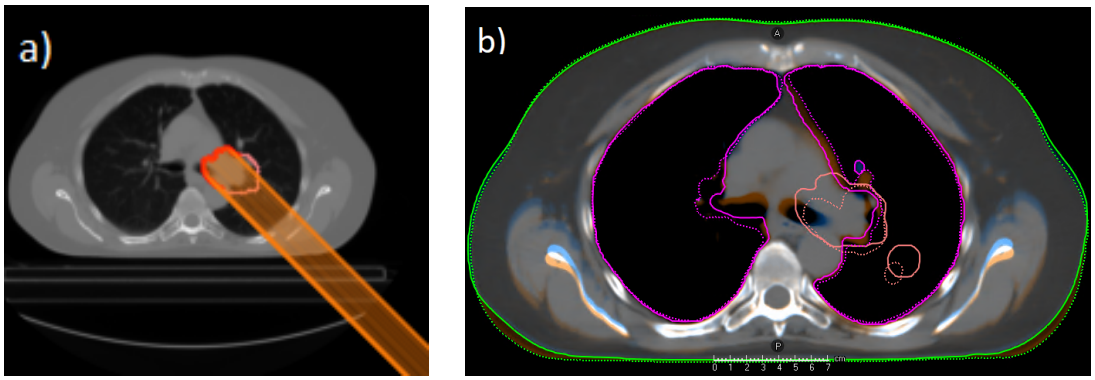

Figure 4.19: a) Illustration of the WEPL calculation for one field angle (blue line in Figure 4.20) in one slice of the pCT for patient 10. Orange lines are the lines along which the WEPL was calculated. *Delineations:* coral: CTV, red: distal edge of CTV. b) Image registration of the rCT of week 1 (orange shade) with the pCT (blue shade) for the same slice. *Delinations:* coral:CTV, pink: lungs, green: body structure. The dotted lines represent the delineations made on the rCT, while the filled lines represent the pCT.

The increasing WEPL indicates an undershooting of the proton beams, but for patient 10 the ΔV95 was -0.09% in week 1 and zero in week 3. As shown in Figure 4.20, the dose distribution was slightly changed in the recalculated IMPT plan, but the CTV remained covered. During the IMRT treatment, the RTTs registered a baseline shift. The image registration between the pCT and the rCT of week 1 (Figure 4.19(b)) revealed a smaller lung volume and change in the body contour as well, increasing the amount of tissue in the beam path in the rCT, as predicted by the WEPL calculation.

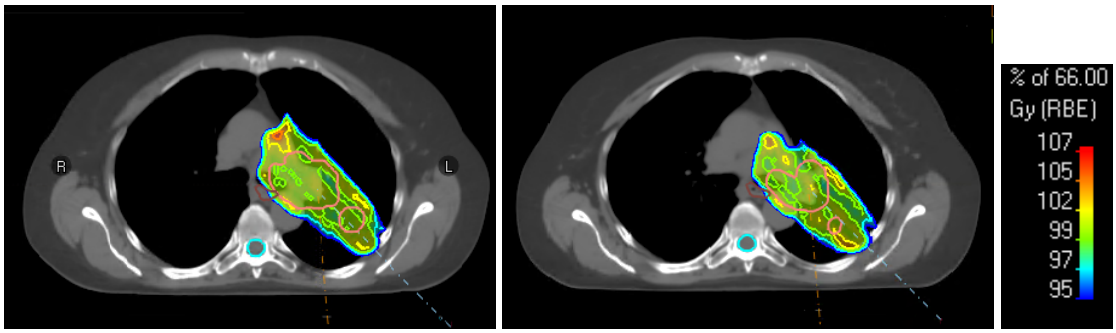

Figure 4.20: Dose distribution of the IMPT plan of patient 10 on the pCT (left) and of the recalculation on the rCT of week 1 (right), shown in corresponding slices. The orange and blue dotted lines show the field angles for the incoming fields. *Delinations:* coral: CTV, cyan: spinal cord, brown: esophagus. The color scale shows the dose as percentage, from 95% to 107% of the prescribed dose, which was 66 Gy(RBE).

5

DISCUSSION

The WEPL calculation developed in this thesis did not seem to correlate with the dose degradation in IMPT plans for LA-NSCLC. Considering ΔWEPL and ΔV95 from planning CT (pCT) scans to repeat CT (rCT) scans, statistically significant correlation was found only between ΔV95 and the percentage of points at the distal edge of CTV with > 10 mm WEPL overshoot. Since no correlation was found for any of the other quantifications of ΔWEPL, the second hypothesis of this study was rejected. There was no significant difference in ΔWEPL between the group of failing plans ($\Delta V95 < -1\%$) and the group of accepted plans ($\Delta V95 \geq -1\%$), rejecting also the third hypothesis. The ΔWEPL values spanned large intervals, which might be due to anatomical changes or a consequence of the inaccurate prediction of the RSP, which had a relative error of 4.6%. With this result, also the first hypothesis of the study was rejecting.

5.1 CORRELATION TESTING

As dose calculations are based on the range of protons, a change in WEPL to the distal edge of CTV was expected to cause a change in dose to the CTV as well. Previous studies have found statistically significant correlations between the mean |ΔWEPL| and degradation in CTV V95 [12, 13]. The results of this study showed that there were no significant correlations between the degradation in dose and the tested measures of ΔWEPL, except the percentage of points with > 10 mm WEPL overshoot.

There were no significant correlations, but it was found that among the 7 failing plans, 5 had > 10 mm WEPL change in more than 10% of the points at the distal CTV and 4 had a 95th percentile of |ΔWEPL| > 15 mm. The 95th percentile was > 18 mm for the three recalculated plans with the largest dose degradation (Patient 9 week 1, patient 9 week 3 and patient 11 week 1). With WEPL these patients could be identified and be evaluated for adaptive therapy. At the same time, larger WEPL changes were found for plans with less dose degradation and no need for adaptions (for instance patient 10).

Even though the results disproved the hypotheses of this study, they were mostly in agreement with the findings of Gorgisyan et al. [11]. The only parameter they found to be correlating with the dose degradation was the percentage of voxels at the distal edge of PTV with > 3 mm WEPL undershoot. This is in contrast to the present study, where the only significant correlation was found for overshooting cases.

Gorgisyan et al. [11] reported that 6/15 patients had > 3 mm WEPL undershoot in $\geq$ 15% of the voxels, and that 3 of these had more than 5% degradation in CTV V95, supporting the finding of a significant correlation. In the present study, the number of patient rCTs with the same amount of undershooting points was slightly higher, with 8/15 in week 1 and 6/14 in week 3. However, none of these had more than 5% dose

degradation, but 4 had more than 1%. Only one patient in the present study had more than 5% degradation (patient 9, week 3), and the WEPL calculation on this rCT showed undershoot in only 6.27% of the points, but overshoot in 69.2%. There were generally more overshooting than undershooting in the present study. More than 3 mm overshoot in $\geq$ 15% of the points was shown for 7/15 rCTs in week 1 and 10/14 in week 3. In total 4 of these had more than 1% dose degradation of which one was more than 5%. The correlation between dose degradation and the amount of overshooting points was significant only when increasing the threshold to 10 mm.

In general, the present study involved a higher degree of WEPL changes and a lower degree of dose degradation as compared to previous studies [11–13]. It should be noted that Gorgisyan et al. calculated the WEPL to distal voxels of the PTV instead of the CTV, which may explain why there were larger WEPL changes in the present study. For instance, if there was a baseline shift parallel to the beam axis moving the tumor outside the delineated CTV, while remaining inside the PTV. However, this should correlate better with dose to the CTV. In the following sections, other possible reasons for these results will be explored.

5.2 DOSE DEGRADATION

Dose degradation in the CTV was found to be minor in the present study. Considering the acceptance criterion $\Delta V95 > -1\%$ for the recalculated IMPT plans, 4/15 plans failed in week 1 and 3/14 plans failed in week 3. Hoffmann et al. [4] reported that 21/23 LA-NSCLC patients treated with IMPT were in need for adaptions when using a similar criterion (CTV V95 > 99%). In the study of Gorgisyan et al. [11] they reported that 12/15 patients had $\Delta V95 < -5\%$, while in the present study there was only one patient with that large dose degradation.

5.2.1 Robust optimisation

Unlike the plans in the studies by Hoffmann et al. and Gorgisyan et al., the IMPT plans in the present study were robust optimised, resulting in less dose degradation. Robust optimisation takes into account setup and range variations. As argued by Li et al. [38], although anatomical changes are not accounted for, the plans were less sensitive to these as well, since robust optimisation in general minimises dose variations under different uncertainty scenarios. However, other studies have reported that adaptions are required for IMPT plans even with robust optimisation. Chang et al. [29] found that adaptive planning was necessary for 9/34 lung cancer patients (26.5%), where of 7 was due to less than 95% coverage of the CTV in the recalculated plans on rCT acquired weekly or after 2 to 3 weeks of treatment. Szeto et al. [39] considered LA-NSCLC patients and compared the accumulated dose distributions during the treatment course to the planned dose distribution, and accepted a reduction of $\leq$ 2 GyE (equivalent dose) in the minimum dose to 99% of the gross target volume (GTV) (D99). They found 8/16 plans (50%) to be failing.

With the acceptance criterion used in the present study, the robust optimised IMPT plans failed in 7/29 fractions (24.1%) in total. One plan failed in both week 1 and week 3, hence, in total 6/15 plans (40%) failed. In discussion with an oncologist, only one of these plans had a dose degradation that was critical enough to require adaptions (patient 11 w1). For the other cases, the lack of dose was mainly at the edges of CTV and the dose to the tumor would probably be sufficient in the composition of several fractions [1].

Due to the robust optimisation of the IMPT plans, the CTV dose was less sensitive to changes in WEPL. One important point is that the WEPL was calculated along straight paths from the entrance of the radiation field to the distal edge of CTV. In a robust optimised IMPT plan, the proton range along the straight path is not the only factor with impact on the target coverage. As can be seen in the IMPT plan in Figure 3.6, some Bragg peaks are positioned outside the target volumes, optimised to account for setup and range variations. A WEPL change along the path of one pencil beam would affect the dose delivery of this single beam, but as the total dose to the CTV is composed of many individual beams, a change in WEPL along one path has little influence. The WEPL was analyzed along several parallel paths to the distal edge of CTV. The paths to points outside the target were not taken into account, hence, the WEPL calculations did not include all changes with impact on the target coverage.

5.2.2 Different calibration curves

Another possible explanation for the weak correlation between changes in WEPL and dose degradation is that the WEPL calculations were based on RSP values obtained using the calibrated HLUT, while the dose calculations were done in RayStation, using a different calibration curve. Hence, the calculations of the proton range differ, possibly causing the changes in dose not to correlate with changes in WEPL.

5.3 WEPL CHANGES

Evaluating WEPL changes from the pCT to the rCTs of week 1 and week 3 for every patient indicated that there were changes in the patients' anatomy and tissue densities during the treatment course. As WEPL changes were evaluated in every point on the distal edge of CTV relative to each field angle in every image slice, a large amount of data was obtained for each patient rCT. At the most, 8195 points were counted for patient 14. The box plot in Figure 4.4 shows that there was a wide distribution of ΔWEPL values and many outliers for most patient rCTs. At the most, the difference between the largest and smallest ΔWEPL was 115.9 mm (Patient 11 week 1). For patient 10, whose WEPL values are presented in Figure 4.5, the values spanned an interval of 51.7 mm in week 1 and 55.9 mm in week 3.

For further evaluation, parameters such as the mean $|\Delta\text{WEPL}|$ per pCT were extracted, inspired by previous studies [11, 12]. Subsequently, it was discovered that the $|\Delta\text{WEPL}|$ values were not normally distributed, making the mean $|\Delta\text{WEPL}|$ an inaccur-

ate measure of the data. Hence, the median values were calculated and it was found that the mean $|\Delta\text{WEPL}|$ and median $|\Delta\text{WEPL}|$ were significantly different, but the correlation testing with dose degradation gave equivalent results.

Neither the mean nor the median $|\Delta\text{WEPL}|$ were considered to be good quantifications as they averaged over numerous widely distributed values for each rCT. A better measure of the degree of WEPL changes was the 95th percentile of $|\Delta\text{WEPL}|$. The correlation testing of this parameter with the dose degradation showed a correlation coefficient of -0.354 with $p = 0.059$, which is close to significant. The larger WEPL changes seem to have more impact on the dose.

The percentage of points with $|\Delta\text{WEPL}| > 10$ mm was also considered to be a good quantification of the WEPL changes. Other studies have used 3 mm as the threshold instead of 10 mm [11, 14]. In the present study, the 3 mm threshold was applied as well in order to compare with previous studies, but a very large percentage of the points had $|\Delta\text{WEPL}| > 3$ mm, making it difficult to distinguish between rCTs with more or less changes. All 29 rCTs had $|\Delta\text{WEPL}| > 3$ mm in at least 20% of the points, while in the study by Gorgisyan et al. the same was valid for 3 out of 15 CTs [11]. The larger ΔWEPL values in the present study might be due to a different approach for the calculation, which will be discussed in Section 5.4. It might also be due to more anatomical changes.

5.3.1 Correlation with observed anatomical changes

By studying the patient CT scans and the reports from the RTTs, it appeared that more anatomical changes where observed for the patients with large percentages of points with $|\Delta\text{WEPL}| > 10$ mm (Tables 4.3 and 4.4). For patients 10 and 14, who both had relatively large WEPL changes, there were observed baseline shift or tumor regression in addition to changes in lung volume and in the body contour, which may have caused the large WEPL changes.

Changes in lung volume due to different breathing pattern, can change the amount of lung tissue relative to air that is traversed by the proton beam. A change in the positioning of the patient could also add or remove tissue from the beam path, changing the WEPL. A baseline shift or a regression of the target volume could induce a change in the WEPL to the distal edge of CTV. Especially since the CTV delineated at planning was used to define the paths for the WEPL calculation, a shift of the tumor away from the delineation could result in a drastic reduction of WEPL for the points where the tumor has moved away from, which was typically replaced by air or lung tissue.

For patients with smaller percentages of points with large WEPL changes, there were less anatomical changes. Baseline shifts and changes in body contour were reported also for these, but typically as one change at a time. For patients 1, 5, 6 and 15 who had the lowest degrees of WEPL changes in week 1, little or no anatomical changes were observed. For patient 2, who had 0% of the points with $|\Delta\text{WEPL}| > 10$ mm in week 3, no anatomical changes were observed in the rCT of week 3.

5.4 THE WEPL CALCULATION

The large variation of ΔWEPL values, and the weak correlation with dose, may be true results, but it may also originate from errors in the WEPL calculation. Uncertainties in predicting the RSP values and uncertainties in the definition of the distal CTV may have contributed to errors.

Testing the WEPL calculations on the water phantom indicated that they were correct. The physical distances for the three field lines defined in Figure 3.3 were measured in ImageJ and calculated in Python, obtaining equal values (Table 4.2). The WEPLs along the two paths in water were almost equal to the physical distances, with WEPL being 1.8 mm longer for both. These deviations were considered to be a small, systematic errors with little impact on the results, as the aim was to compare changes in WEPL between CT scans. One of the paths in water was oblique, confirming that the chord length involved in the WEPL was defined correctly also when the line crossed the pixel edges at oblique angles. The WEPL for the path including pixels with air was shorter than for the line in water of equal physical distance. This was expected, since the RSP of air is approximately 0. With these results, the computation of WEPL was considered to be successful. However, the WEPL is directly connected to the RSP calculations, and the RSPs of the water inserts in the Gammex phantom were predicted with low relative errors. For other tissue types with more uncertainty in the RSP prediction, such as the lungs, the WEPL calculations may have more errors.

5.4.1 Uncertainties in the RSP prediction

The HLUT used in the WEPL calculations was obtained through characterising the CT scanner with a single-energy CT scan of the Gammex phantom and stoichiometric calibration using the properties of 60 human tissues [42]. The RSP values were predicted with a mean relative error (MRE) of 4.6%. The accuracy of the RSP prediction was lower than expected, as an uncertainty less than 3.5% was hypothesised.

Among the tissue substitute inserts in the Gammex phantom, the Lung300 insert contributed the most to the error in the RSP prediction with a relative error of 14.5% (Figure 4.2). The low RSP values of lung tissue contribute to a large relative error. Lung tissue, as compared to other tissue types, is reported to carry more uncertainties in CT imaging and, hence, in the RSP prediction [18]. The Lung300 insert had a relative error 1.7 times larger than the one for the Lung450 insert, which was 8.5%. The relative electron density $\hat{\rho}_e$ of the Lung300 insert was 0.281, while of the Lung450 insert it was 0.458. This indicates that the calculation of RSP is highly sensitive to variations in $\hat{\rho}_e$, as stated in Section 2.3.2. The second largest relative error was 10.0% for the Cortical bone insert. The insert had the largest $\hat{\rho}_e$ with 1.696 and a relative mass density $\hat{\rho}$ of 1.824g/cm^3. High-density materials have been reported to give more inadequate calibration than tissue materials [41, 53].

There are several steps in the calibration process which could contribute to the uncertainty. First of all, there are uncertainties in the CT imaging of the Gammex phantom.

In the study by Annette Høisæter [51], a MRE of 3.5% was obtained. The HLUT was made in a similar manner as in the present study, with the CT scan being the only difference. First of all, different scanners were used. In the study by Høisæter, a Siemens SOMATOM scanner was used, which can be assumed to have a superior image quality as compared to the Philips CT Big Bore scanner. The Big Bore scanner is designed for radiation oncology and therapy with fixation tools mounted to it. Hence, the gantry opening is wider with a larger distance between the source and detector, increasing the amount of scattering [54]. Secondly, Annette used a slice thickness of 5 mm, while 3 mm was used in the present study, which could increase the imaging noise. However, it has been reported that slice thickness has negligible effect of the stoichiometric calibration curve [53]. The exposure was more than doubled in the present study, with 615 mAs in the present study and 300 mAs in Høisæter's study, which should reduce the amount of noise. The overall MRE was higher in the present study, but for the lung inserts, the relative errors were lower than in the study by Høisæter. That might have to do with the imaging protocol for lung cancer patients that was used.

Uncertainties in the CT scan, together with calculation errors, can result in inaccurate calculation of the scanner characteristic k-values. The calculated value of k_1 was equal to the one of Høisæter, while k_2 was equal to the one of Gomà et al. [41]. Based on that, the obtained k-values were considered to be reasonable values. Subsequently, the obtained k-values were used to calculate synthetic HU values for the Gammex inserts, which gave some error as compared to the measured HU values. For instance, the synthetic HU of the water insert was calculated to 0, while the measured one was -9.0. This might be due to a long time since the CT scanner was last calibrated with water, which is done twice a year. It might be that a new water calibration would improve the results. The inaccurate calculation of k-values has an impact on the HLUT, and this step should be validated.

In calculation of the theoretical RSP values for calibrating the HLUT, the I-values contributed a lot to the uncertainty. The current clinical derivation using I-values of solid state elements was applied in the present study. With optimised I-values, as presented by Bär et al. [47], the range uncertainty contribution from the I-values could be 0.47%, as compared to the current estimate of 1.5% [17]. The choice of break points in the HLUT is another step of the calibration which may have contribute to errors. Precise guidelines for this step were not found in the literature, and different approaches were used in different studies [41, 50, 53]. In the present study, the choice of break points was done by trial-and-error, testing several numbers of points and their values in order to achieve the most accurate RSP prediction. Using five break points gave better accuracy, but to avoid overfitting, it was decided that using two break points was more appropriate. More sophisticated methods for optimizing the HLUT have been investigated by Krah et al. [55], but were not considered for this study.

By using a dual-energy CT (DECT) in the calibration, the accuracy of the RSP prediction would probably be substantially improved. Hünemohr et al. [56] reported that the RSP was predicted with an accuracy of 1% using DECT. A recent review article by Wohlfahrt and Richter [49] concluded that there is broad evidence for the clinical benefits of

DECT in proton therapy planning. In the present study, the HLUT calibration was performed with images acquired at the same single-energy CT scanner as the images of the LA-NSCLC patients. Even the same imaging protocol was used, which was meant for planning of photon radiotherapy. With another protocol the accuracy of RSP prediction could be improved.

Despite the inaccuracy, the RSP prediction was considered to be valid for the WEPL calculations in the present study, as the aim was to look for differences between CT scans. Using the same imaging protocol and the same algorithm, with the same accuracy, for all CT scans, it should be possible to evaluate differences between the scans and indirectly derive changes in the proton range.

5.4.2 Definition of the target

In the present study, the WEPL was evaluated to the distal edge of CTV, while the other studies used the distal edge of PTV [11, 13] or an isocenter plane [12]. The CTV was considered to be a better choice for correlating the WEPL calculations to dose degradation in the CTV. In addition, the PTV is not always delineated for modern proton therapy planning, as robust optimisation is commonly used instead.

Regarding the robust optimisation, a possible improved approach would be to calculate the WEPL to every individual Bragg peak position instead of all points at the distal edge of CTV. In the study by Gorgisyan et al. [13] they calculated the WEPL to the possible spot positions at the PTV structure and averaged the WEPL over the individual pencil beams. In the plans of the present study, which are robust optimised, there are spot positions also outside the target. The calculation would be more complicated, but achievable. The spot positions could be extracted from the IMPT plans in RayStation together with the spot weights, which could be used to weigh WEPL differences with varying impact on the dose. However, the positions of the Bragg peaks are calculated in RayStation taking into account the tissue densities from the CT scan and the RSP of the protons. When recalculating the plan on a rCT, the spot positions change (Figure 3.6). In order to analyse the WEPL differences point by point, which is done in this study, the Bragg peak positions in the pCT would need to be used also in the rCT. However, with the robust optimisation, the new Bragg peak positions of the recalculated plan would probably ensure dose to the target, so that the correlation between ΔWEPL and ΔV95 would be weak nevertheless.

Figure 3.7(a) shows a problem with the definition of the distal edge of CTV. For points at the left and right edges, where the structure tends to curve, the paths along which the WEPLs were calculated are overlapping. Some points may also represent the same pixels, leading to a double counting of the line to that pixel. Hence, anatomical changes along these paths contribute more to the total ΔWEPL than other paths. This error probably affected the results, but the exact consequences were not quantified. For improvement, a correction should be added to the algorithm, ensuring that overlapping paths are only counted once and that they are all weighted equally.

Another issue, which 3.7(b) shows an example of, is that the definition of the distal edge of CTV is affected by the fact that the images are square. The paths entering in the corner of the image typically have a longer distance to the CTV. Hence, some points on the distal surface are replaced by other points on the structure of which the straight paths enter in the corner. An alternative approach, which was also tested, is using the points with the longest WEPL to define the distal edge of CTV, neglecting the distance travelled in air. With this approach some points at the distal edge were replaced by others which had more dense tissues, such as bones, included in their paths. Due to the incorrect definition, changes in WEPL for points not being at the distal edge of CTV may have contributed to the total ΔWEPL. This is, however, a systematic error affecting the pCT and the corresponding rCTs equally as the same structures were used.

In the WEPL calculation, the CTV structure delineated on the pCT was used as the target volume also in the rCTs, although the CTV had been re-delineated on the rCTs. The primary reason for this choice was to have equal structures in each of the CT scans, so that changes in WEPL could be evaluated point by point. However, this method does not take into account tumor changes in the distal part, for instance a progression beyond the delineation. These are changes that could result in underdosage of the CTV, but would not be detected in the WEPL analysis. Gorgisyan et al. [13] also used the same PTV delineations. The re-delination could have been used instead but, then, one point of the structure in the pCT would not correspond to one point in the rCT. The same would be the case when using the Bragg peak positions in the rCT as discussed above. The WEPLs would have to be averaged for each image slice before looking for changes between the scans. Positive WEPL changes along one path could then be smeared out by negative WEPL changes along another path in the image. There would also be uncertainty related to the re-delineation of target volumes [57].

Another uncertainty is the rigid image registration, which was applied to locate the CTV in the rCT scans before calculating the WEPL. The image registration was performed by the candidate using Eclipse and matching on the bony anatomy in the target region. There might be errors in the registration, resulting in misplacing the CTV in the rCTs. Calculating the ΔWEPL for a point that has been misplaced in the rCT could give completely wrong results. Nevertheless, the same image registration was applied in the recalculation of the IMPT plans on the rCTs, from which the degradation in dose was found. In treatment delivery, rigid image registration was used to position the patients similarly as on the pCT. The uncertainty related to the registration in the present study reflects some of the uncertainties present in treatment.

5.5 DIFFERENCE BETWEEN 4DCT AND DIBH CT

In the present study, the average intensity projection (AIP) of 4DCT scans were used for the majority of the patients, while for the 3 patients who were treated in deep inspiration breath hold (DIBH), the DIBH CT scans were used. For the 6 DIBH rCTs (3 in week 1 and 3 in week 3), there was a significant correlation between the dose degradation of the IMPT plans and both the mean $|\Delta WEPL|$ and the percentage of points with > 10 mm

and > 3 mm WEPL changes ($r_S = 0.886$, $p = 0.019$ for all). This could be a coincidence due to the small number of plans, but it might also be reasonable.

In the 4DCT, the amount of lung tissue and amount of air in the lungs varies throughout the acquisition. In the AIP, the amount of tissue is averaged over the different breathing phases and some pixels may contain a mix of lung tissue and air. If the patient's breathing motion changes from the pCT to the rCT, the distribution of lung tissue and air (density) in the points of the AIP changes. From the evaluation of the RSP prediction in the Gammex phantom, we know that the uncertainty is highly dependent on the density of the lung tissue (Lung300 or Lung450). This means that the uncertainty in the RSP prediction and, hence, the WEPL calculation may vary from the pCT to the rCT. For the DIBH CTs, every pixel contains either lung tissue or air, roughly speaking. The uncertainty in the WEPL calculation is equal for the pCT and rCT, possibly making the calculation on the DIBH CTs more accurate.

5.6 FUTURE WORK

A quality assurance of the WEPL calculation developed in this thesis should be performed, as it seems to have potential for improvements. The analysis should also be validated for a larger patient group and take into account changes in dose to OARs as well. Increased doses to OARs can also be a consequence of changes in WEPL, and could trigger plan adaptions. It should also be investigated whether the robust optimisation of the IMPT plans makes WEPL calculations to the target volume rather useless for detecting dosimetric changes.

To utilize the true potential of WEPL in adaptive therapy, it should be connected to the CBCT scans taken before every treatment fraction as part of clinical routine, so that rCTs are not needed to decide whether adaptions should be considered. However, since the CBCT typically has more uncertainty in the HU values than the standard CT, WEPL calculations are more challenging. A scattering correction to the CBCT would be needed, or alternatively, creating virtual CT scans based on the pCT and CBCTs, as done by Veiga et al. [14]. However, this is a time consuming process due to the deformable image registration needed.

As proton therapy centers are opening in Norway in a couple of years, good treatment protocols should be developed. Proton therapy can give LA-NSCLC patients more gentle treatment, but with anatomical changes commonly occurring, good adaptive protocols are needed to utilize the true potential. Even with robustly optimised IMPT plans, adaptions are still needed for some LA-NSCLC patients, but the WEPL might not be the best approach to identify them.

6

CONCLUSION

In this thesis, the feasibility of WEPL as a decision tool in adaptive proton therapy of LA-NSCLC has been assessed by comparing changes in WEPL (ΔWEPL) with dose degradation in the CTV (ΔV95) from planning CT scans to repeat CT (rCT) scans, acquired in week 1 and week 3 of the treatment course. A calculation of the WEPL from CT images was successfully implemented, including RSP prediction with an accuracy of 4.6%. Evaluated to the distal edge of the CTV for 15 LA-NSCLC patients, the ΔWEPL did not correlate with the ΔV95 of robust optimised IMPT plans. There were minor dose degradations, where $\Delta V95 < -1\%$ was found for $7/29$ recalculated plans on the rCTs. The WEPL changes were not found to be significantly larger for these than for plans with less dose degradation.

This study suggests that WEPL is not a feasible tool to identify patients with dose degradation in treatment of LA-NSCLC with robust optimised IMPT. Regarding target coverage, the plans were robust towards most of the anatomical changes detected by the WEPL calculations. However, it should be investigated if the robust optimisation was the reason for these findings, or if it was due to uncertainties in the WEPL calculation. If improvements make WEPL able to predict dose deterioration in robust IMPT plans, it should be connected to CBCT scans, so that rCT scans are not needed to identify patients in need of adaption.

BIBLIOGRAPHY

[1] Ragnvaldsen, Vilde. 'Adaptions in Photon and Proton Radiotherapy of Locally Advanced Non-Small Cell Lung Cancer', 2021.

[2] Cancer Registry of Norway. *Cancer in Norway 2020 - Cancer incidence, mortality, survival and prevalence in Norway.* Tech. rep. 2021.

[3] Hall, Eric J. and Giaccia, Amato J. *Radiobiology for the Radiologist*. 8th ed. Philadelphia: Wolters Kluwer, 2019.

[4] Hoffmann, Lone et al. 'Adaptation is mandatory for intensity modulated proton therapy of advanced lung cancer to ensure target coverage'. *Radiotherapy and Oncology*, 2017.

[5] Ma, Li et al. 'A current review of dose-escalated radiotherapy in locally advanced non-small cell lung cancer'. *Radiology and Oncology* 53, 2019.

[6] Bradley, Jeffrey D. et al. 'Long-Term Results of NRG Oncology RTOG 0617: Standard- Versus High-Dose Chemoradiotherapy With or Without Cetuximab for Unresectable Stage III Non–Small-Cell Lung Cancer'. *Journal of Clinical Oncology* 38, 2020.

[7] Gjyshi, Olsi and Liao, Zhongxing. 'Proton therapy for locally advanced non-small cell lung cancer'. *The British Journal of Radiology* 93, 2020.

[8] Chang, Joe Y. et al. 'Significant reduction of normal tissue dose by proton radiotherapy compared with three-dimensional conformal or intensity-modulated radiation therapy in Stage I or Stage III non–small-cell lung cancer'. *International Journal of Radiation Oncology*Biology*Physics* 65, 2006.

[9] Wink, Krista C. J. et al. 'Particle Therapy for Non-Small Cell Lung Tumors: Where Do We Stand? A Systematic Review of the Literature'. *Frontiers in Oncology* 4, 2014.

[10] Chang, Joe Y. et al. 'Consensus Guidelines for Implementing Pencil-Beam Scanning Proton Therapy for Thoracic Malignancies on Behalf of the PTCOG Thoracic and Lymphoma Subcommittee'. *International Journal of Radiation Oncology*Biology*Physics* 99, 2017.

[11] Gorgisyan, Jenny et al. 'Feasibility of Pencil Beam Scanned Intensity Modulated Proton Therapy in Breath-hold for Locally Advanced Non-Small Cell Lung Cancer'. *International Journal of Radiation Oncology*Biology*Physics* 99, 2017.

[12] Casares-Magaz, Oscar et al. 'A method for selection of beam angles robust to intrafractional motion in proton therapy of lung cancer'. *Acta Oncologica* 53, 2014.

[13] Gorgisyan, Jenny et al. 'Impact of beam angle choice on pencil beam scanning breath-hold proton therapy for lung lesions'. *Acta Oncologica* 56, 2017.

[14] Veiga, Catarina et al. 'First Clinical Investigation of Cone Beam Computed Tomography and Deformable Registration for Adaptive Proton Therapy for Lung Cancer'. *International Journal of Radiation Oncology*Biology*Physics* 95, 2016.

[15] Zhang, Miao, Zou, Wei and Teo, Boon-Keng Kevin. 'Image guidance in proton therapy for lung cancer'. *Translational Lung Cancer Research* 7, 2018.

[16] Bentefour, El Hassane et al. 'Using CBCT for pretreatment range check in proton therapy: a phantom study for prostate treatment by anterior-posterior beam'. *Journal of Applied Clinical Medical Physics* 16, 2015.

[17] Paganetti, Harald. 'Range uncertainties in proton therapy and the role of Monte Carlo simulations'. *Physics in Medicine and Biology* 57, 2012.

[18] Yang, Ming et al. 'Comprehensive analysis of proton range uncertainties related to patient stopping-power-ratio estimation using the stoichiometric calibration'. *Physics in Medicine and Biology* 57, 2012.

[19] National Cancer Institute. *Non-Small Cell Lung Cancer Treatment (PDQ®)–Patient Version*. URL: https://www.cancer.gov/types/lung/patient/non-small-cell-lung-treatment-pdq (visited on 24/09/2021).

[20] Drugs.com. *Lung Cancer Guide: Causes, Symptoms and Treatment Options*. URL: https://www.drugs.com/health-guide/lung-cancer.html (visited on 24/09/2021).

[21] Institutt for kreftgenetikk og informatikk, Oslo Universitetssykehus. *LUNGEKREFT*. URL: https://kreftlex.no/Lungekreft (visited on 24/09/2021).

[22] Brierley, James, Gospodarowicz, Mary K and Wittekind, Christian. *TNM classification of malignant tumours*. 8th ed. John Wiley & Sons, Inc., 2017.

[23] Helsedirektoratet. *Nasjonalt handlingsprogram med retningslinjer for diagnostikk, behandling og oppfølging av lungekreft, mesoteliom og thymom*. Tech. rep. 2021.

[24] LUNGevity. *Lung Cancer Staging | LUNGevity Foundation*. URL: https://www.lungevity.org/for-patients-caregivers/navigating-your-diagnosis/lung-cancer-staging (visited on 24/09/2021).

[25] Nguyen, Quynh-Nhu et al. 'Long-term outcomes after proton therapy, with concurrent chemotherapy, for stage II–III inoperable non-small cell lung cancer'. *Radiotherapy and Oncology* 115, 2015.

[26] Iwata, Hiromitsu et al. 'Concurrent Chemo-Proton Therapy Using Adaptive Planning for Unresectable Stage 3 Non-Small Cell Lung Cancer: A Phase 2 Study'. *International Journal of Radiation Oncology*Biology*Physics* 109, 2021.

[27] Kim, Nalee et al. 'Proton beam therapy reduces the risk of severe radiation-induced lymphopenia during chemoradiotherapy for locally advanced non-small cell lung cancer: A comparative analysis of proton versus photon therapy'. *Radiotherapy and Oncology* 156, 2021.

[28] Liao, Zhongxing et al. 'Bayesian Adaptive Randomization Trial of Passive Scattering Proton Therapy and Intensity-Modulated Photon Radiotherapy for Locally Advanced Non–Small-Cell Lung Cancer'. *Journal of Clinical Oncology* 36, 2018.

[29] Chang, Joe Y. et al. 'Clinical Implementation of Intensity Modulated Proton Therapy for Thoracic Malignancies'. *International Journal of Radiation Oncology*Biology*Physics* 90, 2014.

[30] Paganetti, Harald. 'Proton Relative Biological Effectiveness – Uncertainties and Opportunities'. *International Journal of Particle Therapy* 5, 2018.

[31] Rørvik, Eivind. 'Analysis and Development of Phenomenological Models for the Relative Biological Effectiveness in Proton Therapy'. PhD thesis. Bergen, Norway: University of Bergen, 2019.

[32] Leeman, Jonathan E et al. 'Proton therapy for head and neck cancer: expanding the therapeutic window'. *The Lancet Oncology* 18, 2017.

[33] Lomax, A. 'Intensity modulation methods for proton radiotherapy'. *Physics in Medicine and Biology* 44, 1999.

[34] Durante, Marco and Paganetti, Harald. 'Nuclear physics in particle therapy: a review'. *Reports on Progress in Physics* 79, 2016.

[35] Ottosson, Wiviann et al. 'Monte Carlo calculations support organ sparing in Deep-Inspiration Breath-Hold intensity-modulated radiotherapy for locally advanced lung cancer'. *Radiotherapy and Oncology* 117, 2015.

[36] Josipovic, Mirjana et al. 'Deep inspiration breath hold in locally advanced lung cancer radiotherapy: validation of intrafractional geometric uncertainties in the INHALE trial'. *The British Journal of Radiology* 92, 2019.

[37] Norsk Lunge Cancer Gruppe, KVIST group. *Professional guidelines for curative radiotherapy of non-small cell lung cancer*. Tech. rep. Revised version 2016. Norway: Østerås: Norwegian Radiation Protection Authority, 2017.

[38] Li, Heng et al. 'Robust optimization in intensity-modulated proton therapy to account for anatomy changes in lung cancer patients'. *Radiotherapy and Oncology* 114, 2015.

[39] Szeto, Yenny Z. et al. 'Effects of anatomical changes on pencil beam scanning proton plans in locally advanced NSCLC patients'. *Radiotherapy and Oncology* 120, 2016.

[40] Dance, D.R et al. *Diagnostic Radiology Physics: A Handbook for Teachers and Students*. Vienna: IAEA, 2014.

[41] Gomà, Carles, Almeida, Isabel P and Verhaegen, Frank. 'Revisiting the single-energy CT calibration for proton therapy treatment planning: a critical look at the stoichiometric method'. *Physics in Medicine & Biology* 63, 2018.

[42] White, D. R., Griffith, R. V. and Wilson, I. J. 'Appendix A: Body Tissue Compositions'. *Reports of the International Commission on Radiation Units and Measurements* os-24, 1992. ICRU Report 46.

[43] Rutherford, R. A., Pullan, B. R. and Isherwood, I. 'Measurement of effective atomic number and electron density using an EMI scanner'. *Neuroradiology* 11, 1976.

[44] Mayles, Philip, Nahum, Alan and Rosenwald, Jean-Claude. *Handbook of Radiotherapy Physics*. 1st ed. Florida: CRC Press, 2007.

[45] Ziegler, J F. 'The Stopping of Energetic Light Ions in Elemental Matter'. *J. Appl. Phys* 85, 1999.

[46] Berger, M.J. and Seltzer, S.M. *Stopping Powers and Ranges of Electrons and Positrons*. Tech. rep. U.S. Department of commerce - National bureau of standards, 1982.

[47] Bär, Esther et al. 'Optimized I-values for use with the Bragg additivity rule and their impact on proton stopping power and range uncertainty'. *Physics in Medicine & Biology* 63, 2018.

[48] Thoracic Key. *Basic Principles in Computed Tomography (CT)*. URL: https://thoracickey.com/basic-principles-in-computed-tomography-ct/ (visited on 19/12/2021).

[49] Wohlfahrt, Patrick and Richter, Christian. 'Status and innovations in pre-treatment CT imaging for proton therapy'. *The British Journal of Radiology* 93, 2020.

[50] Schneider, Uwe, Pedroni, Eros and Lomax, Antony. 'The calibration of CT Hounsfield units for radiotherapy treatment planning'. *Physics in Medicine and Biology* 41, 1996.

[51] Høisæter, Annette. 'Reducing Uncertainty in Proton Therapy Treatment Planning'. MA thesis. Bergen, Norway: University of Bergen, 2020.

[52] Kwint, Margriet et al. 'Intra thoracic anatomical changes in lung cancer patients during the course of radiotherapy'. *Radiotherapy and Oncology* 113, 2014.

[53] Ainsley, Christopher G. and Yeager, Caitlyn M. 'Practical considerations in the calibration of CT scanners for proton therapy'. *Journal of Applied Clinical Medical Physics* 15, 2014.

[54] Fjell, Else-Gunn, Aaberg, Tone and Bolstad, Kirsten. 'Visuell forbedring av CT-bildekvalitet for inntegning av risikoorganer ved stråleterapibehandling'. *Hold Pusten* 01, 2020.

[55] Krah, N et al. 'Regularised patient-specific stopping power calibration for proton therapy planning based on proton radiographic images'. *Physics in Medicine & Biology* 64, 2019.

[56] Hünemohr, Nora et al. 'Experimental verification of ion stopping power prediction from dual energy CT data in tissue surrogates'. *Physics in Medicine and Biology* 59, 2014.

[57] Sonke, Jan-Jakob, Aznar, Marianne and Rasch, Coen. 'Adaptive Radiotherapy for Anatomical Changes'. *Seminars in Radiation Oncology* 29, 2019.

A

TNM-CLASSIFICATION OF STAGE III LUNG CANCER

Classification of stage III lung cancer according to the TNM staging system 8th edition [22] is shown in Table A.1 with description of symbols in Table A.2.

Table A.1: Stage III lung cancer is divided into three stages, IIIA, IIIB and IIIC [22] based on different tumor sizes and degree of metastasis. The explanation of symbols is given in Table A.2.

Stage	**T**	**N**	**M**
IIIA	T1a,c T2a,b	N2	M0
	T3	N1	M0
	T4	N0, N1	M0
IIIB	T1a,c T2a,b	N3	M0
	T3, T4	N2	M0
IIIC	T3, T4	N2	M0

Table A.2: Explanation of the symbols included in classification of stage III lung cancer [22].

T	**Primary tumor**
T1	Tumor 3 cm or less in greatest dimension, surrounded by lung or visceral pleura, no evidence of invasion to main bronchus T1a - Tumor 1 cm or less T1b - Tumor between 1 cm and 2 cm T1c - Tumor between 2 and 3 cm
T2	Tumor between 3 cm and 5 cm in greatest dimension or tumor with any of the following features: - involves main bronchus - invades visceral pleura - associated with atelectasis or obstructive pneumonitis that extends to the hilar region either involving part of or the entire lung T2a - Tumor between 3 cm and 4 cm T2b - Tumor between 4 cm and 5 cm
T3	Tumor between 5 cm and 7 cm in greatest dimension, or tumor that invades the parietal pleura, chest wall, phrenic nerve or parietal pericardium, or separate tumor nodes in the same lobe as the primary
T4	Tumor greater than 7 cm or tumor of any size that invades intrathoracic structures such as the mediastinum, heart, diaphragm trachea, esophagus or separate tumor nodes in a different ipsilateral lobe to that of the primary

N	**Regional Lymph nodes**
N0	No regional lymph node metastasis
N1	Metastasis in ipsilateral peribronchial and/or ipsilateral hilar lymph nodes and intrapulmonary nodes, including involvement by direct extension
N2	Metastasis in ipsilateral mediastinal and/or subcarinal lymph node(s)

M	**Distant Metastasis**
M0	No distant metastasis

B

TABULAR MATERIALS FOR CT CALIBRATION

B.1 GAMMEX INSERT CONSTITUENTS

Elemental composition of the 16 inserts of the Gammex 467 Tissue Characterization Phantom are shown in Table B.1. Also the relative electron density and relative mass density of each insert are presented.

Table B.1: Elemental composition (in percent), relative electron density ($\hat{\rho}_e$) and relative mass density ($\hat{\rho}$) of the Gammex 467 inserts, provided by the manufacturer.

Element	**H**	**C**	**N**	**O**	**Mg**	**Si**	**P**	**Cl**	**Ca**	$\hat{\rho}_e$	$\hat{\rho}$ (g/cm^3)
Z	1	6	7	8	12	14	15	17	20		
A	1.008	12.01	14.01	16	24.31	28.09	30.97	35.45	40.08		
Lung 300	8.46	59.38	1.96	18.14	11.19	0.78	0	0.1	0	0.281	0.290
Lung 450	8.47	59.57	1.97	18.11	11.21	0.58	0	00.1	0	0.458	0.470
Adipose	09.06	72.3	2.25	16.27	0	0	0	0.13	0	0.928	0.945
Breast	8.59	70.11	2.25	16.27	0	0	0	0.13	0.95	0.954	0.977
Water	11.19	0	0	88.81	0	0	0	0	0	1.000	1.000
Solid Water	8.02	67.23	2.41	19.91	0	0	0	0.14	2.31	0.988	1.017
Solid Water	8.02	67.23	2.41	19.91	0	0	0	0.14	2.31	0.988	1.017
Solid Water	8.02	67.23	2.41	19.91	0	0	0	0.14	2.31	0.988	1.017
Muscle	8.1	67.17	2.42	19.85	0	0	0	0.14	2.32	1.020	1.050
Brain	10.83	72.54	1.69	14.86	0	0	0	0.08	0	1.047	1.051
Liver	8.06	67.01	2.47	20.01	0	0	0	0.14	2.31	1.063	1.095
Inner Bone	6.67	55.64	1.96	23.52	0	0	3.23	0.11	8.87	1.086	1.133
B-200	6.65	55.52	1.98	23.64	0	0	3.24	0.11	8.87	1.102	1.150
CB2-30 %	6.68	53.48	2.12	25.61	0	0	0	0.11	12.01	1.279	1.334
CB2-50 %	4.77	41.63	1.52	32	0	0	0	0.08	20.02	1.471	1.561
Cort Bone	3.41	31.41	1.84	36.5	0	0	0	0.04	26.81	1.696	1.824

The mean ionisation energy of the elements present in the Gammex inserts are presented in Table B.2.

Table B.2: Mean excitation energies for the elements in a solid state. From Berger et al 1982.

Element	**H**	**C**	**N**	**O**	**Mg**	**Si**	**P**	**Cl**	**Ca**
I (eV)	19.2	81	82	106	176.3	195.5	195.5	180	215.8

B.3 HU AND RSP FOR ICRU STANDARD TISSUES

Table B.3 lists the 60 adult human tissues with elemental composition given in ICRU Report 46 [42], with the synthetic HU of each tissue calculated for the relevant CT-scanner (Philips Brilliance Big Bore) and the theoretical RSP values calculated by Equation 2.8. These values were used to create the HLUT.

Table B.3: Synthetic HU values and calculated RSP values for the ICRU standard human tissues on the applied CT scanner.

Tissue	Synthetic HU	Calculated RSP
Adipose 1	-43.35630634128484	0.973813572518248
Adipose 2	-61.64618608817596	0.9562794600546007
Adipose 3	-79.98377098151599	0.9387392369531946
Lipoma	-42.253316597749226	0.9838930447427248
ST ICRU-33	-191.32115044022825	0.9847684098053728
ST ICRU-44m	15.045053111477413	1.0259887765728941
ST ICRU-44f	4.362802238067731	1.0173959871817349
Blood	45.76163798619204	1.0519628500003932
Brain	33.482094606905655	1.037400797991616
Breast-mam-1	-27.553003665487296	0.9916745744009369
Breast-mam-2	1.8574386864893544	1.0175732353786446
Breast-mam-3	39.02048139857417	1.05235878853461
Breast 50/50	-44.15404670346634	0.9672101952616178
Breast 33/67	-67.71472812040247	0.9469212912672645
Carbohydrate	412.2764955832501	1.4911887552964551
Cell nucleus	-4.2966187111844745	0.9948040130782234
Eye lens	38.852980620292186	1.0582767123419008
Gallstones	62.015063820548775	1.0873801775831469
GI tract	17.994158506197344	1.0252410750472016
Heart healty	35.811095916558735	1.0432528618353187
Heart fatty	24.74938135260718	1.0344449741332582
Heart filled	46.30117813223977	1.0520948844041749
Kidney	35.43671245492419	1.0431361905249936
Lipid	-90.62233021591793	0.9303215834611016
Liver healthy	43.870068404848304	1.0520915585095987
Liver cirrhotic	24.666362849877554	1.0347405837495214
Liver fatty	34.114140063213895	1.0434400654500395

Tissue	Synthetic HU	Calculated RSP
Lung healty	-743.4553064805863	0.25823952836160624
Lung congested	28.849916540511167	1.0339454898648281
Lymp	21.942528220520785	1.0248593532645964
Muscle	34.69558246835991	1.0431487343789252
Ovary	40.28927289362194	1.0460213784891141
Pancreas	29.533081751229815	1.0375444635122641
Protein	230.5132886505261	1.2983084123378186
Skeleton-cartil	79.93713621403376	1.0840351728669213
Skeleton-cort.b	1125.7807602229848	1.7655978290512704
Skeleton crani	743.3354836681975	1.5089771301816863
Femur - 30y	412.5892285463588	1.2746833442015015
Femur - 90y	280.43108076038646	1.1815892015911398
Humerus-	563.3192006648919	1.3833687460818909
Mandible	827.7394976738892	1.5676261480416864
Red Marrow	12.054304003414451	1.0269891758096517
Ribs1	491.63486786420685	1.3421592603072316
Ribs2	631.6652690983409	1.4359052235790284
Sacrum M	343.46566621945817	1.2436078440096057
Sacrum F	467.9626054084083	1.3276287427395992
Spongiosa	215.75961834387502	1.1498984801466396
Vert.col. C4	503.7520515702398	1.350949082270672
Vert.col. D6, L3	393.57695635034264	1.2747065768320367
Yellow marrow	-32.86663191309602	0.986741262656642
Skin	64.46277831237657	1.0795222496238708
Spleen	44.36776389038943	1.0520438173712183
Testis	31.74577508947296	1.0371078321530556
Thyroid	64.39345219807335	1.0431587009873087
Bladder empty	29.55365757308215	1.0340130369405096
Bladder filled	27.49147871272917	1.0277947545192812
Ur. stones cyst	653.4763632451193	1.561567753563761
Ur. stones oxa	1597.6242209017996	2.075536553906698
Ur. stones acid	496.456824007008	1.6215633962986105
Water	0.0	1.000889802160326

C

WEPL HISTOGRAMS FOR ALL PATIENTS

The figures of this appendix show histograms of the absolute WEPL changes (|ΔWEPL|) for all patients. The changes from the pCT to the rCTs of week 1 are shown on the left side of the paper and to the rCT of week 3 on the right side of the paper.

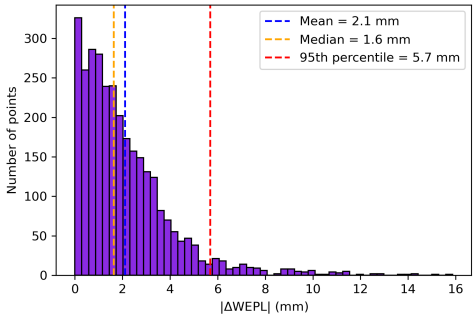

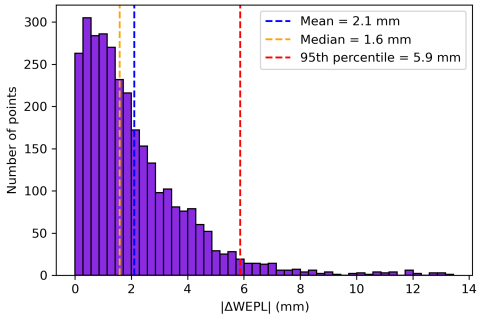

Figure C.1: Patient 1

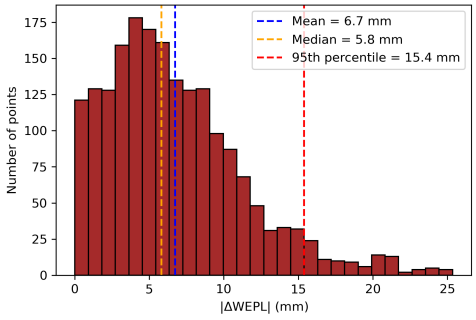

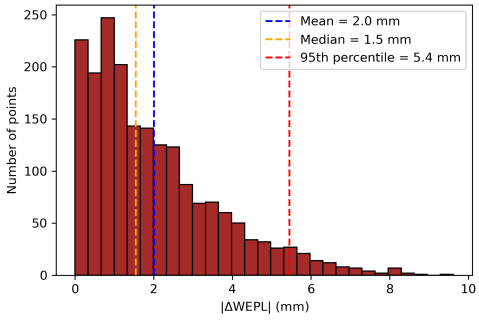

Figure C.2: Patient 2

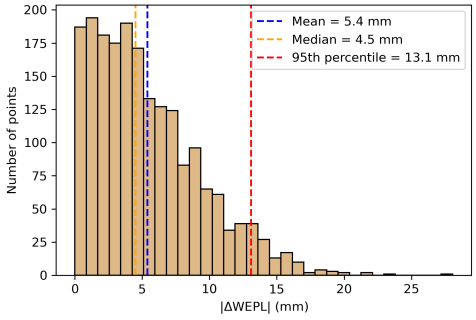

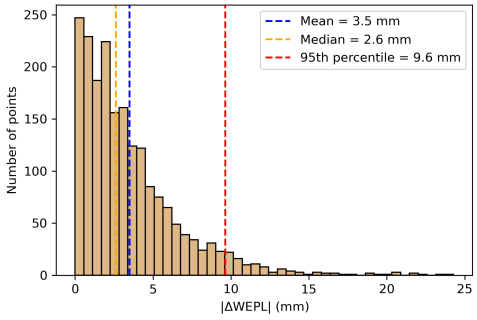

Figure C.3: Patient 3

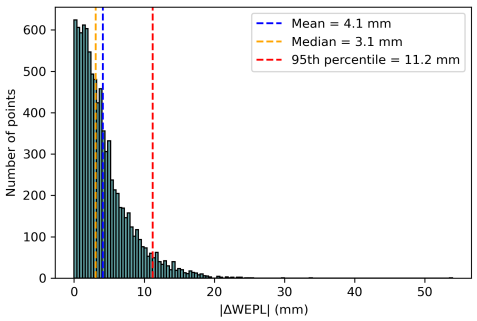

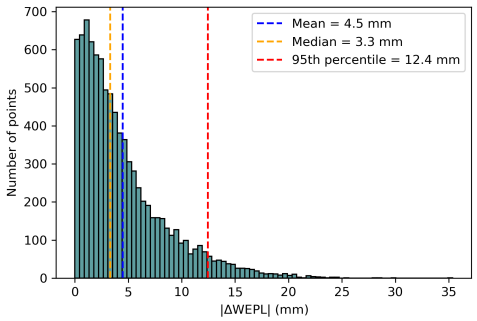

Figure C.4: Patient 4

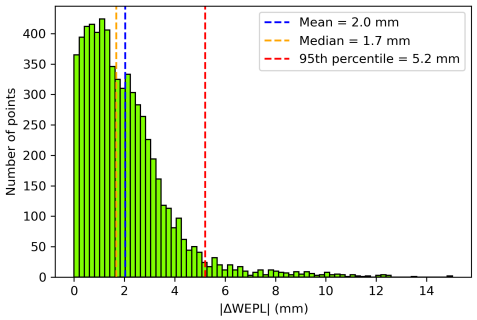

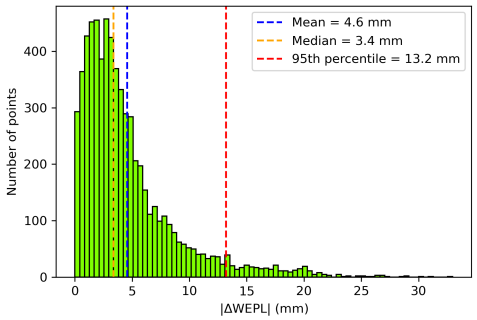

Figure C.5: Patient 5

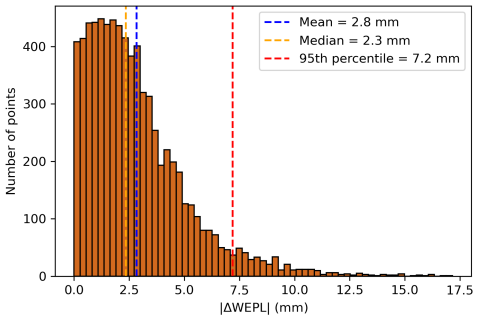

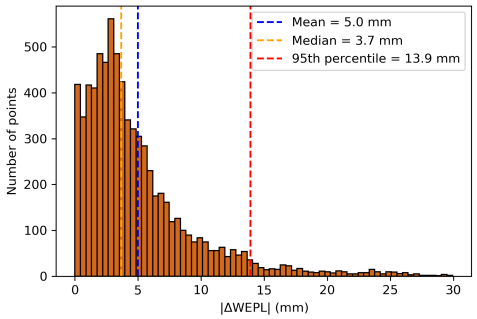

Figure C.6: Patient 6

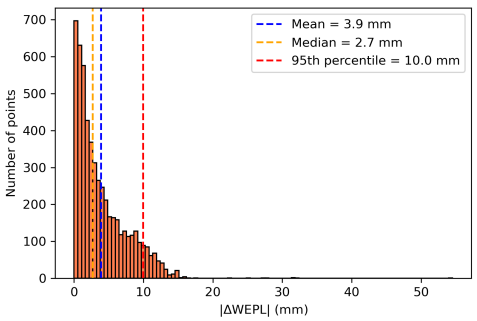

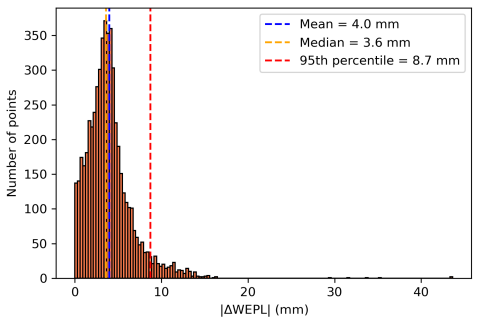

Figure C.7: Patient 7

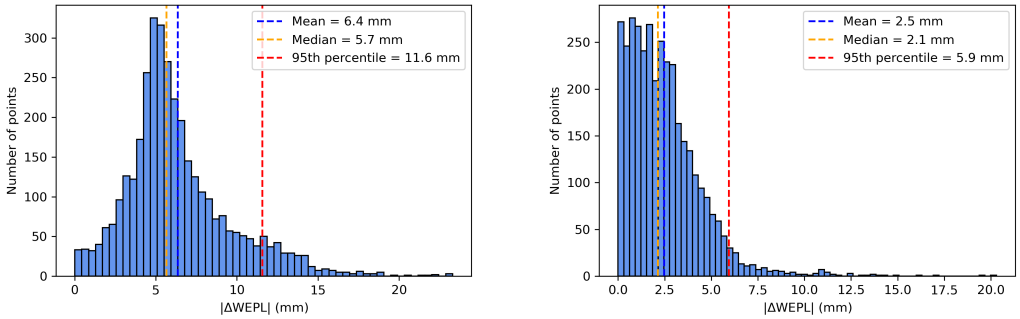

Figure C.8: Patient 8

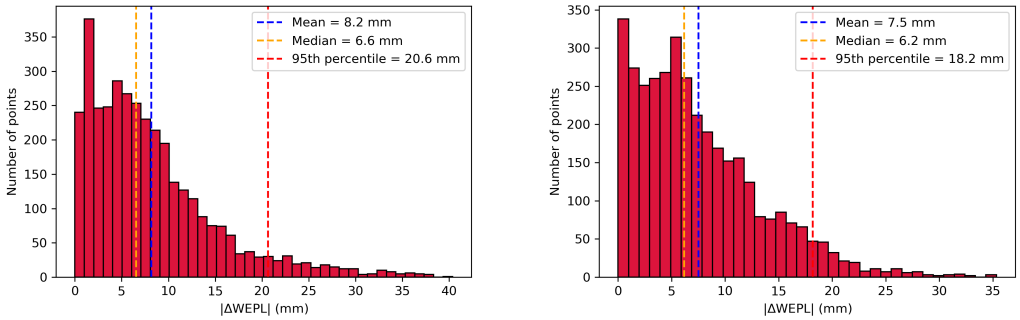

Figure C.9: Patient 9

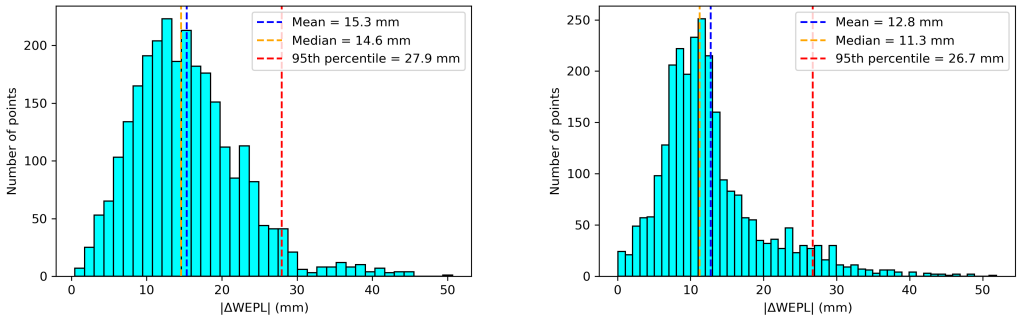

Figure C.10: Patient 10

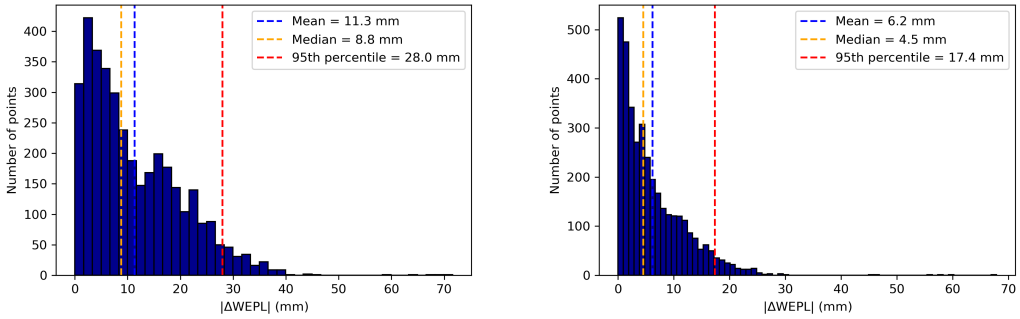

Figure C.11: Patient 11

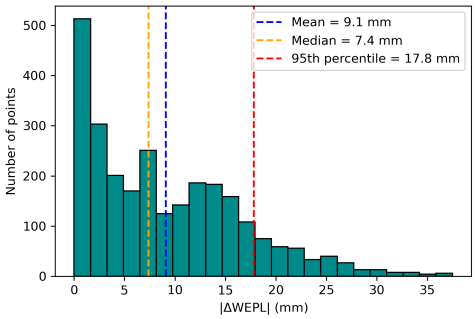

Figure C.12: Patient 12

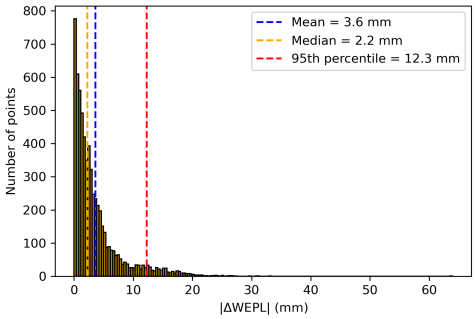

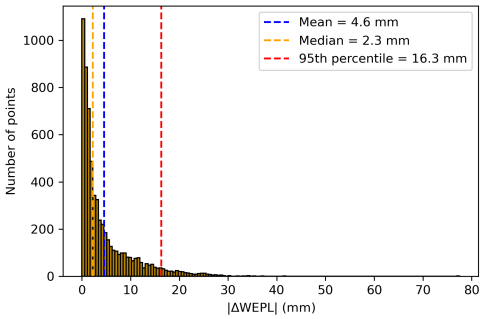

Figure C.13: Patient 13

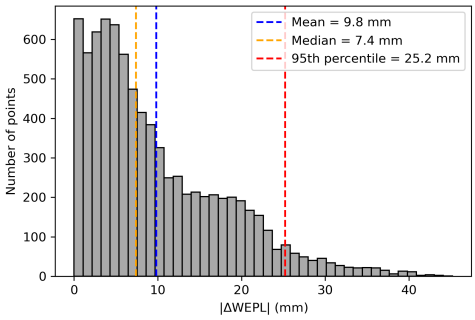

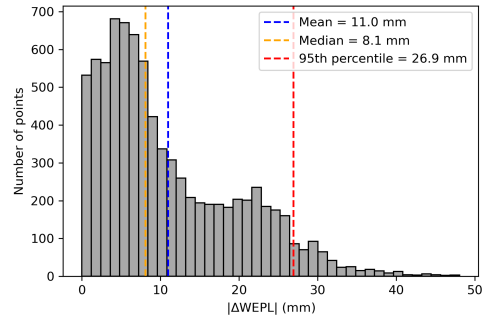

Figure C.14: Patient 14

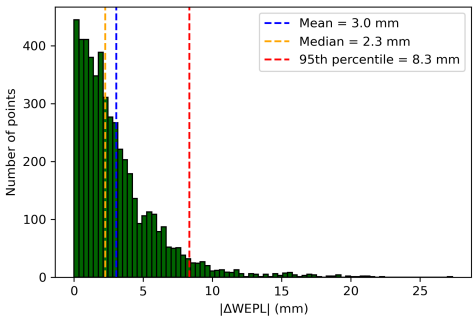

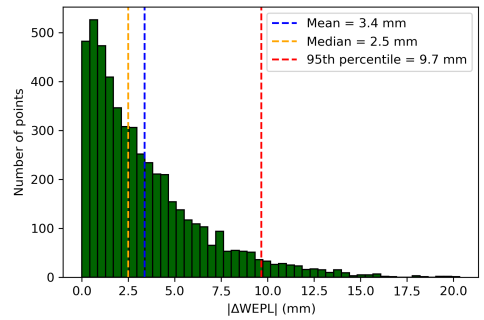

Figure C.15: Patient 15

D

PYTHON CODES

D.1 STOICHIOMETRIC CALIBRATION

The python code for the stoichiometric calibration and generation of the HLUT written by Annette Høisæter [51] were implemented by the candidate with some modifications in order to be applied on the CT scans of the present study.

Listing D.1: Measuring HU in Gammex inserts

```
import numpy as np, pandas as pd, pydicom, glob, math
images = "Data/Philips pulmDIBH B 120kV/*" #27 images
sortDict = {}
for imageNo in range(27):
    path = glob.glob(images)[imageNo]
    ds = pydicom.dcmread(path, stop_before_pixels=True)
    sortDict[ds.SliceLocation] = path
sortedKeys = sorted(sortDict.keys())
def ROI(ar, circle, r):
    ROI    = np.zeros(np.shape(ar), dtype=np.bool_)
    x0, y0 = circle
    for y in range(math.floor(y0 - r), math.ceil(y0 + r) + 1):
        for x in range(math.floor(x0 - r), math.ceil(x0 + r) + 1):
            if (x - x0)**2 + (y - y0)**2 < r**2:
                ROI[y, x] = True
    return ROI
circles =      {"Lung 300":      (317, 137),
                "Lung 450":      (143, 207),
                "Adipose":       (335, 261),
                "Breast":        (216, 209),
                "Water":         (196, 261),
                "SW1":           (217, 137),
                "SW2":           (389, 209),
                "SW3":           (316, 384),
                "Muscle":        (264, 329),
                "Brain":         (315, 211),
                "Liver":         (213, 380),
                "Inner bone":    (388, 312),
                "B-200":         (141, 310),
                "CB2-30%":      (215, 308),
                "CB2-50%":       (314, 309),
                "Cortical bone": (266, 190)
                }
radius = 15
```

```
radius_water = 7
HU_df = pd.DataFrame()
HU_df["Tissue type"]  = circles.keys()
for imageNo in range(11,16): #5 following slices
    for tissue, v in circles.items():
        if tissue == 'Water':
            HU = np.mean(img_ds[ROI(img_ds, circles[tissue],
                radius_water)])
            ROI_imageNo.append(round(HU,3))
        else:
            HU = np.mean(img_ds[ROI(img_ds, circles[tissue], radius)
                ])
            ROI_imageNo.append(round(HU,3))
    HU_df["Slice {}".format(imageNo)] = ROI_imageNo
HU_df['Mean HU'] = (HU_df.mean(numeric_only = True, axis = 1)).round
    (3)
meanHU_df = HU_df[['Tissue type', 'Mean HU']]
meanHU_df.to_csv('Data/Measured_Mean_HU_Gammex.csv', index = False)
```

Listing D.2: Determining k-values

```
import numpy as np, pandas as pd, matplotlib.pyplot as plt
from scipy.optimize, import minimize
from scipy.stats, import linregress
measured  = pd.read_csv("Data/Measured_Mean_HU_Gammex.csv")
data      = pd.read_csv("Data/datablad_gammex_ordered.csv")
index = data.index
idx_w = index[data['Element'] == 'Water'].tolist()[0]
def objective(k):
    k1 = k[0]
    k2 = k[1]
    x_ = list()
    y_ = list()
    wH = float(data.iloc[idx_w,1]) #wH = 0.1119
    AH = float(data.iloc[1,1]) #AH = 1.008
    wO = float(data.iloc[idx_w,4]) #wO = 0.8881
    AO = float(data.iloc[1,4]) #AO = 16
    sum_water = wH/AH*(1+k1+k2) + wO/AO*(8+k1*8**2.86+k2*8**4.62)
    sum_tot=0
    for i in range (2,18):          # rows (CB2-30% - Breast)
        sum_row = 0
        for j in range (1,10):      # columns (H - Ca)
            wi  = float(data.iloc[i,j])
            Ai  = float(data.iloc[1,j])
            Zi  = float(data.iloc[0,j])
            rho = float(data.iloc[i,11]) #relative mass density
            sum_element = wi/Ai * (Zi + k1*Zi**2.86 + k2*Zi**4.62)
            sum_row += sum_element
        calc_HU = rho*(sum_row/sum_water)
```

```
        meas_HU = (float(measured.iloc[i-2,1]))/1000 + 1
        if kDRAW:
            x_.append(meas_HU)
            y_.append(calc_HU)
        diff_squared = (calc_HU - meas_HU)**2
        sum_tot += diff_squared
    return sum_tot
# Initial guess-values
k0 = [5.3e-4, 2.3e-5]
kDRAW = True
kDRAW = False
# Bounds (Goma)
b1 = (2e-4, 6e-3)
b2 = (3e-6, 6e-4)
bnds = (b1, b2)
# Solve:
sol = minimize(objective, k0, method='SLSQP', bounds=bnds)
print('\n Optimal: k1 =', sol.x[0], '/ k2 = ', sol.x[1])
kDRAW = True
#Save k-values to csv-file to be used in other program files
k_df = pd.DataFrame()
k_df['k1'] = [sol.x[0]]
k_df['k2'] = [sol.x[1]]
k_df.to_csv('Data/k-values.csv', index = False)
```

Listing D.3: Synthetic HU and RSP in ICRU tissues

```
import numpy as np, pandas as pd, matplotlib.pyplot as plt
from scipy.optimize, import minimize
from scipy.constants, import c as c
from math, import log
data = pd.read_csv("Data/standard-tissues.csv")
ks = pd.read_csv("Data/k-values.csv")
#Index for water: 63
wH = float(data.iloc[63,1])/100 #0.1119
AH = float(data.iloc[1,1]) #1.008
wO = float(data.iloc[63,4])/100 #0.8881
AO = float(data.iloc[1,4]) #16.0
k1 = ks['k1'].tolist()[0]
k2 = ks['k2'].tolist()[0]
sum_water = wH/AH * (1 + k1 + k2) + wO/AO * (8 + k1*8**2.86 + k2
    *8**4.62)
#Calculate HU and I-values for each tissue substitute
calc_HU = []
e = math.e
I_list = []
for i in range(2,64): #From Adipose #1 to Water--
    sum_row = 0
    sum1 = 0
```

```
    sum2 = 0
    for j in range(1,14): #From H to I
        wi  = float(data.iloc[i,j])/100
        Ai  = float(data.iloc[1,j])
        Zi  = float(data.iloc[0,j])
        rho = float(data.iloc[i,16]) #relative mass density
        sum_element = wi/Ai * (Zi + k1*Zi**2.86 + k2*Zi**4.62)
        sum_row += sum_element
        lni = log(float(data.iloc[64,j]))
        sum1 += wi*(Zi/Ai)*lni
        sum2 += wi*(Zi/Ai)
    HU_reduced = rho*(sum_row/sum_water)
    HU = (HU_reduced-1)*1000
    calc_HU.append(HU)
    I_list.append(sum1/sum2)
rho_list = data['rho_e_rel'][2:64].tolist() #Rel electron densities
# Calculation of RSPs
MeV = 1e6
me = 0.511*MeV
mp = 938*MeV
Iw = 78                     # Ionization energy water #Goma
Ek = 100*MeV                # Proton kinetic energy #Goma
b = np.square(1 - mp**2 / (mp + Ek)**2)   # Velocity 100 MeV proton [
    c]
S_ew = log((2*me*c**2*b**2) / (1-b**2)) - b**2 - log(Iw)
RSP_list = []
for i in range(len(I_list)):
    Ix = I_list[i]
    pe = rho_list[i]
    substitute = data.iloc[i+2,0]
    S_e = log((2*me*c**2*b**2) / (1-b**2)) - b**2 - (Ix)
    RSP = pe * (S_e/S_ew)
    RSP_list.append(RSP)
HU_SPR_df = pd.DataFrame()
HU_SPR_df['Tissue type'] = data['Tissue--'][2:-1]
HU_SPR_df['HU'] = calc_HU
HU_SPR_df['SPR'] = RSP_list
HU_SPR_df.to_csv(r'Data/HU_SPR_ICRU.csv', index = False)
```

Listing D.4: Making the HLUT

```
import numpy as np, pandas as pd, matplotlib.pyplot as plt, pwlf
data = pd.read_csv("Data/HU_SPR_ICRU.csv")
HU = data['HU'].tolist()
RSP = data['SPR'].tolist()
#Line segment locations
x0 = np.array([min(HU), 20, 40, max(HU)])
my_pwlf = pwlf.PiecewiseLinFit(HU, RSP)
my_pwlf.fit_with_breaks(x0)
```

```
xHat = np.linspace(min(HU), max(HU), num=10000)
yHat = my_pwlf.predict(xHat)
# Mathematical equation of the fit
from sympy import Symbol
from sympy.utilities import lambdify
x = Symbol('HU')
def get_symbolic_eqn(pwlf_, segment_number):
    if pwlf_.degree < 1:
        raise ValueError('Degree must be at least 1')
    if segment_number < 1 or segment_number > pwlf_.n_segments:
        raise ValueError('segment_number not possible')
    for line in range(segment_number):
        if line == 0:
            my_eqn = pwlf_.beta[0] + (pwlf_.beta[1])*(x-pwlf_.
                fit_breaks[0])
        else:
            my_eqn += (pwlf_.beta[line+1])*(x-pwlf_.fit_breaks[line])
    if pwlf_.degree > 1:
        for k in range(2, pwlf_.degree + 1):
            for line in range(segment_number):
                beta_index = pwlf_.n_segments*(k-1) + line + 1
                my_eqn += (pwlf_.beta[beta_index])*(x-pwlf_.
                    fit_breaks[line])**k
    return my_eqn.simplify()
```

D.2 CALCULATING WEPL IN PATIENT CT SCANS

A script for extracting the coordinates of all points at the CTV structure from DICOM structure files was written by the candidate's supervisor, H. Pettersen. The candidate implemented that script and wrote additional code for calculating the WEPL to every point at the distal edge of CTV.

Listing D.5: Calculating WEPL to distal edge of CTV in CT image

```
import numpy as np, pandas as pd, matplotlib.pyplot as plt
import pydicom, glob, os, sys
# References: https://github.com/xuejianma/fastLinecut_radialLinecut/
    blob/main/fastLinecut_radialLinecut.ipynb
def euclideanDistance(coord1,coord2):
    return np.sqrt((coord1[0]-coord2[0])**2 + (coord1[1]-coord2[1])
        **2)
def getRowCol(pt,X,Y):
    if (X.min()<=pt[0]<=X.max()) and (Y.min()<=pt[1]<=Y.max()):
        pass
    else:
        raise ValueError('The input center is not within the given
            scope.')
```

```
    center_coord_rowCol = (np.argmin(abs(Y-pt[1])), np.argmin(abs(X-
        pt[0])))
    return center_coord_rowCol #row and col for data point
def getLinecut(image, X, Y, pt1, pt2):
    row_col_1, row_col_2 = getRowCol(pt1,X,Y), getRowCol(pt2,X,Y)
    row1,col1 = np.asarray(row_col_1).astype(float)
    row2,col2 = np.asarray(row_col_2).astype(float)
    dist = euclideanDistance(pt1,pt2)
    N = int(euclideanDistance(row_col_1,row_col_2))
    rowList = [int(row1+(row2-row1)/N*ind) for ind in range(N)]#(N+1)
    colList = [int(col1+(col2-col1)/N*ind) for ind in range(N)]#(N+1)
    distList = [dist/N*ind for ind in range(N)] #(N+1)
    return distList, image[rowList, colList]
def binarySearch(left,right,conditionFunction,threshold=1e-5):
    if euclideanDistance(left,right)/euclideanDistance(right,(0,0))<=
        threshold:
        return left
    middle = (left+right)/2
    if conditionFunction(middle) is False:
        result = binarySearch(middle,right,conditionFunction)
    else:
        result = binarySearch(left,middle,conditionFunction)
    return result
def exclusionCondition(pt,X,Y):
    if X.min()<=pt[0]<=X.max() and Y.min()<=pt[1]<=Y.max():
        return False
    else:
        return True
def getEdgePointFromCenter(image,X,Y,center,angleDegree):
    unitVector = np.asarray([np.cos(angleDegree*np.pi/180), np.sin(
        angleDegree*np.pi/180)])
    unitVectorNeg = unitVector
    trialEdgeNeg = np.asarray(center).astype(float)
    while not exclusionCondition(trialEdgeNeg,X,Y):
        trialEdgeNeg -= unitVectorNeg
        unitVectorNeg *= 2
    left = trialEdgeNeg + unitVectorNeg/2
    right = trialEdgeNeg
    edgeNeg = binarySearch(left,right,lambda middle:
        exclusionCondition(middle,X,Y))
    return edgeNeg
def closestMaching(value, alist):
    min_diff = 1000
    closestvalue = 0
    for i in range(len(alist)):
        abs_diff = abs(alist[i] - value)
        if abs_diff < min_diff:
            min_diff = abs_diff
            closestvalue = alist[i]
```

```
    return closestvalue
# use HLUT to find RSP and WEPL
break1 = 20
break2 = 40
def HLUT(HU):
    if HU <= break1:
        RSP = 0.00097643842534950 1*HU + 1.01685572002769
    elif break1 < HU <= break2:
        RSP = 0.00102118905637142*HU + 1.01596070740725
    elif HU > break2:
        RSP = 0.00069419119987 0186*HU + 1.0290406216673
    return RSP
def calculateWEPL(ptPos, image, X, Y, pixelSp):
    #X, Y : Coordinate system of image
    edgePos = getEdgePointFromCenter(image, X, Y, ptPos, theta+90)
    distList, linecut = getLinecut(image, X, Y, edgePos, ptPos)
    RSP_list = []
    WEPL_list = []
    for HU in linecut:
        RSP = HLUT(HU)
        RSP_list.append(RSP)
        WEPL_list.append(pixelSp * distList[1] * np.sum(RSP_list))
    WEPL = pixelSp * distList[1] * np.sum(RSP_list)
    return WEPL, distList, edgePos

patient = 2
field_nr = 1 #1,2,3
whichCT = 'Plan' #'Week1' 'Week3'
structuresetname = ' '
structureName = ' '
dicomStructureFile = " "
percentileCutoffForDistances = 50 #in percent
folderWithAllImages = " "
allImageFiles = glob.glob(f"{folderWithAllImages}/CT*")
# Field angles from excel
fields_data = pd.read_excel("Data/Patient plan details.xlsx",
    sheet_name = "Beam angles", header = 1, index_col="PATIENT",
    usecols="A,C,E,G")
fields_data = fields_data.fillna(0.0)
theta = fields_data.at[patient, f'{field_nr} Gantry [deg]']
if theta > 400:
    print('OBS: Field angle do not exist!')
    sys.exit()
# Image Registration Translation from excel
translation_data = pd.read_excel("Data/Patient plan details.xlsx",
    sheet_name = "Translation", header = 1, index_col="PATIENT",
    usecols="A:J")
translation_data = translation_data.fillna(0.0)
trans_x = translation_data.at[patient, f'{whichCT} x']
```

```
trans_y = translation_data.at[patient, f'{whichCT} y']
trans_z = translation_data.at[patient, f'{whichCT} z']
eclipseTranslation = [trans_x, trans_y, trans_z]
zposLUT = dict()
structureDict = dict()
contours = list()
WEPLdict = dict()
for fDS in allImageFiles:
    ds = pydicom.dcmread(fDS, stop_before_pixels=True)
    zpos = ds.ImagePositionPatient[2] - eclipseTranslation[2]
    zposLUT[zpos] = fDS
rs = pydicom.dcmread(dicomStructureFile)
# Find correct structure ID from structureName
for seq in rs.StructureSetROISequence:
        structureDict[seq.ROIName] = seq.ROINumber
correctROINumber = structureDict[structureName]
# Load structure array (x,y,z)_i
for seq in rs.ROIContourSequence:
        if not 'ContourSequence' in seq or seq.ReferencedROINumber !=
            correctROINumber:
                continue
        for contour in seq.ContourSequence:
                contourReshape = np.reshape(contour.ContourData, (len
                    (contour.ContourData)//3, 3))
                contours.append(contourReshape)
# Convert contours into X, Y
num = 0
for contour in contours:
        # Load correct DICOM image
    zStructure = contour[0,2]
    zSlice = closestMaching(zStructure, list(zposLUT.keys()))
    print(f"Loading image at {zSlice}")
    ds = pydicom.dcmread(zposLUT[zSlice])
    sliceThickness = ds.SliceThickness
    pixelSpacing = ds.PixelSpacing[0]
    pixelArrayShape = np.shape(ds.pixel_array)
    dicomTranslation = [float(k) for k in ds.ImagePositionPatient]
    zSlice = round(zSlice,3)
    img = ds.pixel_array * ds.RescaleSlope + ds.RescaleIntercept
    img_copy = img.copy().astype(float)
    #Define coordinate system of image
    Xsys = np.linspace(0,np.shape(img)[1],np.shape(img)[1])
    Ysys = np.linspace(0,np.shape(img)[0],np.shape(img)[0])
    #Define coordinates of structure delineation
    Xpos, Ypos = list(), list()
    x0,y0 = [k/2 for k in pixelArrayShape]
    x = [(c - dicomTranslation[0] + eclipseTranslation[0]) /
       pixelSpacing for c in (contour[:,0])]
```

```
y = [(c - dicomTranslation[1] + eclipseTranslation[1]) /
    pixelSpacing for c in (contour[:,1])]
Xpos.append(x)
Ypos.append(y)
plt.clf()
plt.imshow(img, cmap="gray")
plt.axis('off')
WEPLs = list()
distances = list()
edgePoints = list()
for structureX, structureY in zip(Xpos,Ypos):
    for point in zip(structureX, structureY):
        WEPL_pt, distList_pt, edgePos_pt = calculateWEPL(point,
            img_copy, Xsys, Ysys, pixelSpacing)
        WEPLs.append(WEPL_pt)
        distances.append(max(distList_pt))
        edgePoints.append(edgePos_pt)
    WEPLs = np.array(WEPLs)
    distances = np.array(distances)
    percentileCutoff = np.percentile(distances,
        percentileCutoffForDistances)
    distanceFilter = distances >= percentileCutoff
    WEPLsFiltered = WEPLs[distanceFilter]
    structureX = np.array(structureX)
    structureY = np.array(structureY)
    XFiltered = structureX[distanceFilter]
    YFiltered = structureY[distanceFilter]
    edgePoints = np.array(edgePoints)
    edgePoints = edgePoints[distanceFilter]

    plt.plot(structureX, structureY, 'o', markersize=0.5, color =
        'lightcoral', label = f'Structure {structureName}')
    plt.plot(XFiltered, YFiltered, 'o', markersize=1, color='red'
        , label = f'Backend of structure {structureName}')
    for edgePos, ptPos in zip(edgePoints, zip(XFiltered,
        YFiltered)):
        plt.plot([ptPos[0],edgePos[0]], [ptPos[1], edgePos[1]],
            color = 'tab:orange', alpha = 0.2)
    plt.legend()
    plt.show()
    if f'{zSlice}' not in WEPLdict:
        WEPLdict[f'{zSlice}'] = WEPLsFiltered
        num = 0
    else:
        num += 1
        WEPLdict[f'{zSlice} {num}'] = WEPLsFiltered
```

Vilde Ragnvaldsen

NTNU
Norwegian University of
Science and Technology

Haukeland University Hospital